Airbursts and Cratering Impacts

2025 | Volume 3 | Pages: 1–47 | e-location ID: e20250004
DOI: 10.14293/ACI.2025.0004

Research Article

Evidence of a 12,800-year-old Shallow Airburst Depression in Louisiana with Large Deposits of Shocked Quartz and Melted Materials

Robert Fitzenreiter[1], Kord Ernstson[2], Gunther Kletetschka[3,4], Malcolm A. LeCompte[5], Christopher R. Moore[6,7], James P. Kennett[8], Michael Bizimis[9], Florian Hofmann[10], Marian Takac[4], A. Victor Adedeji[11], Timothy Witwer[1], Julie E. Chouinard[12], Jesus Paulo Perez[13], Marc D. Young[14], Teresa M. Eaton[15], Matthew J. Valente[16], David B. Lanning Jr.[15], Yoav Rapoport[15], Kailey Ellison[15], Argyro Reyes[15], Ravi Holladay[15], Michelle Madrigal[15], Julian Albanil[15], Charlie Sanchez[15] and Allen West[1,*]

[1]Comet Research Group, 2204 Lakewood Drive, Prescott, AZ 86301, USA; [2]Faculty of Philosophy, Julius-Maximilians-Universität, Würzburg, Germany; [3]Geophysical Institute, University of Alaska, Fairbanks, Alaska 99775, USA; [4]Faculty of Science, Charles University, Albertov 6, Prague 12843, Czech Republic; [5]Elizabeth City State University, Center of Excellence in Remote Sensing Education and Research, Elizabeth City, NC 27909, USA; [6]South Carolina Institute of Archaeology and Anthropology, University of South Carolina, Columbia, SC 29208, USA; [7]SCDNR Heritage Trust Program, Land, Water, and Conservation Division, South Carolina Department of Natural Resources, Columbia, SC 27909, USA; [8]Department of Earth Science and Marine Science Institute, University of California, Santa Barbara, Santa Barbara, CA 93106, USA; [9]School of Earth, Ocean and Environment, University of South Carolina, Columbia, SC 29208, USA; [10]Geophysical Institute, University of Alaska Fairbanks, 1930 Yukon Dr, Fairbanks, AK 99775, USA; [11]Department of Natural Sciences, Elizabeth City State University, Elizabeth City, NC 27909, USA; [12]CAMCOR, University of Oregon, 1443 E 13th Ave, Eugene, Oregon 97403, USA; [13]Electron Microscopy and Surface Analysis Lab, Nanofab, University of Utah, Salt Lake City, UT 84112, USA; [14]College of Humanities, Arts and Social Sciences, Flinders University, Bedford Park, Australia; [15]Department of Biology and Chemistry, College of Arts & Sciences, Embry-Riddle University, Prescott, AZ 86301, USA; [16]Life Sciences Dept., Harford Community College, Bel Air, MD 21015, USA

*Correspondence to: Allen West, E-mail: CometResearchGroup@gmail.com

Received: 27 April 2025; Revised: 27 April 2025; Accepted: 23 May 2025; Published online: 4 June 2025

How to cite: Fitzenreiter R., et al. Evidence of a 12,800-year-old Shallow Airburst Depression in Louisiana with Large Deposits of Shocked Quartz and Melted Materials. *Airbursts and Cratering Impacts*. 2025 | Volume 3 | Issue 1 | Pages: 1–47 | DOI: 10.14293/ACI.2025.0004

ABSTRACT

We report evidence of a likely low-altitude cosmic airburst near Perkins, Louisiana, associated with semi-consolidated deposits containing abundant shocked quartz grains, a classical impact indicator, along with spherules, meltglass, and microbreccia. Analytical techniques employed on these materials include optical microscopy, the universal stage, electron microscopy (SEM, TEM, and STEM), cathodoluminescence, laser ablation (LA-ICP-MS), neutron activation (INAA), and radiometric dating. These analyses reveal that the deposits exhibit morphological and compositional similarities to known impact-related proxies. Radiocarbon dating and 40Ar/39Ar analyses constrain the likely age of deposition to between 30,000 and 10,000 calibrated years BP, with a concentration of dates clustering around 12,800 years BP (12,835-12,735 cal BP), coinciding with the age range of the Younger Dryas Boundary (YDB). Spherule and meltglass abundances, along with evidence of high-temperature mineral transformations, are consistent with the effects of a high-energy airburst or impact. Hydrocode modeling suggests that a touch-down airburst could plausibly account for the observed shallow depression, material dispersal patterns, and geochemical signatures. Our study suggests that a 300-m-long lake/depression at the Perkins site represents North America's first identified YDB-age airburst crater.

KEYWORDS

Airbursts, comets, asteroids, impact crater, shocked quartz, remanent magnetism, hydrocode modeling, meltglass, microspherules, archaeology

Introduction

Cosmic airbursts and impacts produce a wide range of surface effects, with high-altitude airbursts, such as the 1908 Tunguska event, primarily generating blast damage without forming craters [1]. In contrast, low-altitude "touch-down" airbursts may induce surface melting, spherule formation, shocked quartz, and shallow cratering [2]. Due to preservation challenges, few airburst signatures are documented in the geologic record, limiting our understanding of these events.

Here, we report findings from a site approximately 5.8 km east of Perkins, Louisiana (30.3980° N, 93.3535° W) (Figure 1), where an anomalous 300-m-long seasonal lake/depression (Figure 2) is associated with extensive deposits of likely impact-related materials (Figure 3). We tested the hypothesis that an airburst/impact at the Perkins site produced these materials. To understand these deposits, we conducted a multi-disciplinary study employing a comprehensive suite of microscopy and geochemical techniques to characterize the material, investigate its origin, and determine whether the Perkins site represents an airburst/impact cratering event.

Research history

In ~1938, Walter Leo Fitzenreiter, Jr., father of the lead author (R.F.), first speculated that a seasonal lake on his property was an "impact crater" based solely on its shape and crater-like rim raised ~1 m above the surrounding terrain. Later, in 2006, lead author R.F. began to test his father's suggestion of a crater and discovered several locations around the lake displaying large semi-consolidated masses of spherules

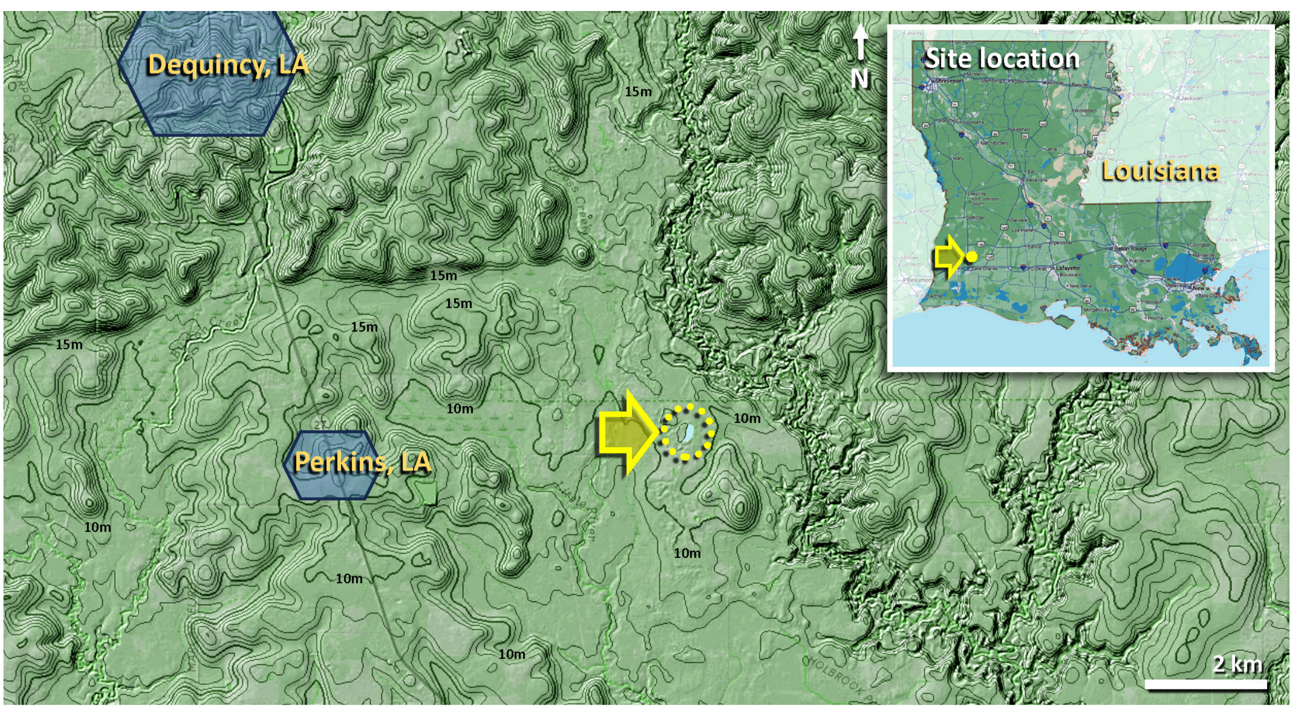

Figure 1: **Map.** The lake is located east of Perkins, LA, in the state's southwest corner (inset, arrow) and is called the Perkins site. Base image: USGS. Inset image: Google Maps, 2024, INEGI.

Figure 2: Lake/depression with locations of glass-and-spherule-rich material is outlined with the white dotted line. The Pond deposit is northwest of the lake/depression, and the Vee deposit is south of the lake/depression. Trench #1 is on the east rim of the lake/depression. The Lake deposit is within the lake/depression. Calibrated radiocarbon ages on organic material and carbon-rich meltglass are shown for three key deposits. Image: Google Earth, Maxar Technologies; imagery date: 12/13/2003; accessed: 8/8/2024.

associated with multi-cm-sized fragments of black vesicular glass, which, he reasoned, might result from a cosmic airburst/impact event. Beginning in 2006, lead author R.F. found very large quantities of meltglass and spherules in two deposits near the raised rim of the lake, ~300 m long and 120 m wide.

From 2006 through 2024, lead author R.F. also hand-extracted 32 cores (~4 to 13 cm in diameter) and excavated two trenches (~3 m wide). Locations and results are described in the sections below. In 2007, after identifying numerous spherules and fragments of meltglass in the Vee and Pond deposits, R.F. first contacted one of the co-authors (K.E.), who analyzed the spherules and meltglass. His analyses suggested that they resulted from a cosmic impact event, and he recommended additional research. In 2011, R.F. next contacted members of the Comet Research Group, who analyzed these materials to investigate their characteristics and origin.

Information on airbursts

Cosmic airbursts can occur at various altitudes, producing distinctly different surface effects. High-altitude airbursts, like the 1908 Tunguska event (~5-10 km altitude) [1], primarily cause widespread devastation through blast waves but typically leave no craters [2]. Even so, the airburst evidence at Tunguska has been reported to include spherules, shocked quartz, glass-filled fractured quartz, melted feldspar, carbon spherules, and glasslike carbon [1]. Such events, called

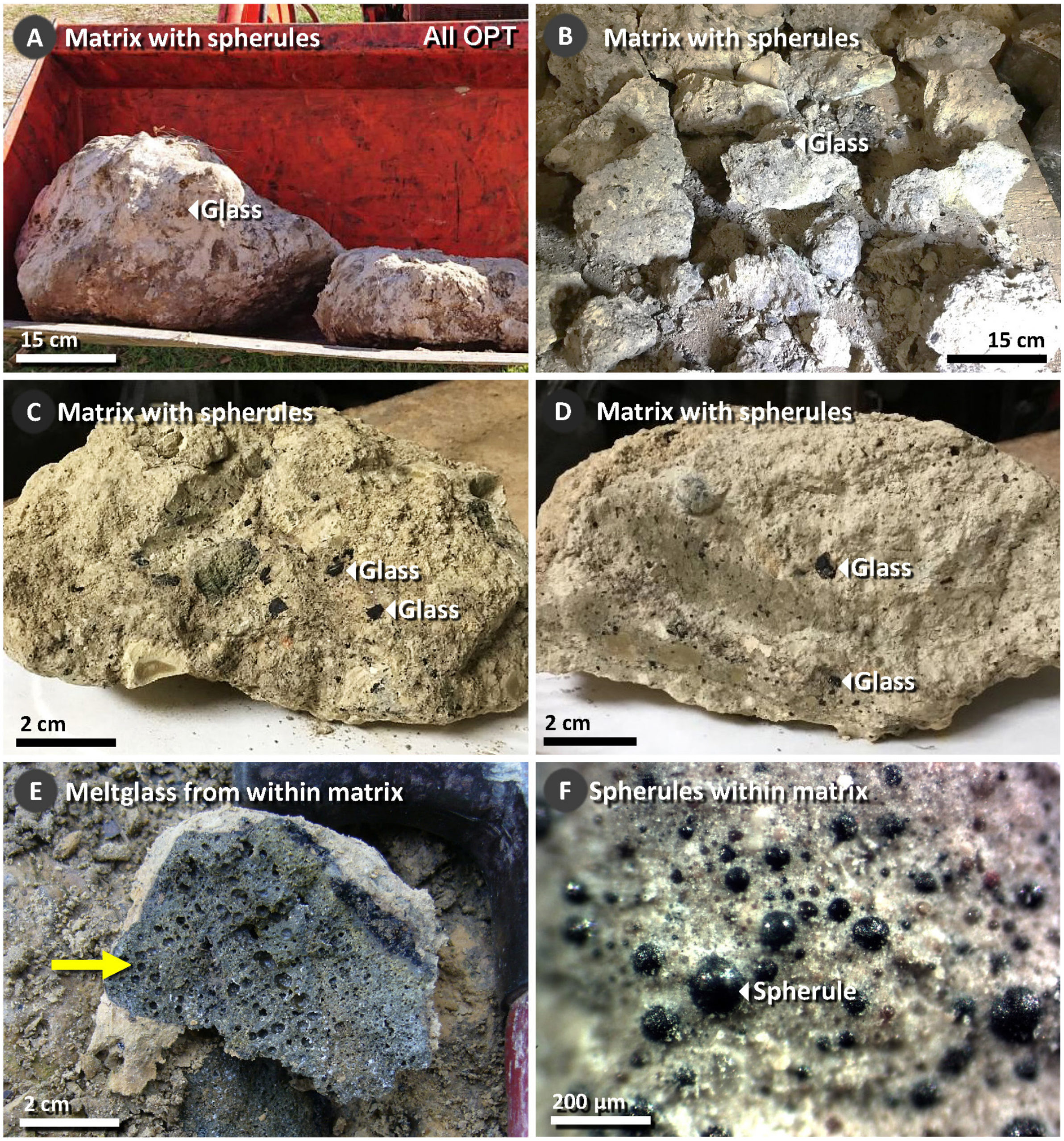

Figure 3: Optical photographs of meltglass and spherules from the Pond deposit. (**A-D**) The original discovery was of a sizeable semi-consolidated surface deposit, primarily comprised of billions of spherules and fragments of meltglass, embedded in a matrix of partially melted and unmelted grains of quartz sand and limestone. (**E**) A large fragment of vesicular meltglass (at arrow) was removed from the spherule-rich matrix (tan) from the Pond deposit. (**F**) Photomicrograph of spherules embedded in the Pond deposit matrix.

"touch-down airbursts," occur when a bolide explodes sufficiently close to Earth's surface that high-velocity fragments, the shockwave, and the thermal pulse form meltglass, create spherules, generate shocked quartz, and potentially create shallow ephemeral craters [2].

Due to the scarcity of documented cases of airbursts and the frequent lack of evidence preserved in the geologic record, the effects of airbursts are still poorly understood. However, understanding them is vitally important because, as Boslough and Crawford [3, 4] wrote, "*Low-altitude airbursts are by far the most frequent impact events that have an effect on the ground.*" To provide additional insights into airburst processes in the geologic record, we document our discoveries at this new proposed airburst location near Perkins, SW Louisiana (Figure 1).

Methods

We employed standard protocols for eight complementary techniques to characterize spherules, meltglass, and shocked quartz (for more details, see **Supporting Information**, https://zenodo.org/records/15496666 [5]).

1) Optical microscopy (OPT). Transmission microscopy is used for 3D imaging. It also uses crossed polarizers to identify isotropic areas of melted silica in quartz grains. EPI-illumination microscopy (EPI) is used for 3D imaging of spherules and meltglass. It also reveals if a fracture in a quartz grain is filled with material but not the nature of the material.
2) Scanning electron microscopy (SEM): Used to image and analyze spherules and meltglass. It also reveals if quartz fractures are filled with silica without determining if it was melted.
3) Energy dispersive spectroscopy (EDS): A standardless technique used to determine the elemental and oxide compositions of spherules, meltglass, and the quartz fracture-filling material (e.g., melted silica, hydrated silica, carbon, other minerals, or polishing compounds).
4) Laser ablation inductively-coupled plasma mass spectrometry (LA-ICP-MS): A laser beam and mass spectrometer were used to analyze the elemental and isotopic composition of spherules and meltglass.
5) Cathodoluminescence (CL): Used to differentiate between amorphous and crystalline areas of quartz grains; non-luminescent (black) areas indicate melted silica [6–8].
6) Neutron activation analysis (INAA): This nuclear technique measures the elemental concentrations in a material by irradiating it with neutrons and measuring the resulting gamma rays.
7) Universal stage (u-stage): This technique was used to index candidate shocked quartz grains, previously identified using a petrographic microscope. Indexing some quartz grains with a universal stage was problematic because they appeared thermally distorted. However, indexing was possible in those areas where the lamellae remained planar and parallel. The u-stage is considered the definitive technique for identifying shocked quartz.
8) Argon-argon dating ($^{40}Ar/^{39}Ar$): This radiometric dating technique can determine the formation age of rocks that underwent rapid cooling to below their closure temperature since impact-related heating likely reset previous ages. Samples were neutron-irradiated for 6 hours, which is appropriate for ages from 1 Ma to 100 Ma.

Study objectives

1) Material composition: analyze the material with a focus on the morphology and composition of Fe- and Si-rich spherules, meltglass, carbon spherules, melted minerals, and fractured quartz grains, with the latter as a widely accepted indicator of shock metamorphism [2, 9–12].
2) Dating: produce an age-depth model for Trench #1 to determine the age of the spherule-and-meltglass abundance peak and acquire calibrated radiocarbon ages on the carbon-rich meltglass surrounded by very large amounts of spherules. Lastly, determine whether or not the meltglass is co-eval with the spherules and meltglass in Trench #1.
3) Formation conditions: estimate the temperatures and pressures required to produce these materials.
4) Potential formation mechanisms: compare anthropogenesis, authigenesis, volcanism, tectonism, lightning discharges, and cosmic airbursts/impact.
5) Hydrocode modeling: produce a cosmic impact model consistent with the observed evidence.

Results

This section documents our analyses of the wide range of materials observed at the Perkins site. To investigate the characteristics of these materials, we used eight analytical techniques, as described in the **Methods** section. Below, we offer a short introduction before presenting the results for each proxy. Also, to assist in understanding the complex, multidisciplinary data presented in this study, we provide the following Table of Contents of the Results and Discussion sections:

Table of Contents

1. Sedimentology and stratigraphy

Louisiana coastal plain near-surface sediments down to several 100 m typically comprise alternating weakly to well-stratified beds of unconsolidated to semi-consolidated sand, carbonate-cemented sand, limestone, and colored clays [13]. At Perkins, stratigraphic profiles reveal massive, mostly non-laminated, unconsolidated deposits of sand. A sand grain analysis for Trench #1 shows that ~70% of the sediment is fine sand (63-200 µm) (**Supporting Information, Figure S1** [5]), dominated by quartz and limestone grains.

Four primary deposits of glass-and-spherule-rich material were discovered (Figure 2): 1) the Vee deposit in the narrow-V-shaped southwestern end of the lake is ~10 m in diameter and ~30 cm thick; 2) the Pond site northwest of the lake is ~10 m in diameter and ~60 cm thick; 3) a smaller discontinuous deposit of meltglass and spherules was found at the Lake site; 4) Trench #1 on the east rim of the lake contains moderate amounts of glass-and-spherule-rich material. In addition, small amounts of the material were found along some of the roadways and paths where the landowner had placed them.

2. Age of materials

2.1. Radiocarbon dating

We acquired 17 dates, of which six were usable, and eleven were excluded because of insufficient carbon or carbon that was too old or too young (**Supporting Information, Table S1** [5]). To produce an age-depth model for Trench #1, we used OxCal [14], a Bayesian computer program widely used for interpreting radiocarbon dating results by combining radiocarbon dates with prior knowledge, such as archaeological context or stratigraphy. For the Trench #1 model, we used dates on bulk organic material from the 60-75-cm layer that contains the peak in meltglass and spherules and from below the peak in the 105-120-cm layer (Figure 4; **Supporting Information, Table S2** [5]). We also included cultural age ranges for an Early Archaic projectile point (range: ~10,000-8,000 cal BP) and several Late Woodland projectile points (range: ~1,500-1,000 cal BP) [16–18] (**Supporting Information, Table S2** [5]). The modeled age for the spherule-and-meltglass layer in Trench #1 is 12,794 ± 69 cal BP (13,021-12,713 at 95% CI).

We questioned whether the meltglass might contain carbon present at the time of the impact, so we acquired four calibrated ages on carbon-rich fragments of meltglass from the Pond deposit and one for the Vee and compared them to the Trench #1 Bayesian age. Using Oxcal v4.4.4, r:5 [19] with the InCal20 calibration curve, we found that 3 of 6 dates overlap at 99% Confidence Interval (CI; Figure 5; **Supporting Information, Tables S1 and S3** [5]) [20]. Furthermore, the three deposits overlap the YDB age range at 99% CI, as published by Kennett et al. [15].

Radiocarbon dates on bulk meltglass have higher uncertainties than those on charcoal or seeds due to the possibility of younger encroaching roots and mixing with older material, including peat found in the lake and across the area [15, 21–23]. Although this makes assessing synchroneity problematic, given that the key interval at Trench #1 dates to 12,794 ± 69 cal BP, we suggest that the melted material at Perkins resulted from a single cosmic impact event at the YD onset ~12,800 years ago. Thus, the high quality of radiocarbon age for the spherule-and-meltglass layer in Trench #1 takes precedence over the less accurate meltglass ages when inferring an age for the layer.

2.2. Argon-argon dating

The Perkins site lies within the distal ejecta zones of the 65-Ma K-Pg and the 35-Ma Chesapeake Bay impact events. To test the hypothesis that the spherules and meltglass deposits could be from these much older impact events, we performed argon-argon ($^{40}Ar/^{39}Ar$) dating on several aliquots of the spherule-rich matrix from the Vee deposit (**Supporting Information, Table S4** [5]). Every step (including high-temperature steps) yielded almost 100% atmospheric argon, and as a result, the Vee deposits appear young (<2 Ma) and, therefore, are not reworked from these two older impact events or any other known older crater within an ~800-km radius.

3. High-temperature melted spherules

3.1. Spherule abundances

We collected samples from the nine cores, pits, and trenches and then extracted the spherules and meltglass, counted them, and analyzed selected examples. The quantities by depth for the nine locations are shown in Figure 6 and **Supporting Information, Table S5** [5]. Based on field measurements and SEM imagery of spherule-rich samples, the estimated volume of glass-and-spherule-rich material in the Vee deposit totals ~23 m^3, and the Pond deposit is 46 m^3, for a total of 69 m^3. Each m^3 of the material weighs ~1500 kg, so the total mass is >100 tonnes. Quantification using SEM imagery of aliquots of the deposited material revealed that each kg is estimated to contain >100 billion spherules, so, extrapolating conservatively, the total mass of known material includes hundreds of billions of spherules, with the meltglass equaling ~1% of the total or >1 tonne.

The spherule composition from the Vee varies, averaging 7.36 wt% Al, 8.15 wt% Ca, 17.05 wt% Si, and 10.12 wt% Fe with small concentrations of other elements. Scanning

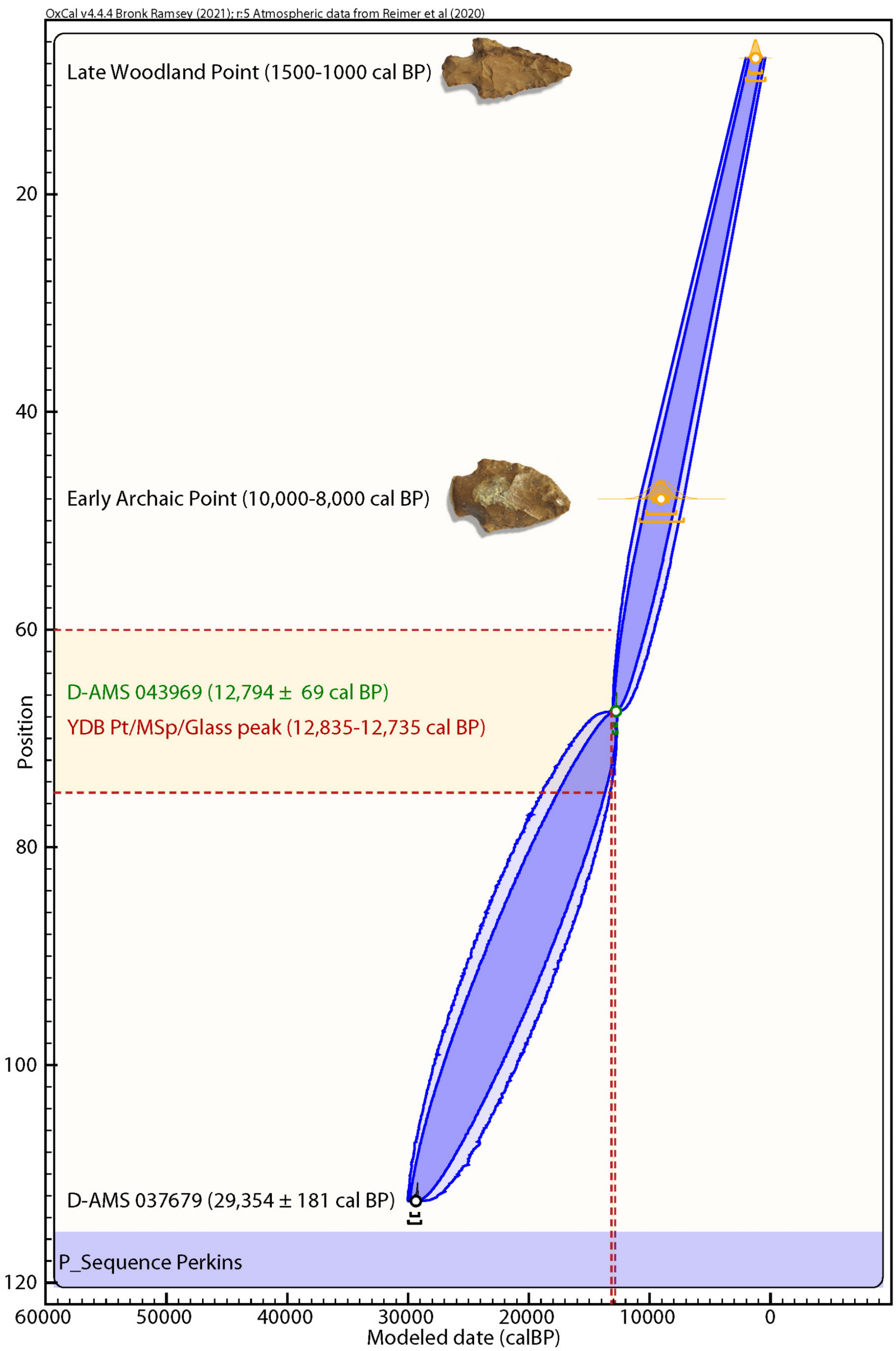

Figure 4: Bayesian chronology for Trench #1. Bayesian age-depth model for the trench (**Supporting Information, Tables S1 and S2** [5]). The model relies on two radiocarbon dates and age ranges for two Native American projectile points. Organic material from the 60-75-cm layer containing the peak in meltglass, microspherules, and shocked quartz dates to 12,794 ± 69 cal BP (13,021-12,713 cal BP at 95% Confidence Interval (CI)), overlapping the proposed range (red dashed lines) of 12,835-12,735 cal BP for the YDB impact event [15]. The model includes a date of 29,354 ± 181 cal BP from organic material at 105-120 cm. The age ranges of the two cultural artifacts are 1,500-1,000 cal BP (Late Woodland culture) and 10,000-8,000 cal BP (Early Archaic culture) [16–18].

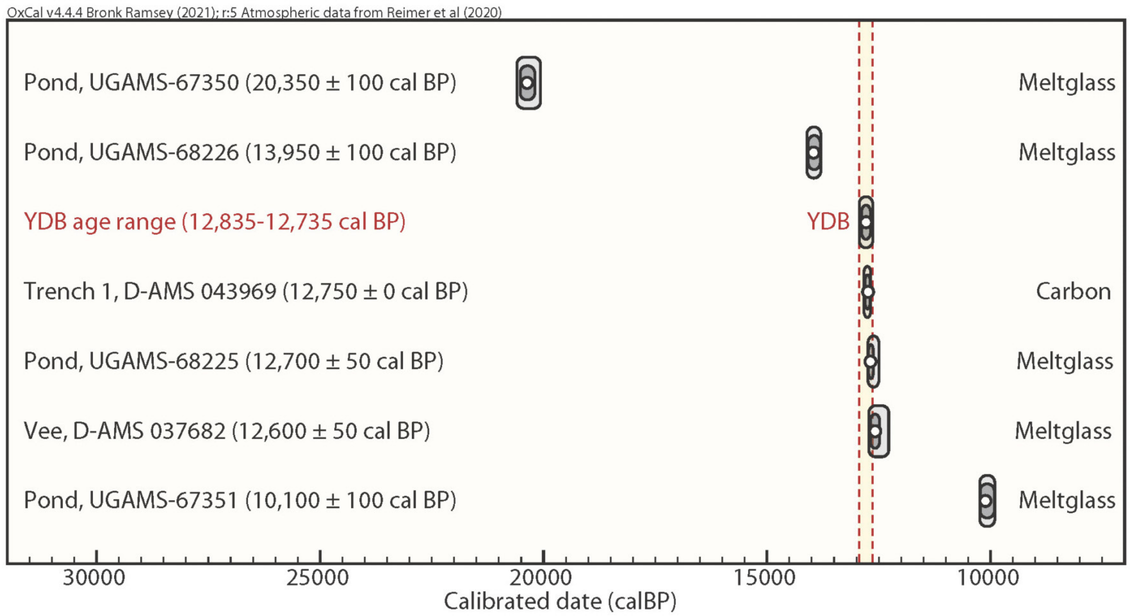

Figure 5: Six calibrated radiocarbon ages for charcoal and meltglass from 3 sites. Meltglass from the Pond and Vee charcoal from Trench #1 were radiocarbon-dated, and these were compared with the proposed YDB age range of 12,835-12,735 cal BP (red dashed lines) [15]. The medium gray bar represents a 95% CI, while the dark gray is a 68% CI. Although the age of the Pond and Vee deposits is unclear, 3 of 6 dates overlap at 99% Confidence Interval (CI), indicating that they could be synchronous within the limits of radiocarbon uncertainties.

electron microscopy with energy dispersive spectroscopy (SEM-EDS) and activation analysis (INAA) reveal that the site's bulk sediment is a variable average mix of Si (31 wt%), Ca (21 wt%), Al (18 wt%), and Fe (16 wt%), totaling ~86 wt% with the remaining 14 wt% comprised of small concentrations of Mn, S, Ti, Na, Mg, K, and P.

3.2. Spherule distribution

The spherule distribution was determined at 11 locations to test whether there was a discernible pattern across the site. The results vary from zero spherules north and south of the lake/depression to a peak abundance of 9200 spherules within the southeastern part of the lake/depression (Figure 7). The isopachs show that spherule concentrations are highest within the lake border but fall off substantially with increasing distance from the lake.

The spherules were plotted by depth across the site, revealing that the largest spherule peak concentrations occur in the lake at depths of up to ~6 m below the surface (Figure 8). Away from the rimmed lake/depression, spherule peaks vary in depth from 0.5 to 1.5 m below the surface. The depth of the deepest part of the lake is unknown; however, two wells, #4 and #6, drilled within ~6 m of the shoreline, encountered alternating layers of multi-colored clay (red through gray colors) down to a depth of ~6 m. At that depth, the well encountered water-saturated fine sand that flowed into the well bore, suggesting that the bore had passed below the bottom of the lake bed. This observation indicates the lake basin is steep-sided at ≥45°, atypical for any known area lake and consistent with the site's lake being an anomalous feature. The rim of the lake/depression is also atypical for any known natural area lake within more than a 50-km radius.

3.3. Spherule morphologies

Regarding spherule morphologies, although we refer to these objects as being spherulitic, they display a wide range of morphologies that include rounded, sub-rounded, ovate, oblate, elongated, teardrop-shaped, dumbbell-shaped, clustered, accretionary, hollow, and broken (Figures 9–12). An analysis of ~100 spherules reveals that their diameters range from ~1 to 65 µm with an average of 14 µm (**Supporting Information, Figure S2** [5]). Colors include clear, white, red, orange, purple, brown, and black; they can be opaque, translucent, or transparent. Surface textures vary widely, including smooth, dendritic, platy, soccer-ball-like, reticulated, and irregular. When sectioned or broken, the spherules most commonly display one or more large vesicles, but some are solid. The spherules sometimes display multi-phase morphologies (Figures 9 and 10) and may contain relict grains of quartz. The Fe-rich spherules are often depleted in oxygen, which is consistent with being wüstite and sometimes approaches the composition of native iron (Figure 10).

Multi-layered glassy spherules were observed with similar morphologies to those previously reported for impact events [24, 25]. Many of them contain fragments of stoichiometric crystalline quartz surrounded by either melted quartz or Ca-rich aluminosilicate glass. Several contain an overgrowth of ettringite, a likely post-depositional mineral.

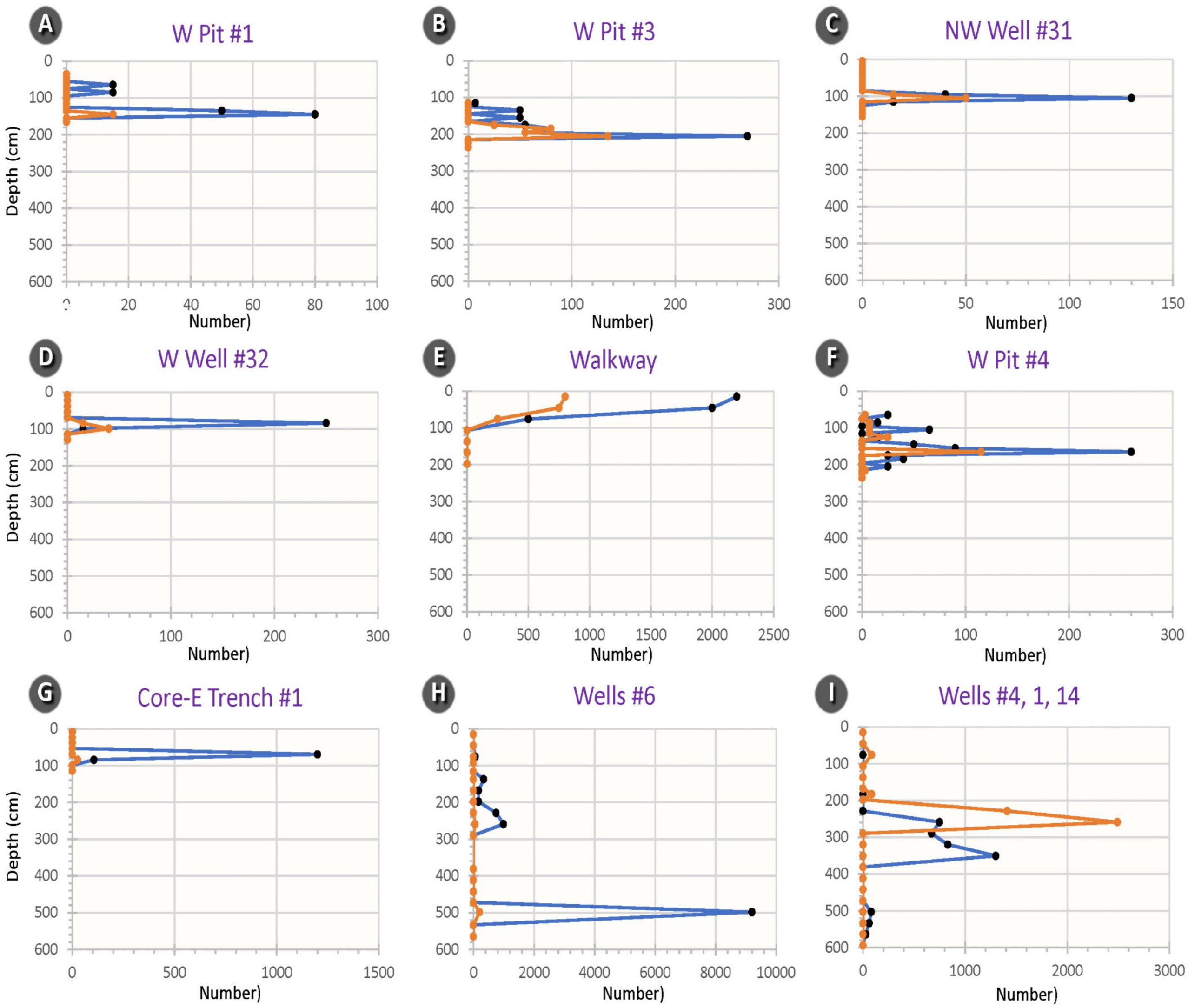

Figure 6: **Abundances by depth for spherules and meltglass.** See Figures 2 and 7 below for the nine sampling locations in and around the lake/depression. The blue lines represent spherules, and the orange lines represent meltglass.

Summary of Spherule Evidence

- Deposits contain **>100 tonnes** of spherules.
- Estimated **>100 billion spherules per kilogram**.
- Morphologies include **rounded, sub-rounded, dumb-bell, hollow**, and **clustered** forms.
- **Elemental composition**: Primarily Fe, Si, Al, and Ca.
- **Spatial distribution**: Spherule concentrations are highest within the lake/depression, declining radially.
- **Depth profile**: Deeper spherule peaks (up to 6 m) in the depression's center, consistent with ejecta fallback.

4. Carbon spherules and glasslike carbon

We observed multiple varieties of these carbon-rich particles, with colors including black, tan, and amber; transmissivity including opaque, translucent, and transparent; and shapes including spherical, oval, and broken. The abundance of carbon spherules in the Vee and Pond meltglass was ~500/kg with diameters ranging from ~100-800 µm, averaging ~600 µm (Figure 13). The glasslike carbon fragments were typically multiple millimeters in size with approximately the same abundance as the carbon spherules. The spherules and glasslike carbon are dominantly carbon (up to ~80 wt%) combined with small concentrations of Fe, Si, and O (Figure 14).

Summary of Carbon-Rich Spherules and Glasslike Carbon

- Carbon spherules (opaque, translucent) and glasslike carbon fragments were found.
- Enriched in platinum-group elements (PGE): Os, Ir, Pt.
- Meltglass carbon content suggests lower peak formation temperatures than metallic or silicate melts.

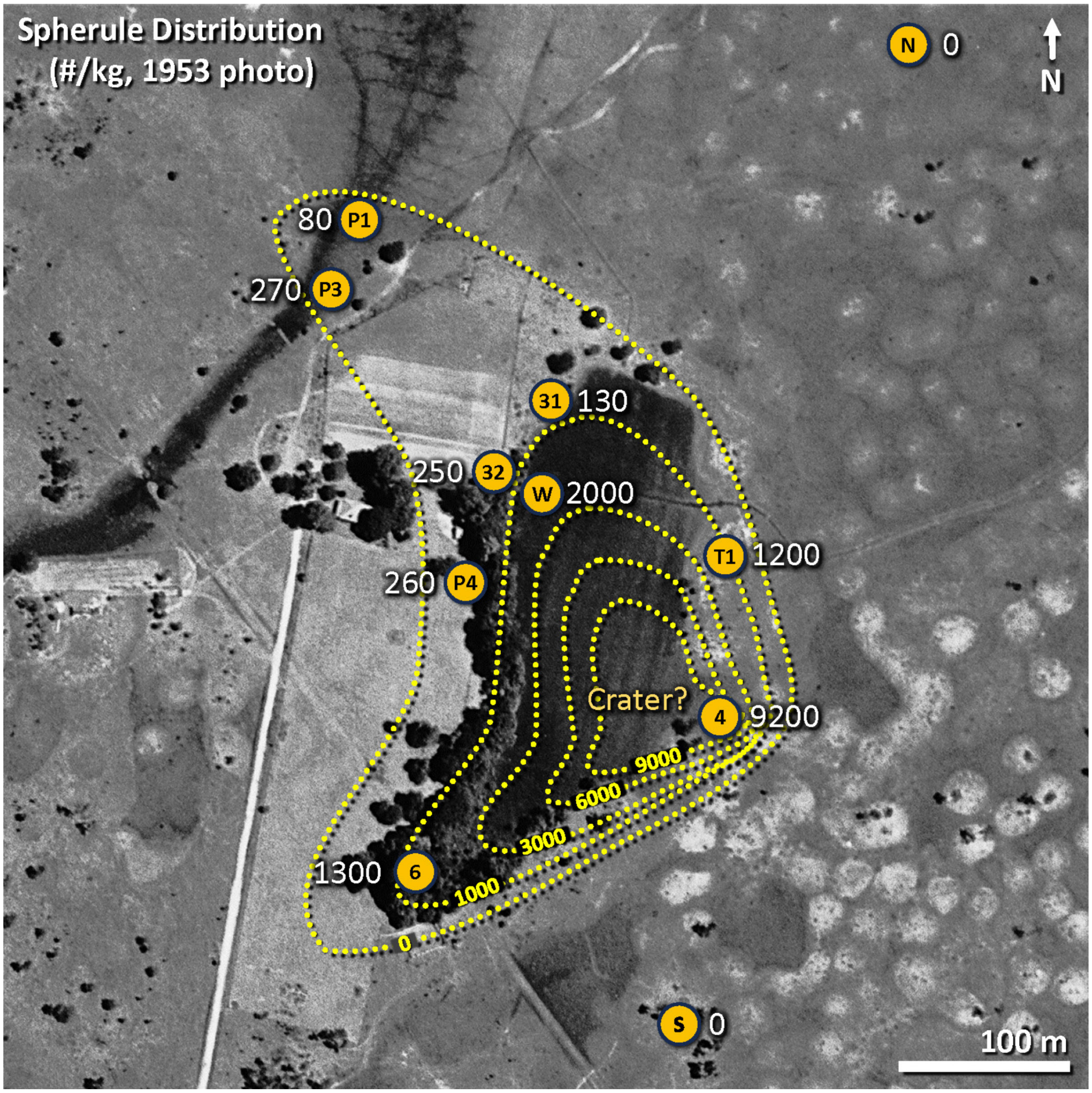

Figure 7: **Spherule isopach diagram of spherule distribution.** Numbered circles represent 11 sampling locations, and white numbers represent the peak abundance of spherules, ranging from 9200 in core 4 to none north and south of the lake. P1, P3, and P4 indicate three excavated pits; T1 is Trench #1; circles numbered 4, 6, 31, and 32 correspond to small-bore coring locations; N and S represent north and south coring locations. The isopachs reveal that spherule abundances are the largest in the lake and decline with distance away from it. Image from USGS; imagery date: 1983; accessed: 8/8/2024. Figure composited using Microsoft PowerPoint 2021.

5. Meltglass

The meltglass elemental abundances vary but are mostly Fe-rich Ca-aluminosilicates. The meltglass from Trench #1 and the Vee deposit averages 9.64 wt% Al, 14.97 wt% Ca, 17.42 wt% Si, and 8.71 wt% Fe, with small concentrations of other elements (**Supporting Information, Tables S6 and S7** [5]). These irregular, broken objects display a wide range of textures, including smooth, rounded, folded, layered, and granular; most are highly vesicular (Figures 15–21). Dimensions range from sub-cm to a 31-cm-long meltglass rock weighing 16.33 kg. Colors vary from clear, white, red, orange, purple, brown, and black. They are primarily opaque but can appear translucent, as with numerous mm-sized, white, vesicular fragments that reached an abundance peak in Trench #1 at 12,794 ± 69 cal BP. Sand grain analyses for Trench #1 reveal that the abundance peak in meltglass corresponds to a nearly doubling of the fine silt component (<40 µm; **Supporting Information, Figure S1** [5]).

Abundances of meltglass fragments from nine cores, pits, and trenches are shown in Figure 6. Meltglass fragments, like many spherules, are typically composed of aluminosilicates (Al, Ca, Si, and O), although they commonly contain small amounts of other elements, including C, Fe, Zr, Ti, Ni, Co, Cr, and PGEs. Variations in concentrations of these

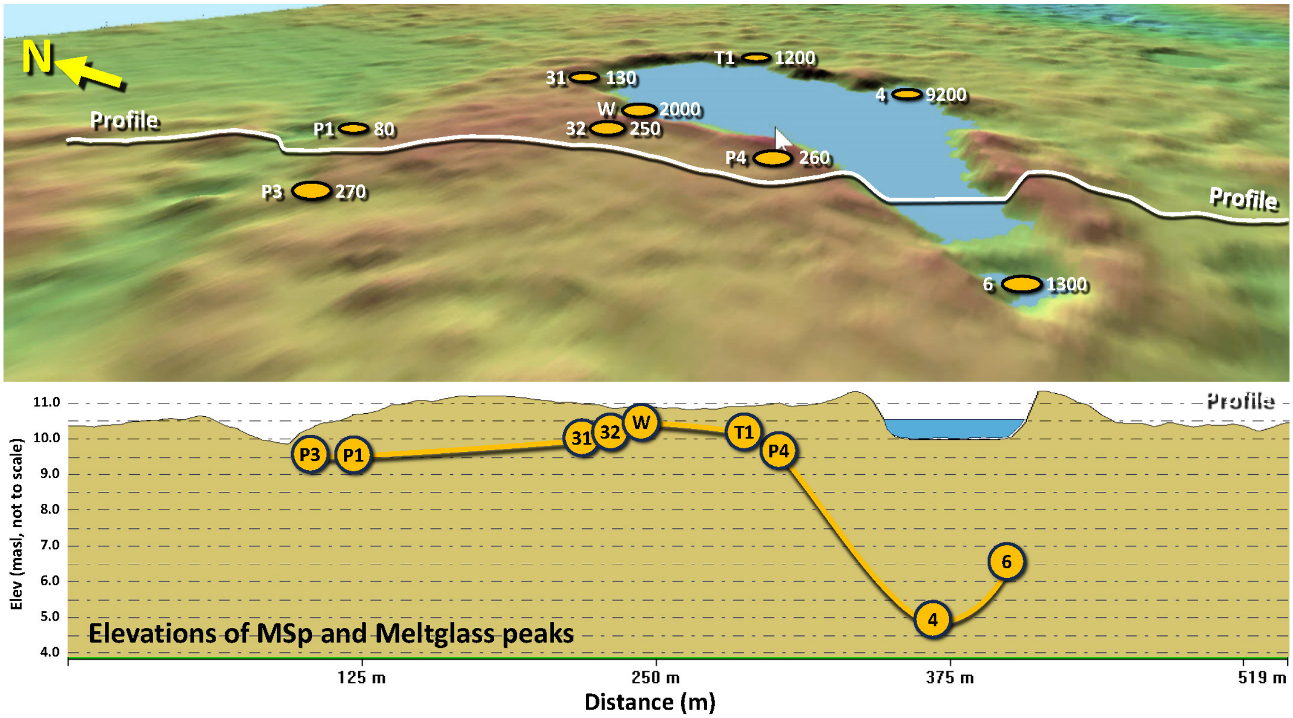

Figure 8: Profile across lake/depression showing spherule peak by depth. Peak abundances of spherules plotted by depth. Peaks become substantially deeper by up to ~6 m below the surface within the lake/depression. Note the distinctive raised rim around the lake, which is anomalous for lakes within this region. The sediment-filled lake is estimated to have had an original depth of ~25 m, as discussed in the hydrocode modeling below. For the LiDAR base image, the vertical scale is exaggerated several times. P3 = Pit #3; P1 = Pit #1; 31 = Well #31; 32 = Well #32; W = Walkway; T1 = Trench #1; P4 = Pit #4; 4 = Well #4; and 6 = Well #6. Base figures created with Global Mapper, v. 8.0.

elements affect the spherule morphology. Some fragments comprise >80% carbon and are more similar to glasslike carbon. Many meltglass fragments display high-temperature melted or boiled minerals, including magnetite (1590°C), NiCr-magnetite (1590°C), zircon with baddeleyite (1775 to ≥4400°C), kaolinite (1770°C), clinopyroxene (1150°C), and quartz (~1710 to ≥2230°C) (Table 1).

Summary of Meltglass Evidence

- Estimated **>1 tonne** of meltglass across the site.
- Composed mainly of melted **Fe- and Ca-aluminosilicates**.
- **Textural evidence**: Highly vesicular, layered, folded, tubular, and flowed structures.
- **Thermal evidence**: Mineral inclusions suggest melting temperatures **≥1590–4400°C**.

6. Low-oxygen metallic flakes

These typically flake-like objects were analyzed using SEM/EDS. They ranged from ~38 to 818 µm in diameter, averaging ~200 µm with an abundance of ~100 particles/kg (Figure 22). They are typically composed of troilite, native iron (Fe), wüstite (FeO), reduced iron (Fe^{2+}; i.e., oxygen-depleted), and chromian magnetite, all of which are common ET materials. The morphologies include flat, flake-like, or curved forms that sometimes appear folded and melted along the edges. Similar oxygen-depleted flakes have been reported to be cosmic dust particles, most likely cometary in origin [27–32].

Summary of Low-Oxygen Metallic Flakes

- Discovery of **oxygen-depleted metallic flakes** composed of native iron, troilite, and wüstite.
- Morphologies (folded, melted edges) and chemistry consistent with **extraterrestrial (ET) origin.**
- Rare on Earth, common in ET and impact-related materials.

7. High-temperature/high-pressure quartz

7.1. Shocked quartz grains with glass-filled fractures

The similarities and differences between these four types of lamellae/fractures are summarized in Table 2. We investigated grains optically in 14 levels from 35-165 cm in Trench #1, in addition to samples from the Vee and Pond deposits. In Trench #1, shocked quartz was observed in the 12,794 cal BP YDB layer, not above or below. Shocked quartz candidate grains were selected, thin-sectioned, and further analyzed. Optical microscopy, SEM, and CL reveal

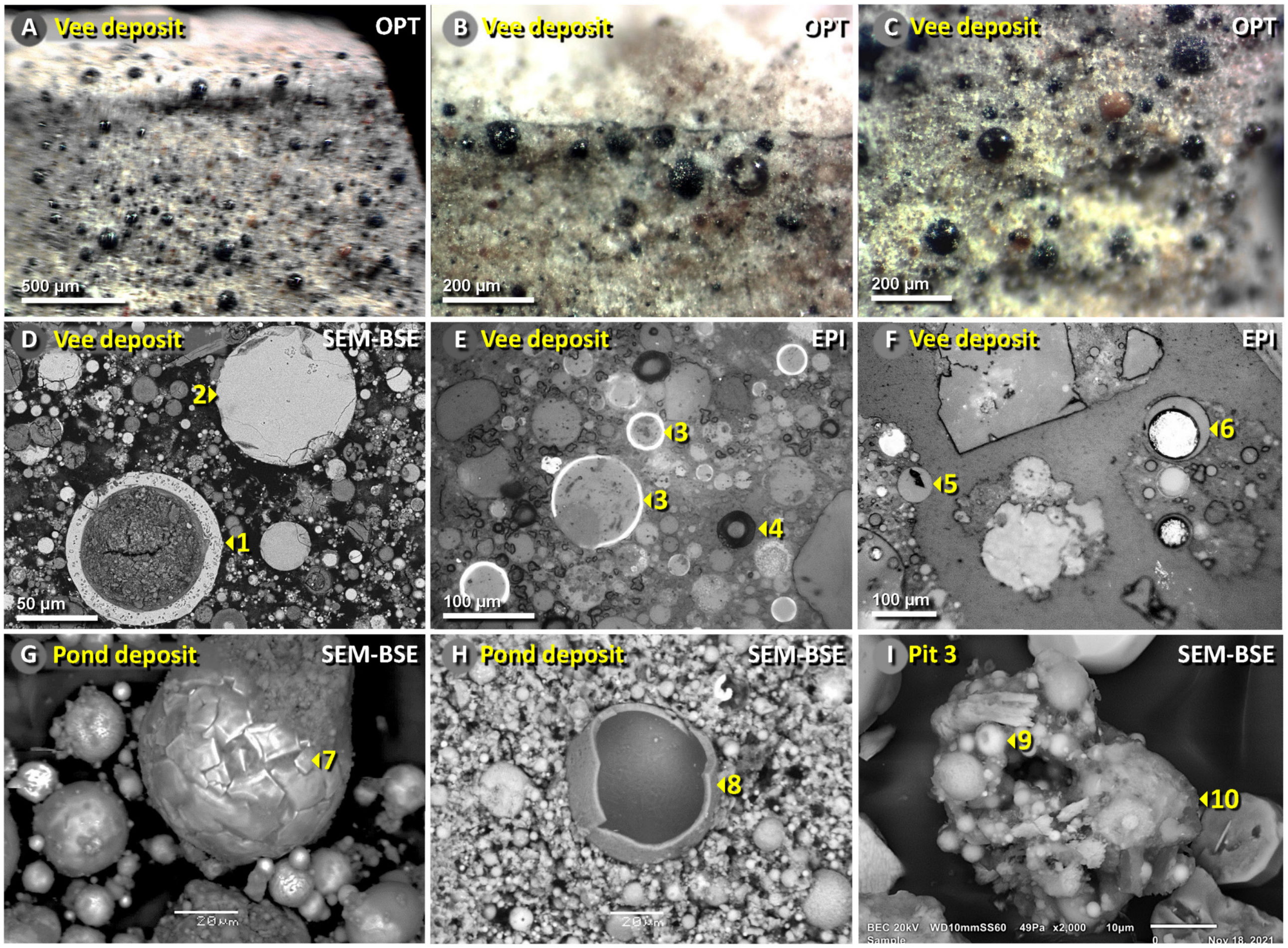

Figure 9: Spherules from various deposits from several locations. (A-C) Photomicrographs of the surfaces of a block of semi-consolidated, spherule-rich matrix. Spherules and meltglass comprise >90 wt% of the spherule-rich matrix. **(D-F)** SEM-BSE image and with two epi-illuminated photomicrographs (EPI) of the thin-sectioned spherule-rich matrix. Panels D and E exhibit ~800 spherules, representing ~1.8 million spherules/cm^2. In panels D-E, #1 and #3 indicate hollow spherules surrounded by a brighter Ca-Al-Si-Fe coating, added after the spherule was quenched. In panel D, #2 marks a solid Ca-Al-Si-Fe spherule. In panel E, #4 marks an Al-Si-rich spherule surrounded by a carbon coating. In panel F, #5 marks an Al-Si-rich spherule, and #6 marks a bright metallic core surrounded by a gray Si-rich coating. **(G-I)** SEM-BSE images of spherules within the matrix. In panel G, #7 is an Fe-rich spherule with a platy texture. In panel H, #8 is a hollow Al-Si-rich spherule surrounded by hundreds of smaller spherules. In panel I, #9 marks a small, hollow spherule a few microns in diameter, and #10 marks an elongated Fe-rich object.

evidence of extensive fractures and lamellae (12 in ~25,000 grains). We observed four types of microstructures in quartz in this study: classical planar deformation features (PDFs), classical planar fractures (PFs), and glass-filled non-planar fractures (herein termed "nPFs") (Figures 23–28). We also observed but ignored non-shock deformation lamellae (DLs) [9, 34–38], which typically result from tectonic motion, but tectonism does not produce glass along the deformation lamellae.

Melted silica within quartz grains takes two forms: (i) diaplectic glass that forms when quartz undergoes shock-induced, solid-state transformation into an amorphous state by mechanical pressure rather than through high-temperature melting, and (ii) amorphous silica, also called lechatelierite, that melts at high temperatures at any pressure. Both forms of melted silica within quartz grains are called "glass" in this contribution. The presence of melted silica within shocked quartz is a characteristic that makes glass-filled shocked quartz a reliable indicator of cosmic impact events [9]. Indeed, French and Koeberl [38] emphasized the primary importance of melted silica in PDFs. They wrote, "*Most striking, and most diagnostic of shock-wave pressures and impact conditions, are the unusual planar deformation features (PDFs) that have served reliably as an impact indicator for several decades.*"

Nearly all shocked quartz grains at Perkins display regions of amorphous silica, typically along lamellae and around the grain edges, and most show evidence of having been thermally warped after being shocked. One shocked quartz grain (Figure 23B) was observed within a matrix containing thousands of spherules adhering to its surface, confirming a close relationship between spherule formation and shocked quartz.

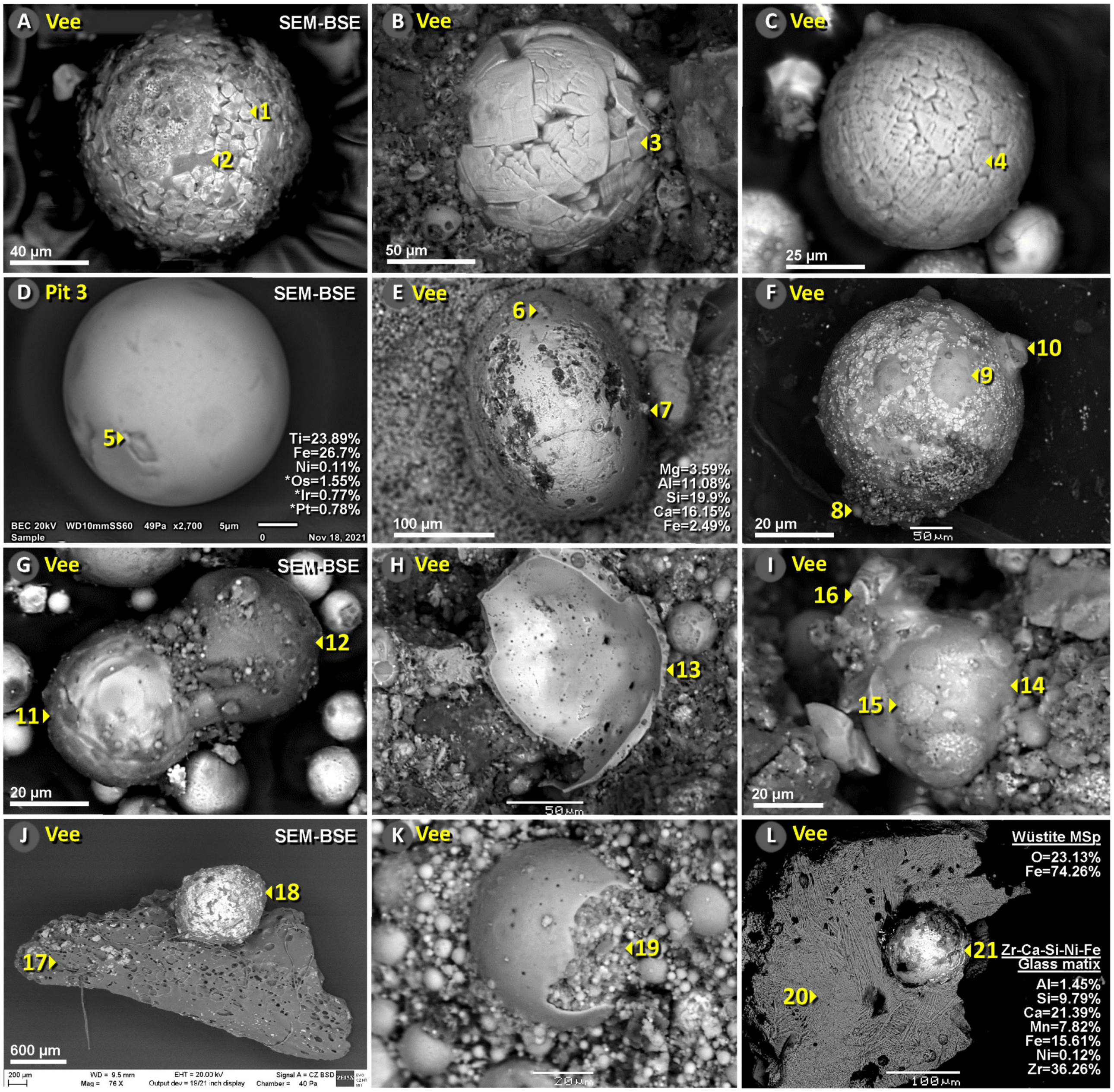

Figure 10: **SEM images of Fe- and Al-Si-rich spherules.** All are from the Vee deposit, except panel D, which is from Pit 3. **(A)** #1: Platy texture characteristic of Fe-rich spherules, covering an Al-Si-rich core at #2. **(B-C)** #3: Platy textures and #4 dendritic textures on Fe-rich spherules, surrounded by spherule-rich matrix. **(D)** #5: Impact pit on spherule; Ti-mag enriched in Ni, Os, Ir, and Pt. **(E)** #6-7: Splashes of once molten material draped across an Al-Ca-Si spherule. **(F)** #8: A cluster of sub-micron spherules splashed onto the large spherule. #9: Fe plates cover an Al-Si core. #10: smaller secondary collisional spherule, dimpled due to high-velocity impact while molten. **(G)** #11: Fe-rich spherule that collided with #12, an Al-Si-rich spherule. **(H)** #13: A broken shell of an Al-Ca-Si spherule. **(I)** #14: Large, multi-phase Al-Si spherule that collided with #15: smaller Fe-rich spherules. #16: agglutinated material. **(J)** #17: Vesicular glasslike carbon with embedded #18: Fe-rich spherule. **(K)** #19: Hollow Al-Si spherules surrounded by and filled with hundreds of smaller spherules. **(L)** #20: Zr-Ca-Si-Ni-Fe glass with #21, an embedded wüstite (FeO) spherule.

7.2. Thermally warped quartz grains

When quartz grains undergo shock metamorphism that creates glass-filled PDFs, PFs, and fractures, they may undergo additional transformation when exposed to high temperatures from the impact fireball. This process can partially melt and warp the grains, leaving the lamellae still visible though non-planar, i.e., bent or curved (Figures 23–26).

Some quartz grains display regions of isotropy when using crossed polars. Often, the grains are coated with a thin

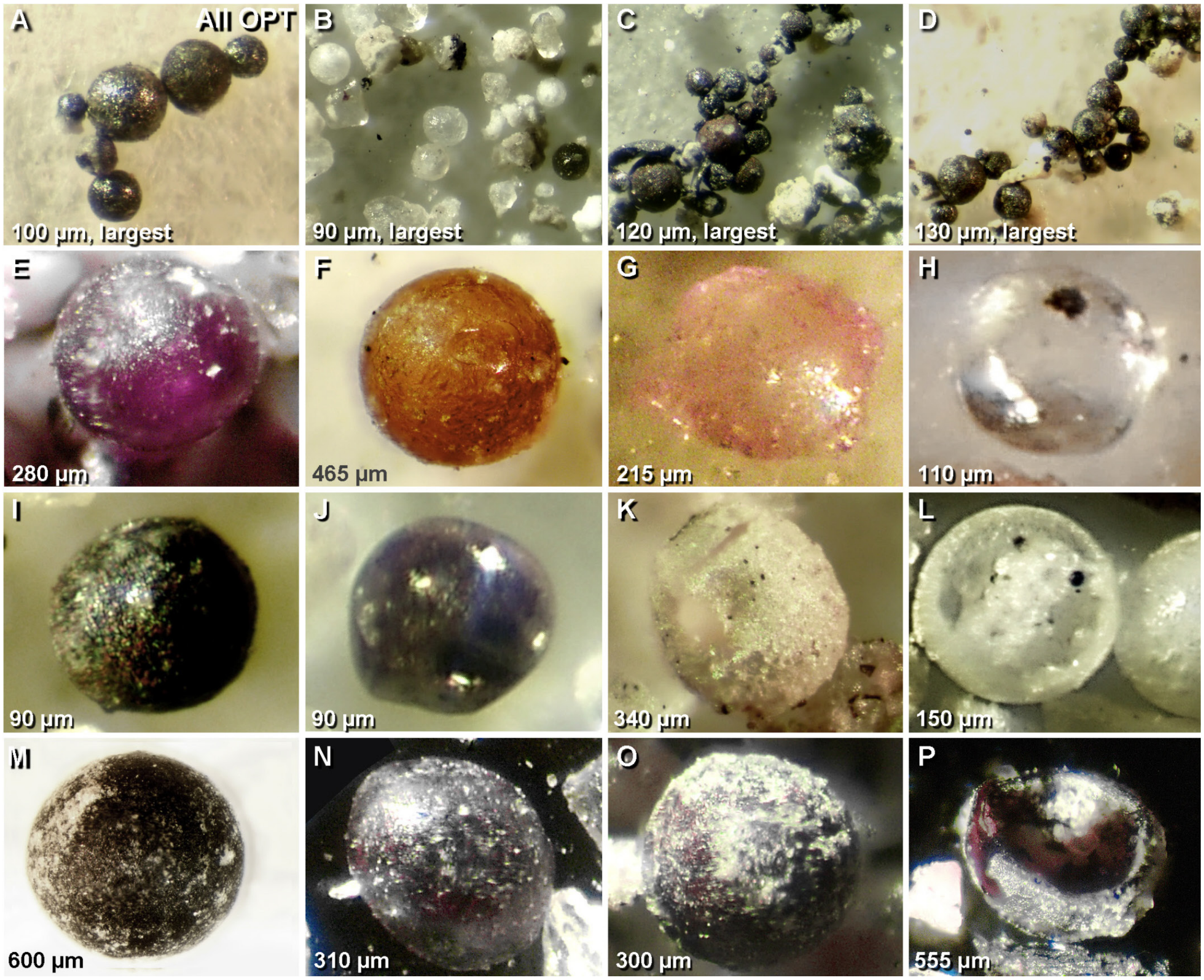

Figure 11: **Spherules extracted from the Vee deposit.** All optical photomicrographs. (**A-D**) Clusters of Fe- and Al-Si-rich spherules. (**E-K**) Multiple colors of glassy Ca-Al-Si-Fe-C-rich spherules. (**L**) Hollow, broken, glassy spherule containing numerous sub-micron spherules. (**M-O**) Dark-colored glassy Ca-Al-Si-Fe-C-rich spherules. (**P**) Hollow, broken, dark-colored, glassy Ca-Al-Si-Fe-C-rich spherule.

layer of isotropic material, consistent with noncrystalline silica (glass), and they commonly display non-planar and planar fractures filled with melted silica (Figure 26). SEM and SEM-EDS confirm that the red areas are not microcrystalline quartz (e.g., chalcedony), cryptocrystalline quartz (e.g., chert), or quartz overgrowth or cement (hydrated silica), and therefore, are melted silica.

7.3. Miller-Bravais indices confirm shocked quartz

PDFs and PFs have been reported to display characteristic angles relative to the plane of the c-axis in quartz [9, 38–40], and these angles can be measured in polished thin-sectioned slides using a universal stage [41–43]. For the Perkins shocked quartz candidates, the measured angles were plotted in Figure 27 using the ANIE software program [42, 44]. The indices observed match the most common crystallographic orientations of planar microstructures in shocked quartz [9].

Summary of Shock Metamorphism in Quartz

- Presence of **planar deformation features (PDFs)**, **planar fractures (PFs)**, and **non-planar glass-filled fractures (nPFs)**.
- Thermally warped quartz grains were observed, indicating **post-shock heating**.
- **Universal stage measurements** match known shock-induced crystallographic orientations.
- **Shock evidence rate**: ~1% of all quartz grains examined.

7.4. Microbrecciated quartz grains

This term indicates that quartz grains have undergone brecciation, a process in which the grains are broken into angular

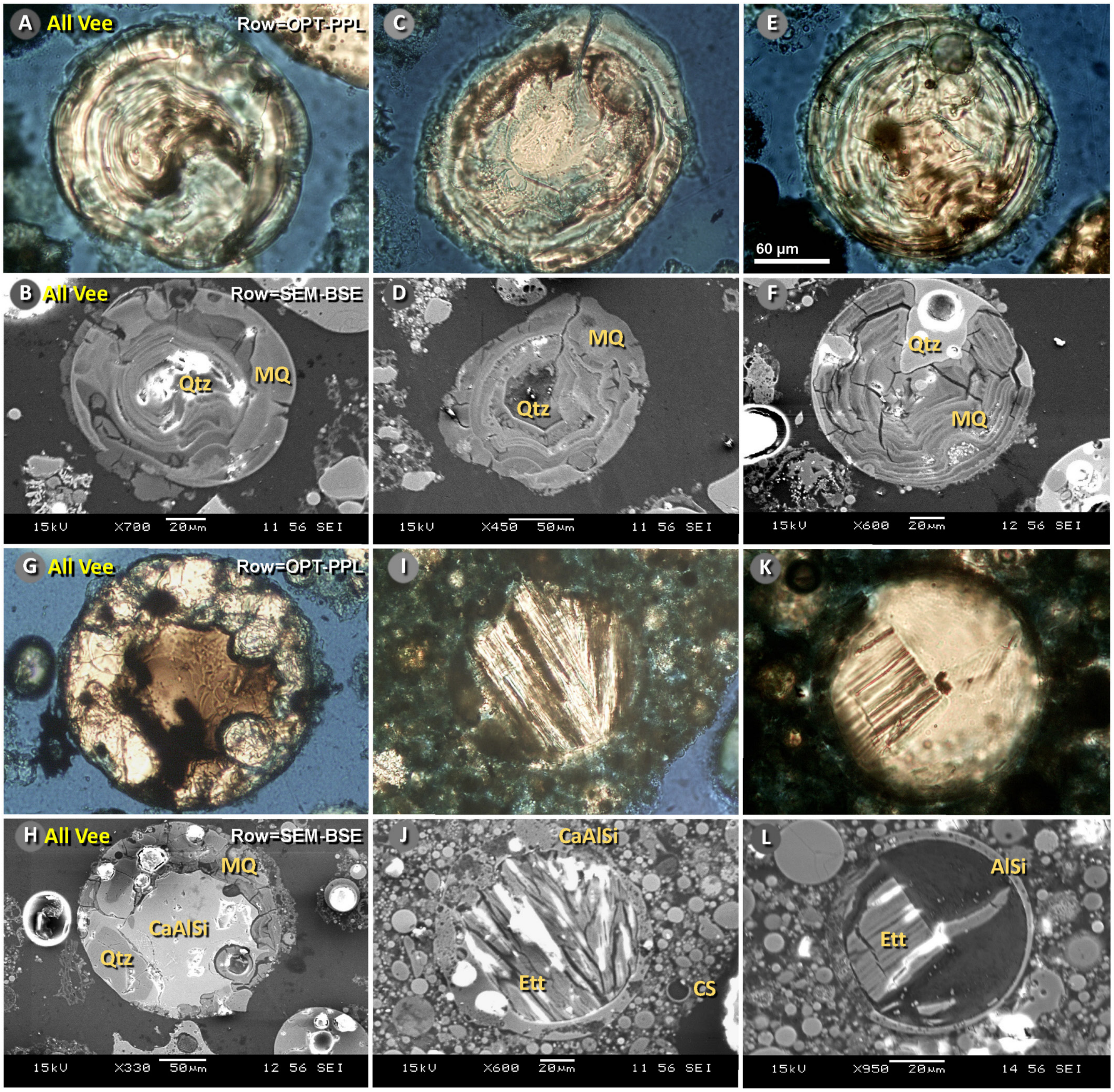

Figure 12: Multi-layered Vee spherules. Rows 1 and 3 are optical photomicrographs under plane-polarized light (OPT-PPL); rows 2 and 4 are SEM-BSE images of the corresponding spherules. "Qtz" indicates stoichiometric crystalline quartz, and "MQ" represents melted quartz. **(A)-(B), (C)-(D)**, and **(E)-(F)**. Multi-layered spherules comprised of melted quartz with crystalline quartz inclusions. **(G)-(H).** Multi-component spherule comprised of CaAlSi glass, melted quartz, and crystalline quartz. **(I)-(J)** and **(K)-(L).** Hollow CaAlSi spherule filled with likely post-depositional material (O = 61.27 Wt%, Al = 5.90 Wt%, Si = 0.65 Wt%, S = 7.99 Wt%, and Ca = 24.19 Wt%).

to rounded fragments that are then bonded together by a mineral cement or melted material. This phenomenon is typically observed in high-stress environments, such as fault zones at a macro-scale, volcanic eruptions at a macro-scale, and impact craters at micro- and macro-scales.

During an impact event, the cement in quartz grains commonly comprises isotropic, amorphous, and often vesicular silica. Sometimes, the entire quartz grain is melted, and as the molten quartz cools, it re-crystallizes into aggregates, with each globule representing a different crystallite [45, 46]. In some cases, the aggregates crystallize into spherical shapes; however, in other cases, they become sub-spherical, such as those observed in the Vee deposit (Figure 28). If the molten cement is quartz in a quartz grain, the grain is referred to as monomict quartz microbreccia; if the material is composed of other elements, the grain is referred to as polymict quartz

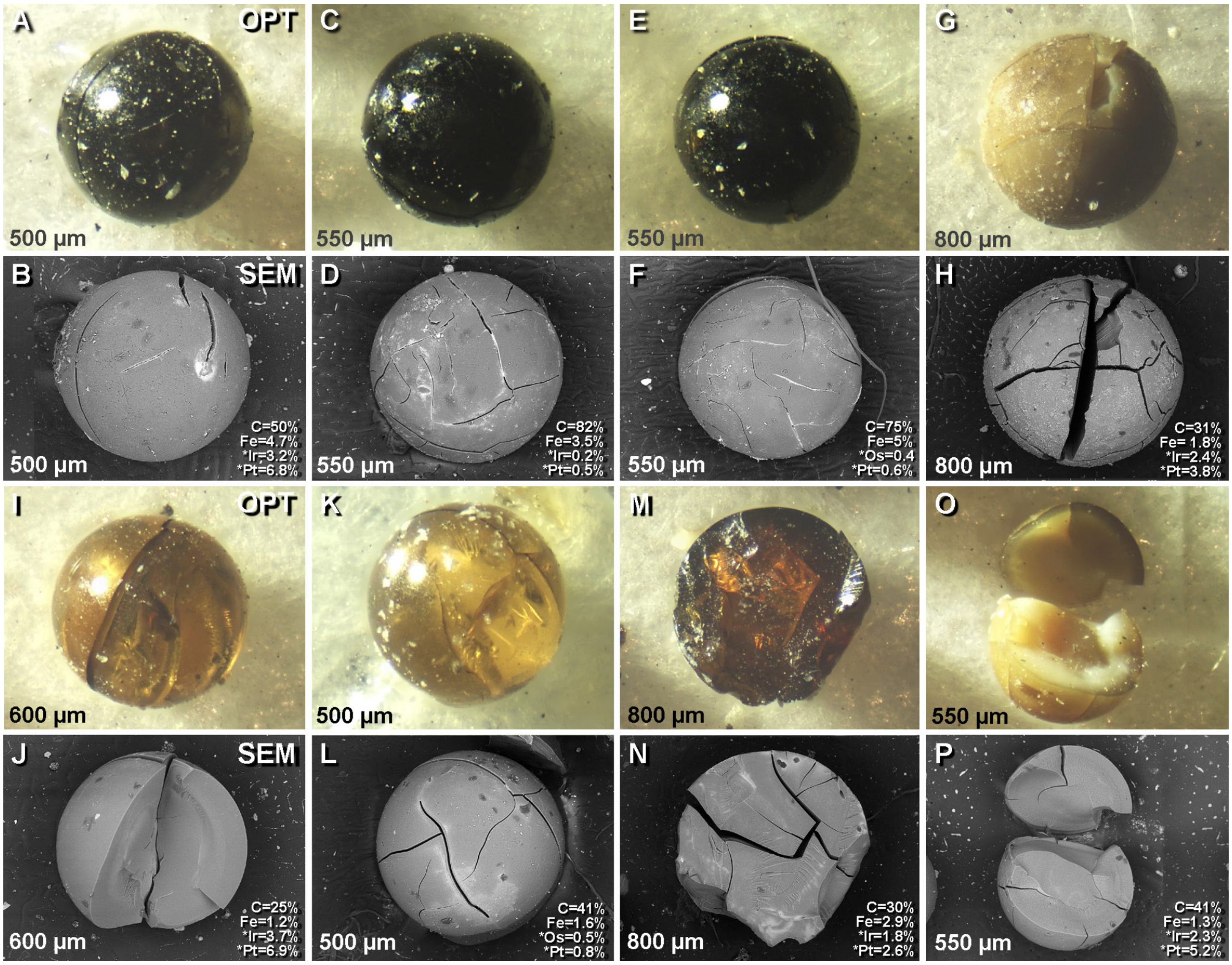

Figure 13: Pond carbon-rich spherules containing Fe and PGEs. (A,C,E,G,I,K,M,O) Color photomicrographs using an optical microscope (OPT). **(B,D,F,H,J,L,N,P)** Corresponding SEM-BSE images are below each color image. These mixed composition carbon-rich spherules (range: 25 to 82 wt% C) also contain Al, Ca, Si, and Fe, along with PGEs, Os, Ir, and Pt, as shown. Ranges of PGE SEM-EDS percentages: Os = 0.4 to 0.5 wt%; Ir = 0.2 to 3.7 wt%, and Pt = 0.5 to 6.9 wt%. SEM-EDS percentages are too high and, therefore, should be considered qualitative. Other spherules quantitatively measured with laser-ablation ICP-MS confirm that all spherules analyzed are enriched in PGEs, not in the percent range but in the ppm range at 300 to 1000× above crustal values.

microbreccia. Shocked quartz has previously been observed in monomict quartz breccia associated with Libyan Desert Glass [47] and in the YDB-aged site, Abu Hureyra, Syria [26].

Summary of Microbrecciated Quartz

- Microbrecciation within quartz grains bonded by amorphous silica.
- Indicative of **extreme stress and shock conditions** associated with impacts.

8. Magnetic survey

If the lake/depression is an impact crater, we reasoned that there may be associated magnetic total field anomalies due to potentially higher Fe concentrations produced by the impactor. We tested this hypothesis by conducting two magnetic surveys on the lake/depression across two wing-like features, similar to the pattern produced by the Tunguska airburst [48, 49], the Saarland structure airburst [50], and rays of secondary ejecta on the Moon and Mars [51]. We found positive magnetic anomalies associated with each wing (Figure 29), consistent with similar patterns related to other known impact structures that typically show magnetic intensity variations ranging from a few nT to several hundred nT [52]. These magnetic signatures may result from several impact-related processes: (i) The concentration of magnetic minerals through ballistic sorting during ejection and deposition; (ii) the thermal alteration of iron-bearing minerals during the impact event, potentially producing new magnetic phases through heating and rapid cooling; and (iii)

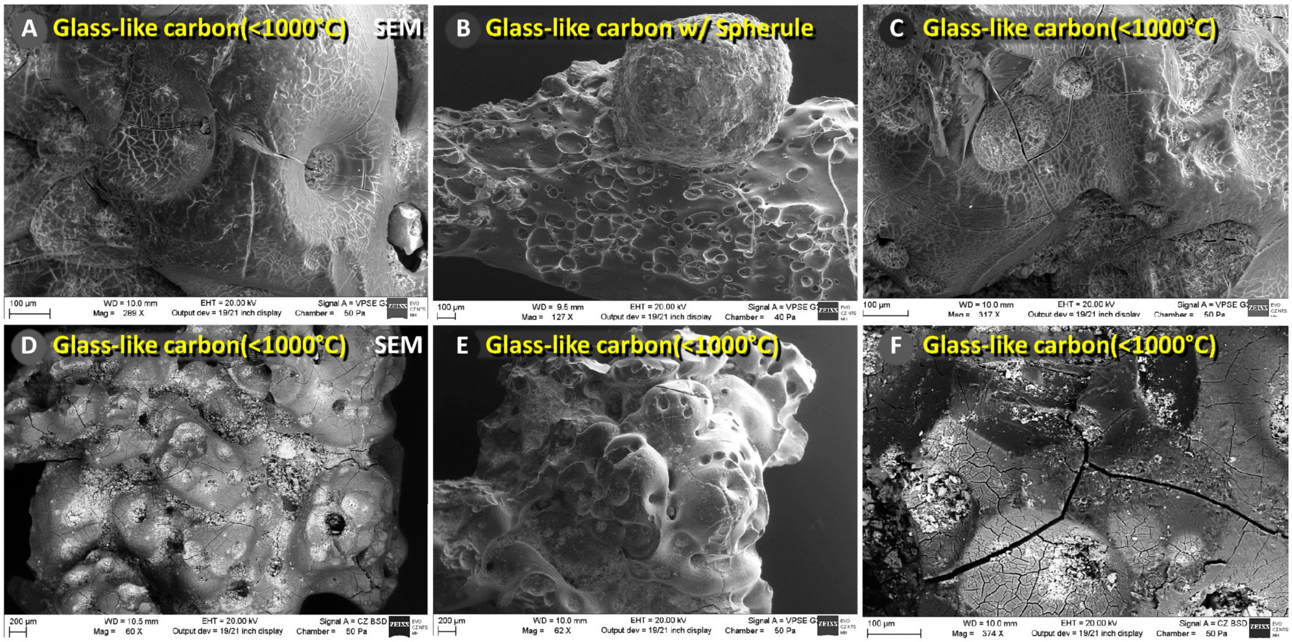

Figure 14: SEM-BSE images of Al-Si-rich meltglass and glasslike carbon from the Vee deposit. (A-C) Fragments of meltglass that most likely melted at ≥1250°C [26]. Panels A and C are from pit #3; panel C is from the Vee. **(D-I)** Fragments of glasslike carbon from the Vee deposit most likely melted at <1000°C, although all were surrounded by numerous spherules, including Fe-rich ones that melted at ≥1538°C, the melting point of iron.

possible contributions from impactor material, as suggested by the elevated Ni/Fe and Cr/Fe ratios that we found in the spherules and meltglass.

Alternatively, there are multiple relict braid-plain stream channels across the area, so the lake/depression and wing-like features could be due to past fluvial action and only coincidentally associated with the spherule-and-meltglass deposits. However, other local lakes do not display wing-like features or raised rims, as is typical for impact craters. The magnetic data, combined with the morphological and geochemical evidence, provides additional indirect support for the lake/depression being an impact crater, although the magnetic evidence is inconclusive.

Summary of Magnetic Survey Results

- **Positive magnetic anomalies** were detected along "wings" extending from the depression.
- Morphology and magnetic signals are similar to known secondary ejecta patterns on the Moon, Mars, and Tunguska.
- **Alternative fluvial explanations** are possible but questionable due to the absence of similar features nearby.

9. Summary of analytical results for all proxies

The table below summarizes the results for the Perkins site (Table 3), and Figure 30 provides a visual flowchart to illustrate the complex, multidisciplinary data presented in this study.

Discussion-interpretation

The two large glass-and-spherule deposits at the Vee and Pond locations are at the surface and not *in situ.* However, small quantities of spherules and meltglass exhibiting the same morphologies and geochemistry occur *in situ* in the ~12,800-year layer of Trench #1. In this section, we consider several issues related to the Perkins site.

i. How old are the spherule-and-meltglass deposits that had been relocated?
ii. Are these deposits related to or unrelated to the lake/depression?
iii. What processes produced the site's spherules, meltglass, breccia, and shocked quartz?

10. Age of the Perkins materials

The Bayesian-modeled age of the *in situ* spherule-and-meltglass deposit in Trench #1 is well constrained at 12,794 ± 69 cal BP, and the ages of some meltglass in Vee and Pond deposits overlap at 95% CI. We acquired six radiocarbon dates on carbon-rich material from the Vee and Pond deposits, but the dates did not definitively constrain the age of the deposits. Large carbon spherules from the Vee meltglass date to >28,000 cal BP, and six radiocarbon dates on large peat-like carbon-rich material extracted from the Vee and Pond deposits were all older than 42,000 cal BP. The reason for the old ages is unclear, but we speculate that when

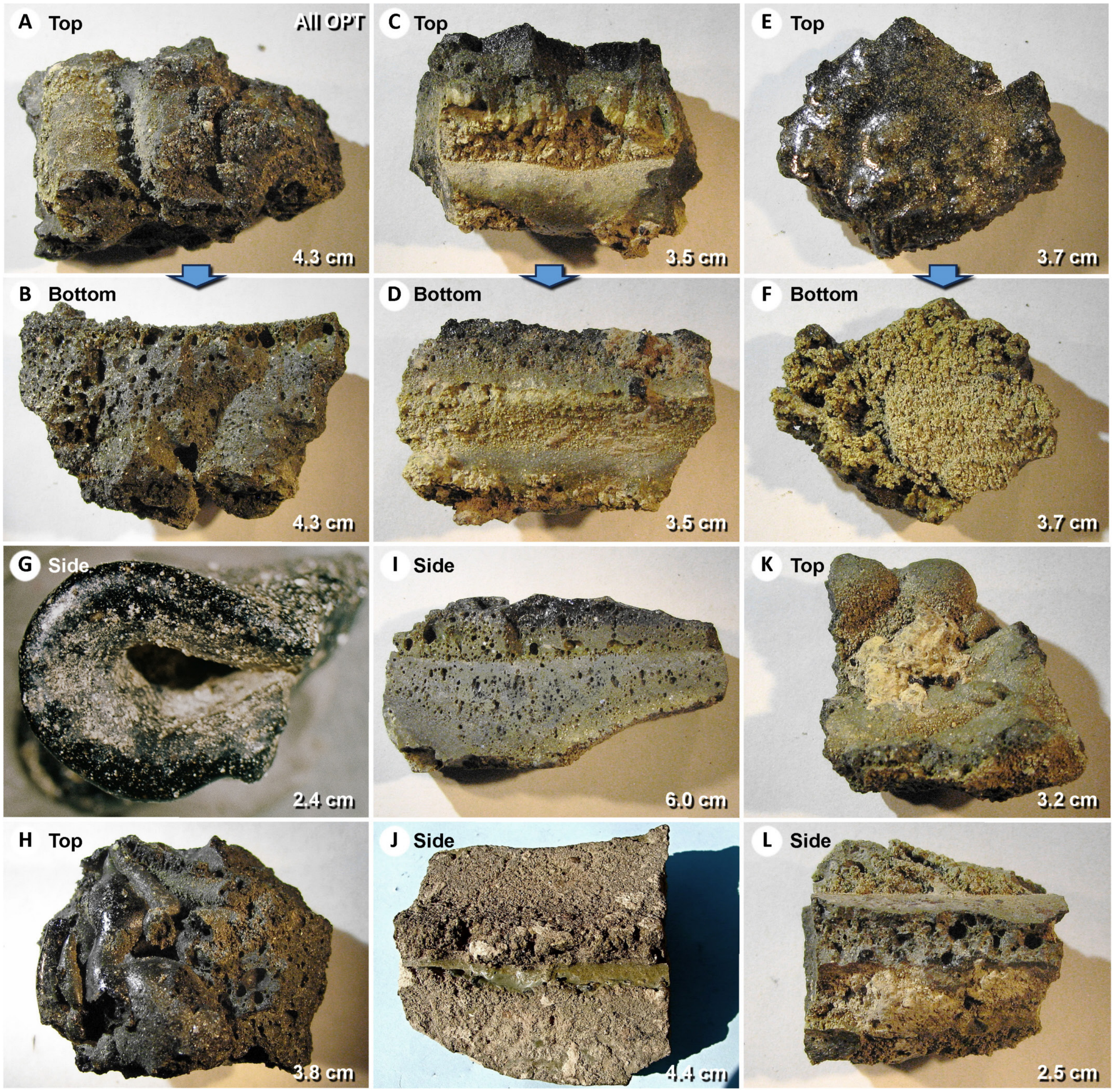

Figure 15: Meltglass fragments from the Pond deposit. All optical photomicrographs. **(A-B) (C-D) (E-F)** These pairs of images are of the inferred tops and bottoms of meltglass fragments. Note that the top photos are typically either glazed and reflective, as in panel E, or display rolled textures, as in panels A and C, interpreted as having been melted by a thermal pulse or aerodynamically splashed across the top of the glass while molten. As in panel B, the bottom images are typically vesicular or display a granular texture consistent with partially melted sand grains. **(G)** This meltglass fragment displays a distinctive morphology consistent with being folded while molten. **(H)** A meltglass fragment with distinctive tubular textures across the top of the glass. **(I-L)** Vesicular meltglass fragments with a distinctive multi-phase layered morphology.

the Vee and Pond deposits were excavated by backhoe, older and younger carbon was mixed into the deposits, giving a wide range of dates.

The $^{40}Ar/^{39}Ar$ dating helped eliminate any association with older craters elsewhere and confirmed a young deposit age. The significant uncertainties are mainly due to the presence of only small amounts of radiogenic argon (<5%) and the relatively long (6-hour) neutron irradiation that was conducted to test for ages in the Ma range. Incomplete resetting during impact-related thermal degassing could have led to an overestimate of the age, especially for very young (<100 ka) ages. Temperatures >1000°C were most likely attained during the impact, but these conditions only persisted for a few seconds, perhaps leading to incomplete argon diffusion. Non-radiogenic

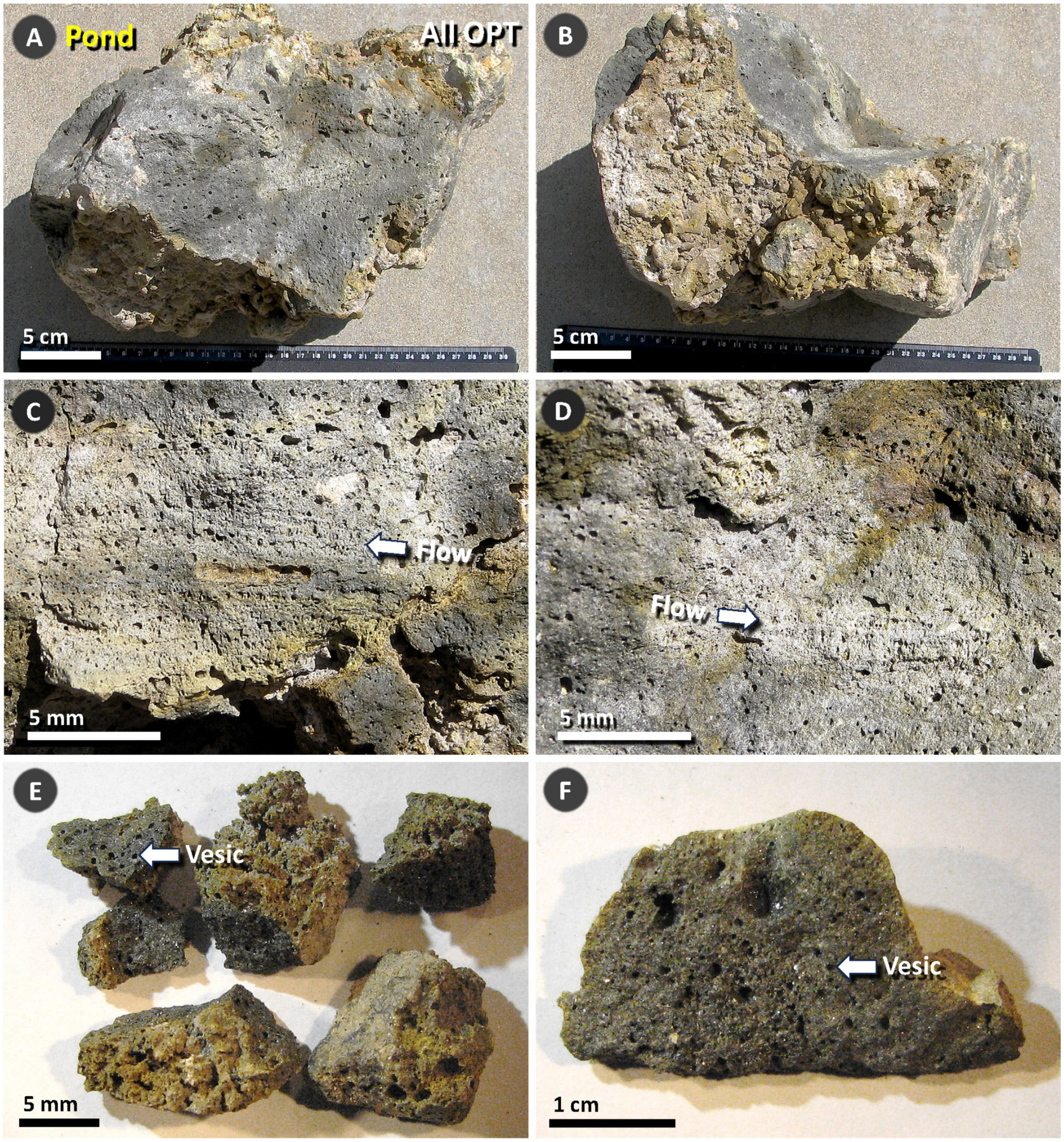

Figure 16: Optical photomicrographs of a 16-kg meltglass fragment. (A-B) This large fragment of meltglass from the Pond deposit is 31 long × 21 × 12 cm high and weighs 16.33 kg. Panel B shows partially melted sediment fused to the bottom. **(C-D)** Close-up photographs show layering, suggesting the meltglass flowed while molten (marked as "flow"). **(E-F)** Meltglass fragments broken from the larger object generally display a vesicular morphology ("vesic").

argon from air or other sources could also have been incorporated into the spherules as fluid inclusions or trapped on the surface of the spherules, leading to low radiogenic argon fractions (<5%). Shorter irradiation durations and additional chemical treatment planned for further work could provide better constraints on the formation age of these spherules.

The Vee and Pond glass median ages are slightly younger than for Trench #1, possibly due to contamination by microscopic modern plant roots that penetrated the glass and were impossible to remove during processing for radiocarbon dating. An alternate hypothesis is that three meltglass-forming impact events occurred one or more centuries apart, separated by only a few 100 m. However, this hypothesis is statistically unlikely. Alternatively, several lines of evidence suggest that the deposits in Trench #1, the Vee, and the Pond are the same age. First, the layer of spherules, meltglass, and shocked quartz in Trench #1 is stratigraphically below an Early Archaic projectile

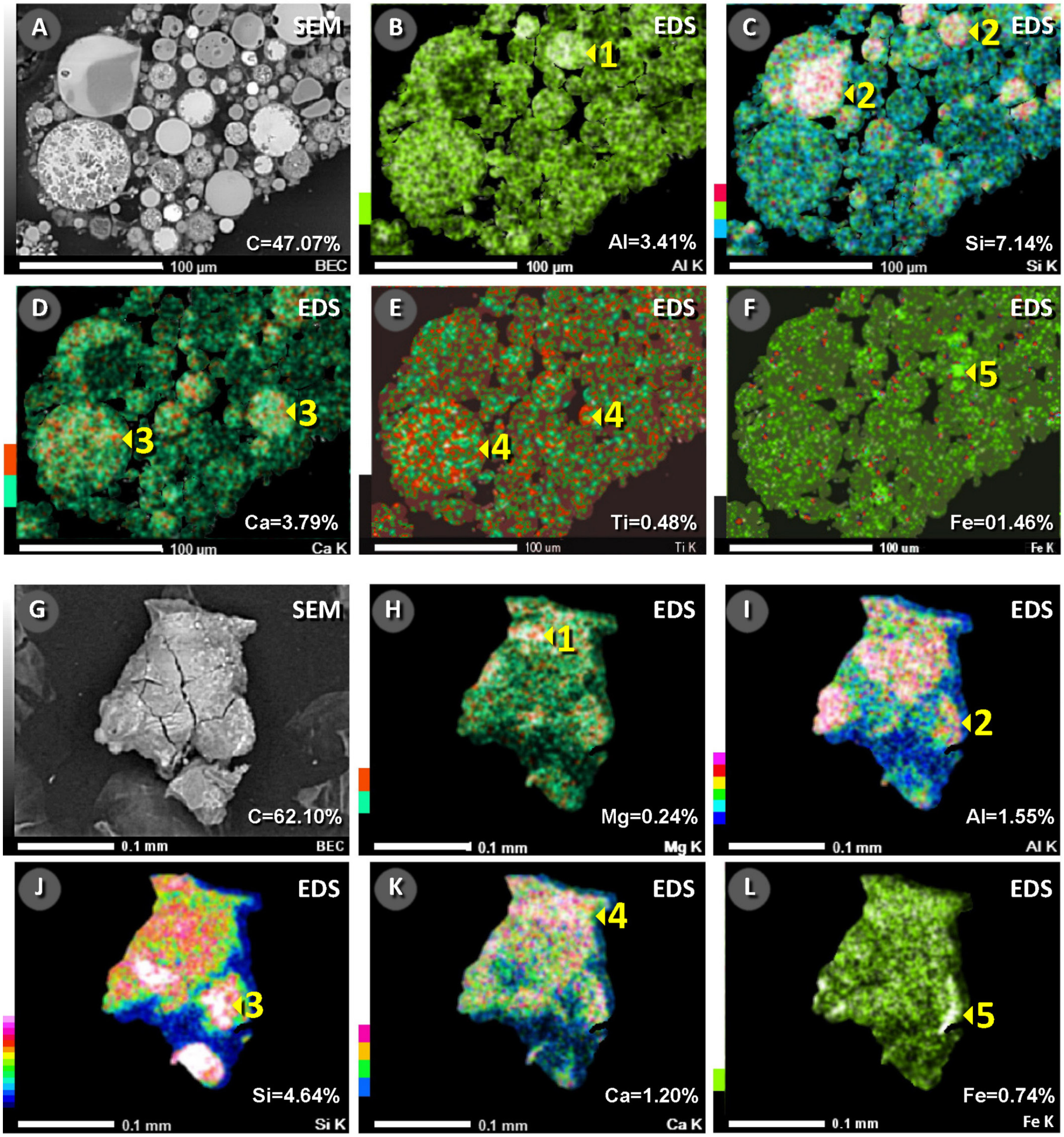

Figure 17: SEM-BSE and SEM-EDS elemental maps of Vee spherule clusters and meltglass. (A-F) A Vee spherules cluster shows a heterogeneous enrichment in Al, Si, Ca, Ti, and Fe. Numbered arrows point to selected areas of higher enrichment (brighter colors) in each panel. **(G-L)** Meltglass fragment from pit 3, showing heterogeneous enrichments in Mg, Al, Si, Ca, and Fe. The background behind the spherule clusters and meltglass fragments has been masked to black for enhanced clarity. The original, unmodified figures are in **Supporting Information, Figures S3–S8** [5].

point (age range: ~10,000-8,000 cal BP), thus indicating deposition of the material occurred before that (Figure 4, **Supporting Information, Tables S1 and S3** [5]). Second, in Trench #1, spherules, meltglass, and shocked quartz grains were associated with sedimentary carbon with a modeled age of 12,794 ± 69 cal BP, consistent with the age range of the YDB impact event from 12,835-12,735 cal BP (Figure 4, **Supporting Information, Tables S1 and S2** [5]). Third, five radiocarbon dates on the carbon-rich meltglass from the Vee and Pond deposits range from ~10,000

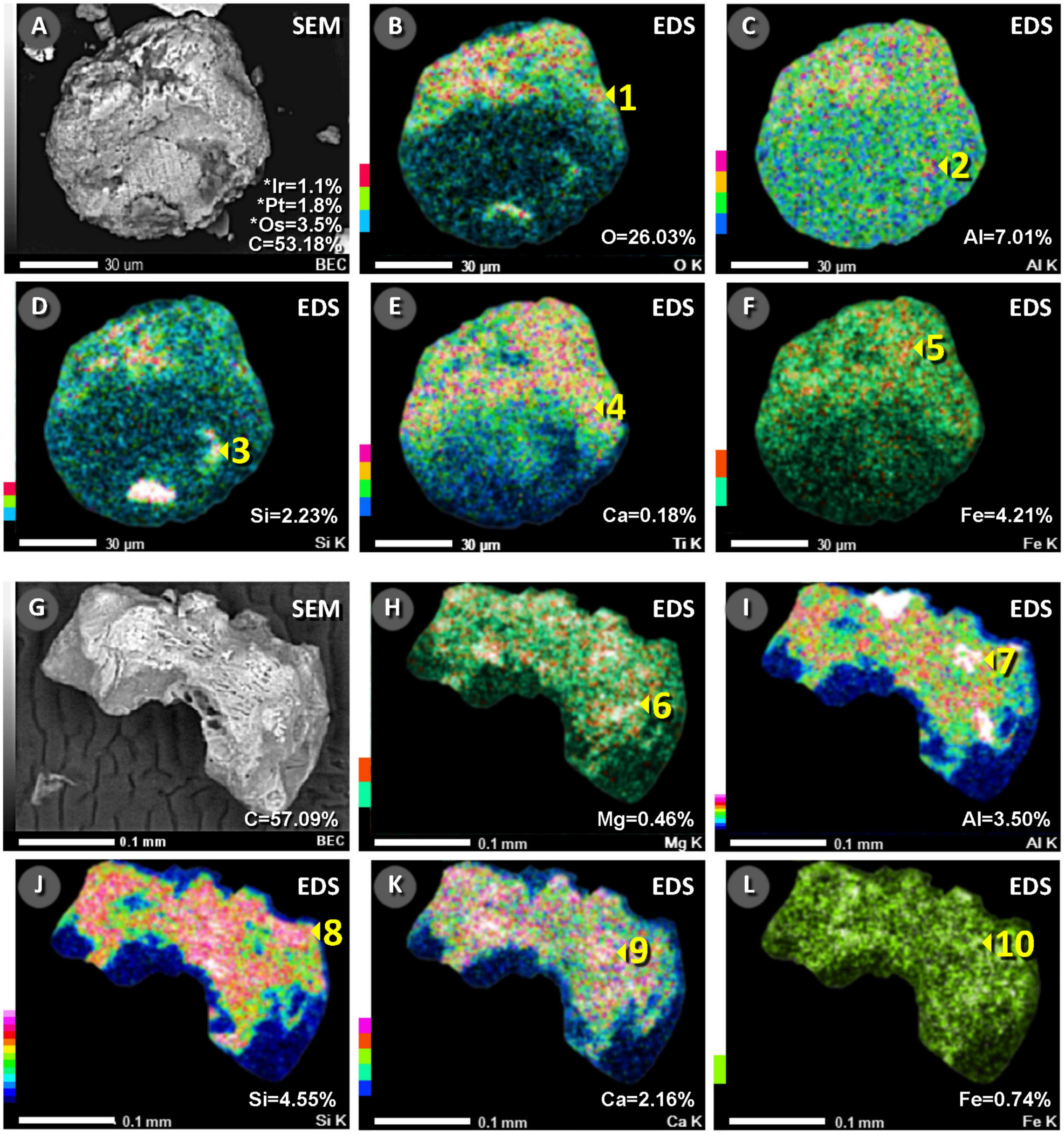

Figure 18: SEM-BSE and SEM-EDS elemental maps of meltglass and spherule clusters from pit 3. (A-F) The meltglass fragment from pit 3 shows heterogeneous enrichments (brighter colors) in Al, Si, Ca, and Fe. Numbered arrows point to selected areas of higher enrichment in each panel. **(G-L)** Another meltglass fragment from pit 3 shows heterogeneous enrichments in Mg, Al, Si, Ca, and Fe. For greater clarity, the backgrounds are shown as black. The original, unmodified figures are in **Supporting Information, Figures S9–S14** [5].

to 20,000 cal BP, and one sample of carbon spherules dated to ~29,000 cal BP (Figure 5, **Supporting Information, Tables S1 and S3** [5]), suggesting that this material was deposited between ~30,000 and 10,000 cal BP. Two of the five ages also overlap with the age of the deposits in Trench #1 and the age range of the YDB impact event at 99% CI. This result suggests that the impact occurred at ~12,800 cal BP, but more research is needed to confirm the inferred age of the event.

Although the dating on the deposits is uncertain, the spherules, meltglass, and shocked quartz grains in the well-dated Trench #1 are morphologically and geochemically similar to those in the Vee and Pond deposits, suggesting that all were deposited at the same time.

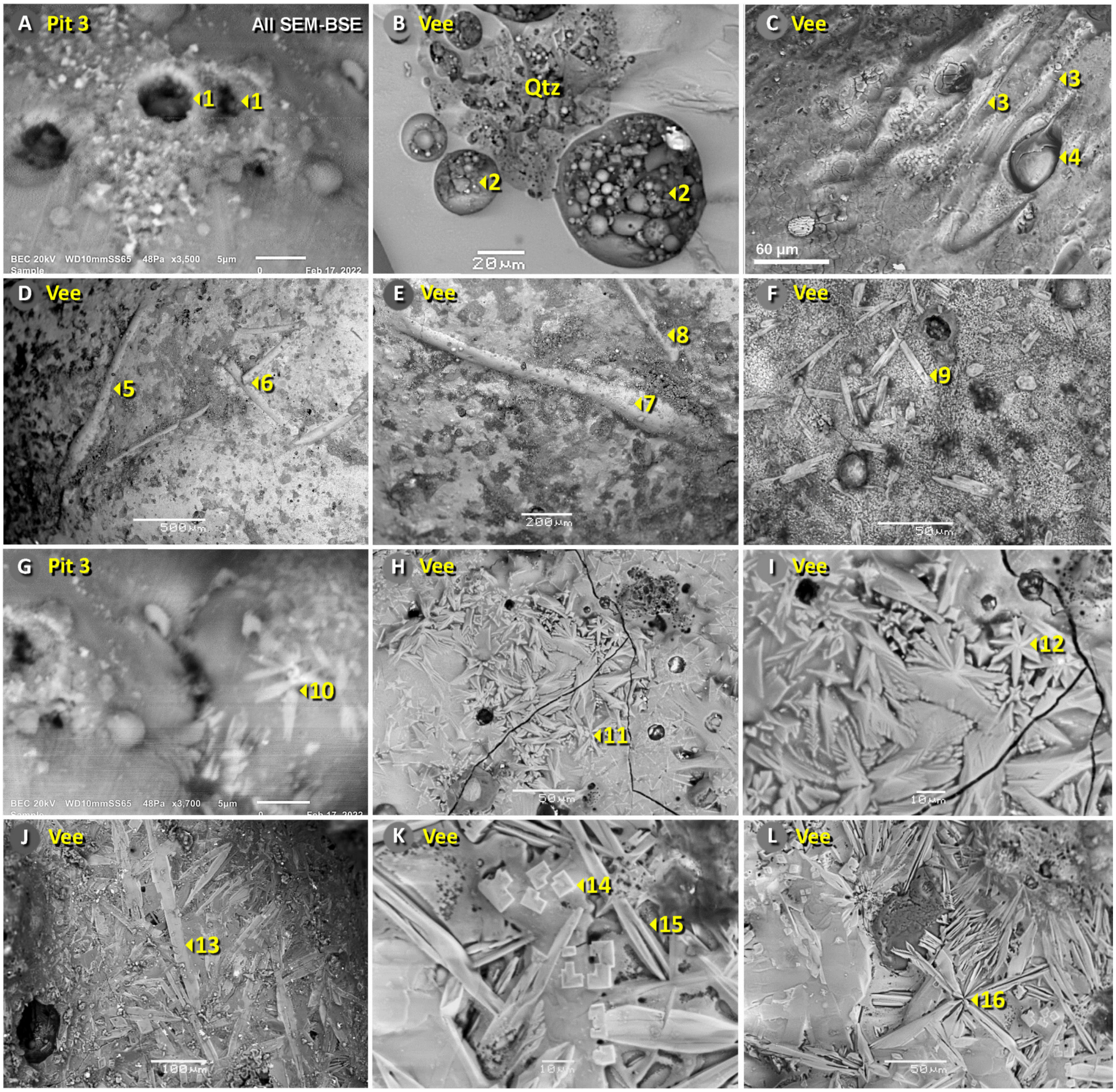

Figure 19: **SEM-BSE images of quench crystals and other surface features of meltglass. (A)** #1: Vesicles in meltglass due to high-temperature outgassing. **(B)** #2: Vesicles filled with spherules surrounding a quartz grain that melted at >1710°C (Qtz). **(C)** #3: Flow marks indicating the meltglass was moving while molten. #4: Small spherule inside a crater, indicating a secondary impact while meltglass was molten. **(D-E)** The numbers mark melt drapings across the meltglass. **(F-L)** The numbers indicate quench crystals, typically clinopyroxene, that crystallized on the meltglass as it cooled below ~1300°C. Panels A and G are from pit 3; all others are from the Vee deposit.

11. Origin of the spherules, meltglass, and shocked quartz

11.1 Anthropogenesis

Iron furnaces and other industries often smelted or refined materials that would yield slag, a waste product of smelting metal ores. This process separates molten rock from the desired metal (e.g., during steel production and iron ore smelting). However, there are no known historical industries near Perkins, Louisiana; the closest facilities are not in Louisiana but in states like Pennsylvania, Ohio, and West Virginia.

Smelting or glass manufacturing can produce slag glass, a distinctive type of pressed, layered material used in producing glassware and other items in the 19th century. However, there is no historical record of such industries near Perkins, Louisiana.

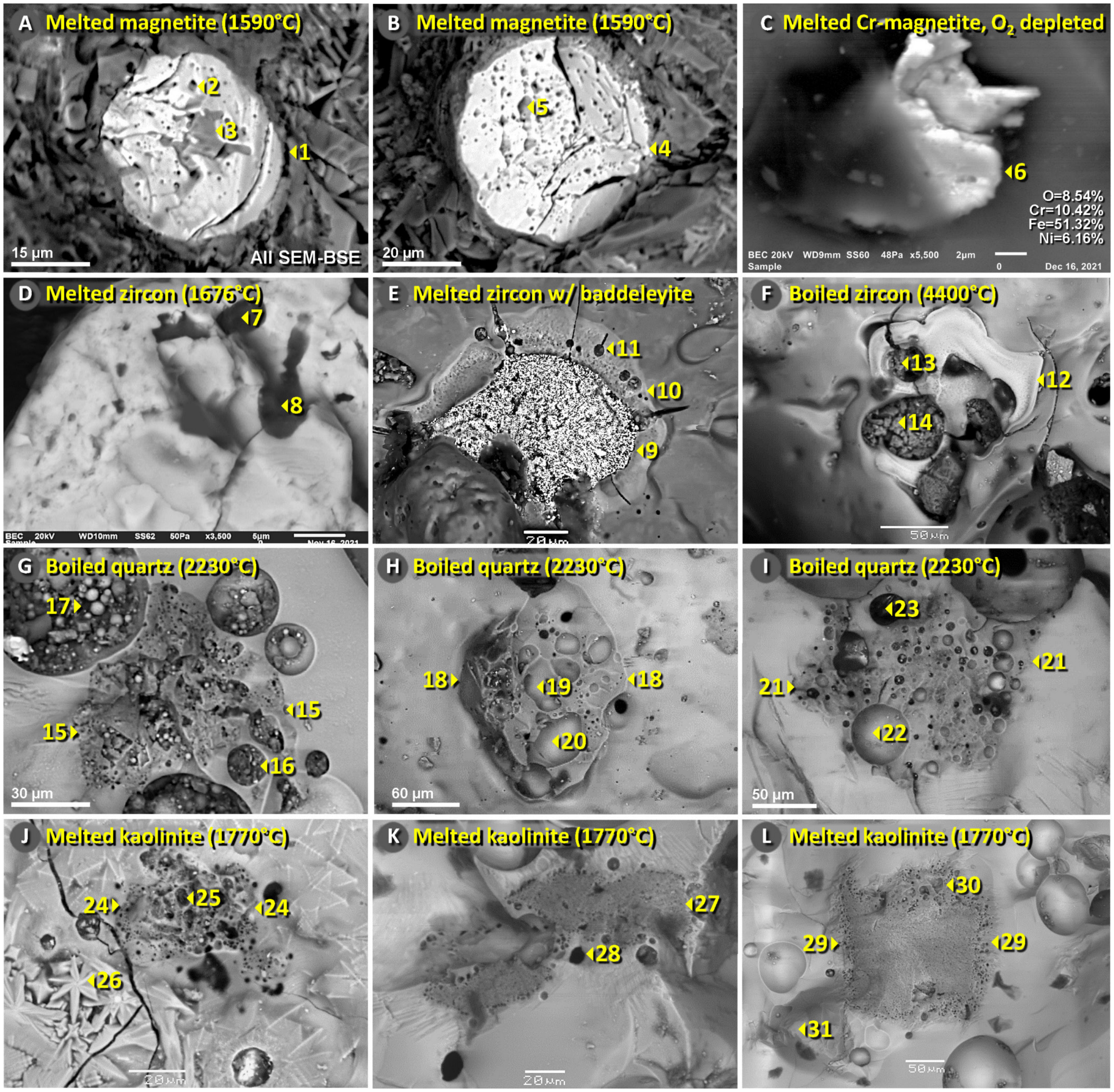

Figure 20: **SEM-BSE images of high-temperature melted minerals embedded in Vee meltglass. (A)** #1: Magnetite spherule, embedded in meltglass and melted at ≥1590°C. #2: Vesicles indicative of temperatures above the melting point of magnetite (~1590°C). #3: Melted quartz grain embedded in the magnetite, indicative of temperatures above the melting point of quartz (~1710°C). **(B)** #4: Melted magnetite spherule. #5: Vesicles indicative of temperatures above the melting point of iron. **(C)** #6: Melted NiCr-magnetite grain containing Cr, Fe, and Ni. **(D)** Zircon grains melted at ~1775°C. #7, #8: Vesicles indicative of high-temperature dissociation of the zircon. **(E)** #9: Zircon grain fully converted to baddeleyite at >1775°C. #10: The molten zircon began to diffuse into the aluminosilicate glass matrix. #11: Vesicles in diffused zircon due to the evolution of oxygen during dissociation of the zircon. **(F)** #12: Entirely melted zircon grain, showing flow marks. #13, #14: Vesicles in melted zircon due to the evolution of oxygen during dissociation **(G)** #15: Edges of quartz grain were fully melted above the melting point of quartz. #16: Vesicles in melted quartz due to the evolution of gases during boiling. #17: Numerous small spherules inside the large vesicle. The grain melted at ~1775°C and likely boiled at ~4400°C. **(H)** #18: Edges of quartz grain, possibly boiled at greater than 2200°C. #19, #20: Vesicles in melted quartz due to the evolution of gases during boiling. **(I)** #21: Edges of quartz grain, possibly boiled at greater than 2200°C. #22, #23: Vesicles in melted quartz due to the evolution of gases during boiling. **(J)** #24: Edges of kaolinite fragment melted at ~1770°C. #25: Vesicles due to the evolution of gases during melting. #26: Star-like Al-Si quench crystals in meltglass. **(K)** #27: Edge of melted kaolinite fragment. #28: Vesicles are caused by the evolution of gases during melting. **(L)** #29: Edges of melted kaolinite fragment. #30: Vesicles due to the evolution of gases during melting. #31: Flow marks indicative of the fusion of kaolinite into meltglass matrix. All examples are from the Vee deposit, except for panel D, which came from pit 3. The melting points of key minerals observed at Perkins are shown in Table 1.

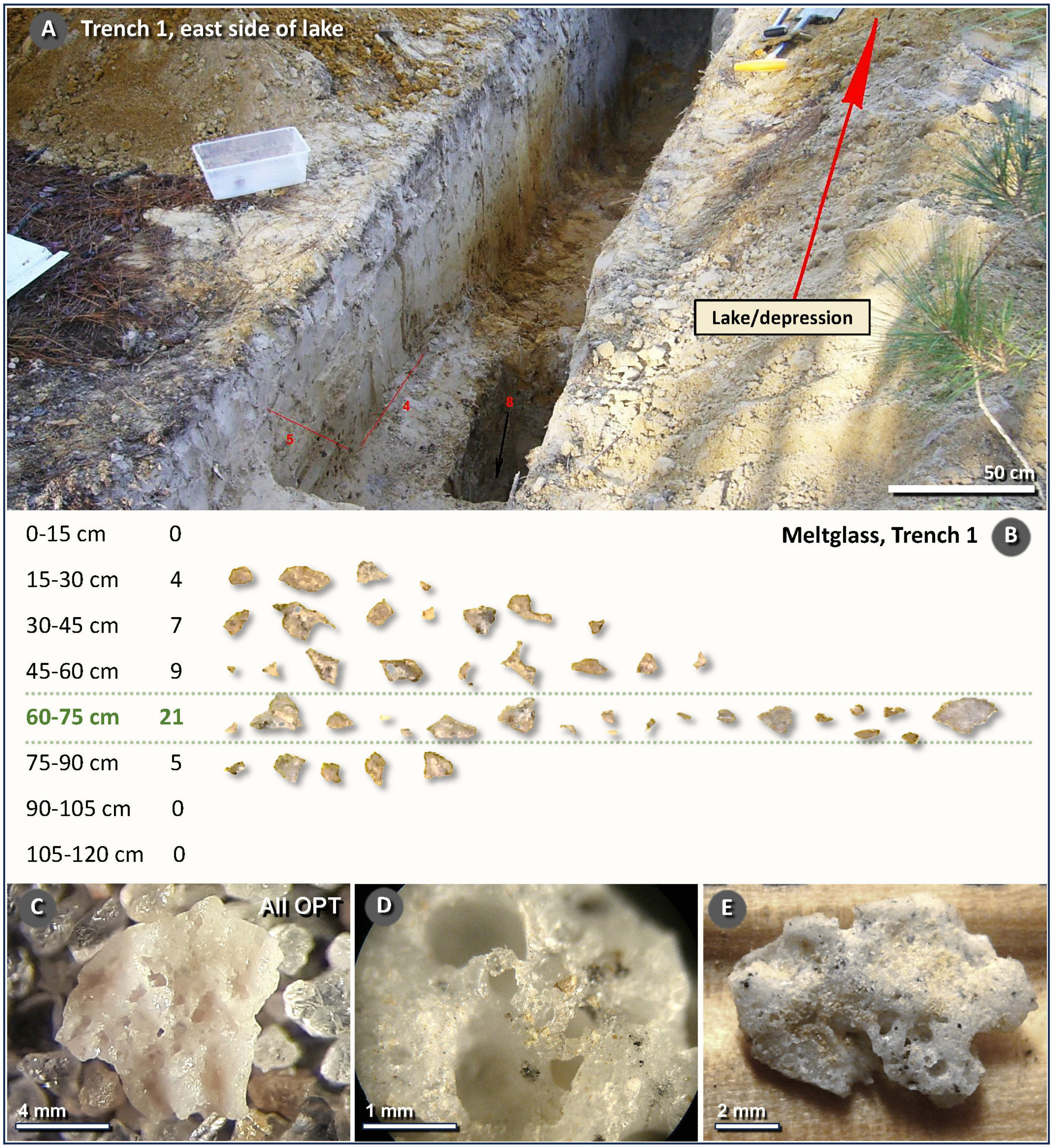

Figure 21: **Optical photomicrographs and graph of meltglass from Trench #1. (A)** The trench facing west. **(B)** Plot from Trench #1 showing photomicrographs and the number of fragments of meltglass by depth. Peak abundance occurred at 60-75 cm. **(C-E)** Photomicrographs of vesicular high-Si meltglass. These are low-resolution photographs of meltglass, mainly to show heterogeneous shapes. The background has been removed to assist in visualization. These are inferred not to be lightning-generated fulgurites because they are not ubiquitous in the sediment and do not have the characteristic tubular shapes common for fulgurites.

The area has historical remnants of an old sawmill, a sugar mill, a tongue paper mill, and oil prospecting and sulfur mining. However, none of these historical industries could have produced glass slag.

Lastly, we considered that the material might be fly ash from coal-fired power plants or railroad slag. The current landowners maintain that the previous owners dug up the deposits and did not haul in fly ash or other industrial material. Even so, we explored this contamination as a possibility. To do so, we compared the elemental abundances of Perkins spherules and meltglass to 273 fly ash samples from 31 studies representing 38 sites in Australia/New Zealand,

Table 1: Melting points of key minerals observed at Perkins.

Mineral	Formula	~Equilib Melt T (°C)	Est. Flux Melt T (°C)	~Equilib Boil T (°C)
Aluminosilicate glass	$CaAl2Si2O_8$	1300	1150	
Chert	SiO_2	1710	1520	2200
Chromite	$(Fe)Cr_2O_4$	2265	2065	2640
Clinopyroxene	$(Ca,Mg,Fe,Na)(Mg,Fe,Al)(Si,Al)_2O_6)$	1150	1000	
Hematite	Fe_2O_3	1538	1338	--
Ilmenite	$FeTiO_3$	1050	850	--
Iron sulfide	FeS, Fe_2S, Fe_3S	1200	1000	--
Kaolinite	$Al2Si2O_5(OH)_4$	1770	1500	
Magnetite	Fe_3O_4	1590	1390	2620
Native iron	Fe	1420	1220	--
Native Silicon	Si	1414	1214	--
Nickel iron	NiFe	1430	1230	--
NiCr-magnetite	$(Ni,Cr)Fe_2O_4$	1590	1390	
Quartz	SiO_2	1710	1520	2200
Titano-magnetite	$Fe^{2+}(Fe^{3+},Ti)_2O_4$	1625	1425	--
Wollastonite	$CaSiO_3$	1540	1340	--
Zircon	$ZrSiO_4$	1775	1575	4400

Asia, Europe, Africa/Mideast, and North America (Figiure 31A, **Supporting Information, Tables S8, and S9** [5]). We also compared the Si-rich Perkins melted material to Si-rich anthropogenic spherules [53]. The fly ash samples generally contain less Cr, Ni, Mn, S, Ti, Ca, Na, Mg, Fe, and Si than the Perkins samples. The Si-rich anthropogenic spherules generally contain less CaO, Al_2O_3, FeO, TiO_2, and MgO than the Perkins material (Figure 31B, **Supporting Information, Table S7** [5]).

Thus, the Perkins glass-and-spherule deposits are chemically unlike any investigated fly ash and anthropogenic spherule samples. Furthermore, the meltglass and spherules are buried up to ~6.5 m below the surface, making anthropogenic contamination highly unlikely. Furthermore, anthropogenesis from industrial activities is doubtful because all seven radiocarbon dates are older than 10,000 years, ranging from ~10,000 to 30,000 cal BP. In addition, the deposits are geochemically nearly identical to the average of Perkins sediment samples, suggesting the deposits derive from local sediment. Although anthropogenic sources (e.g., power plants, factories, and railroads) are capable of producing spherules and meltglass, they cannot generate temperatures required to melt or boil quartz, zircon, and kaolinite (~1710° to 4400°C), nor are they capable of generating the pressures needed to produce shocked quartz.

11.2 Railroads and logging operations

In the early 20th century, large parts of Louisiana underwent extensive logging activities, facilitated by installing temporary railroad tracks, which sometimes included industrial slag (i.e., meltglass) along the railway tracks. Although some of the trackways are still visible at the Perkins site, there is no evidence of any remaining slag alongside them. In addition, there is no known mechanism by which railway activities could boil zircon grains, boil quartz grains, or produce shocked quartz, all of which have been found embedded within meltglass at Perkins.

11.3 Natural gas blowout

Local residents speculated that the lake/depression resulted from a natural gas blowout, which sometimes occurs among the oil fields of Louisiana. While this possibility might explain the crater, a blowout could not have generated the high pressures/temperatures required to produce the spherules, meltglass, shocked quartz, and other proxies.

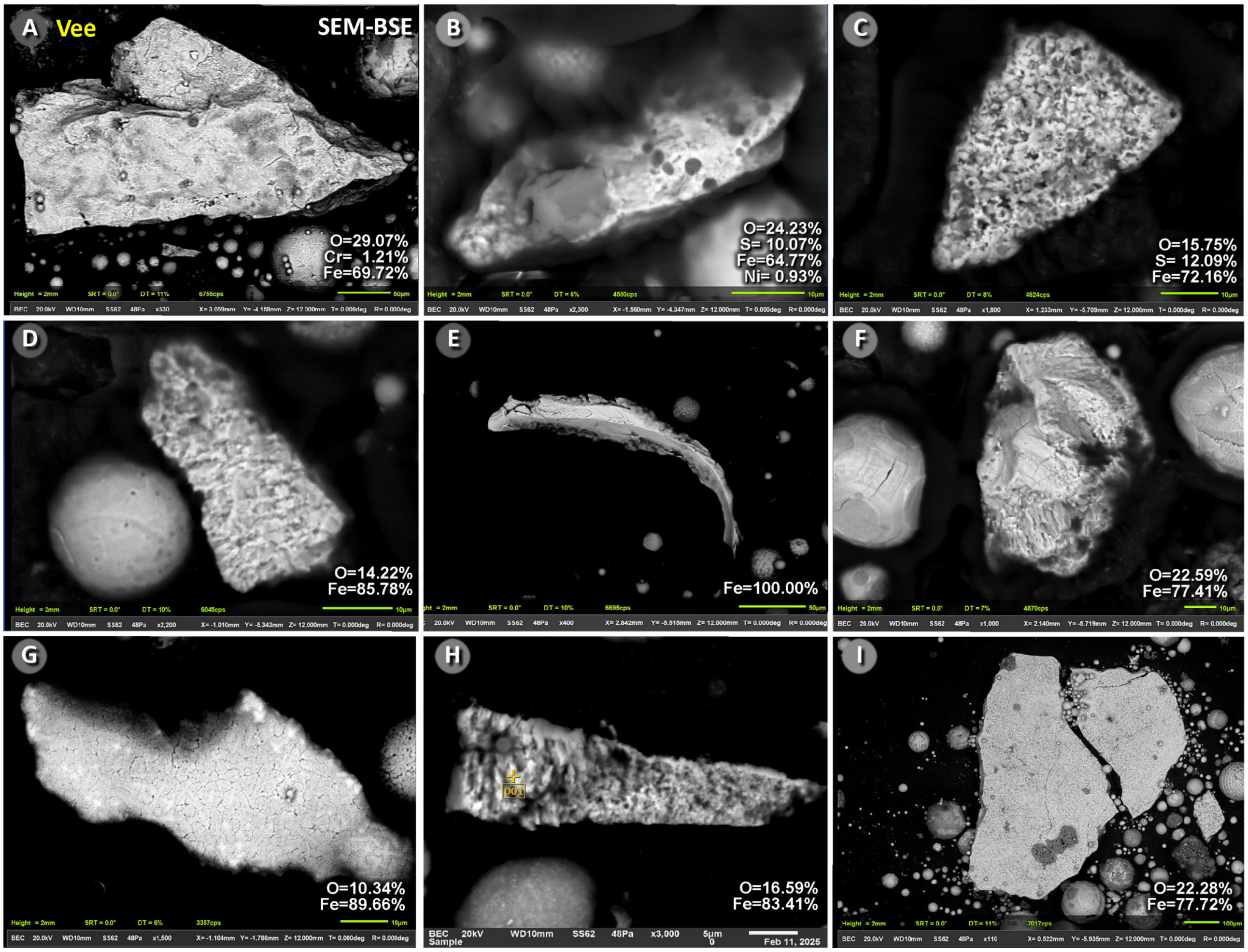

Figure 22: Low-oxygen metallic flakes from the Vee deposit. (A) A flake-like particle of chromian magnetite. **(B)** Ni-Fe-S rich grain, most likely a mix of ~30 wt% troilite and ~70 wt% Ni-rich magnetite. **(C)** Fe-S rich grain, most likely a blend of ~30 wt% troilite and ~70 wt% wüstite. **(D)-(I)** Various Fe-rich flake-like grains depleted in oxygen from typical iron oxide. Panel E is native iron, rarely found on Earth's surface. Panels F and I have the composition of wüstite, which is also rarely found on Earth but is common in extraterrestrial material.

Table 2: Comparison of different types of microstructures in quartz.

Characteristics	PDFs	PFs	nPFs	DLs
Microstructures	Lamellae	Open fractures	Glass-filled fractures	Dislocations
Features crystallographically controlled	Yes	Yes	No	Sometimes
Planar fractures/lamellae	Planar	Virtually planar	Subplanar	Subplanar
Parallel fractures/lamellae	Parallel	Virtually parallel	Subparallel	Subparallel
Thickness of fractures/lamellae	Usually ≤1 μm	Usually ≥3 μm	nm to μms	Usually ≥2 μm
Features filled with amorphous silica	Yes	Sometimes	Often	Never
Spacing between fractures/lamellae	Usually <1 μm	Usually >20 μm	nm to μms	Usually ≥5 μm
Estimated formation pressure (Gpa)	~10-25	<10	≥1.5	<1

11.4 Authigenesis

There are various types of silica, including authigenic ones. Kletetschka et al. [1] studied shock-fractured quartz at Tunguska and reported that the quartz grains often showed isotropic silica coatings and glass-filled fractures similar to those found at the Perkins site. Their analyses confirmed that

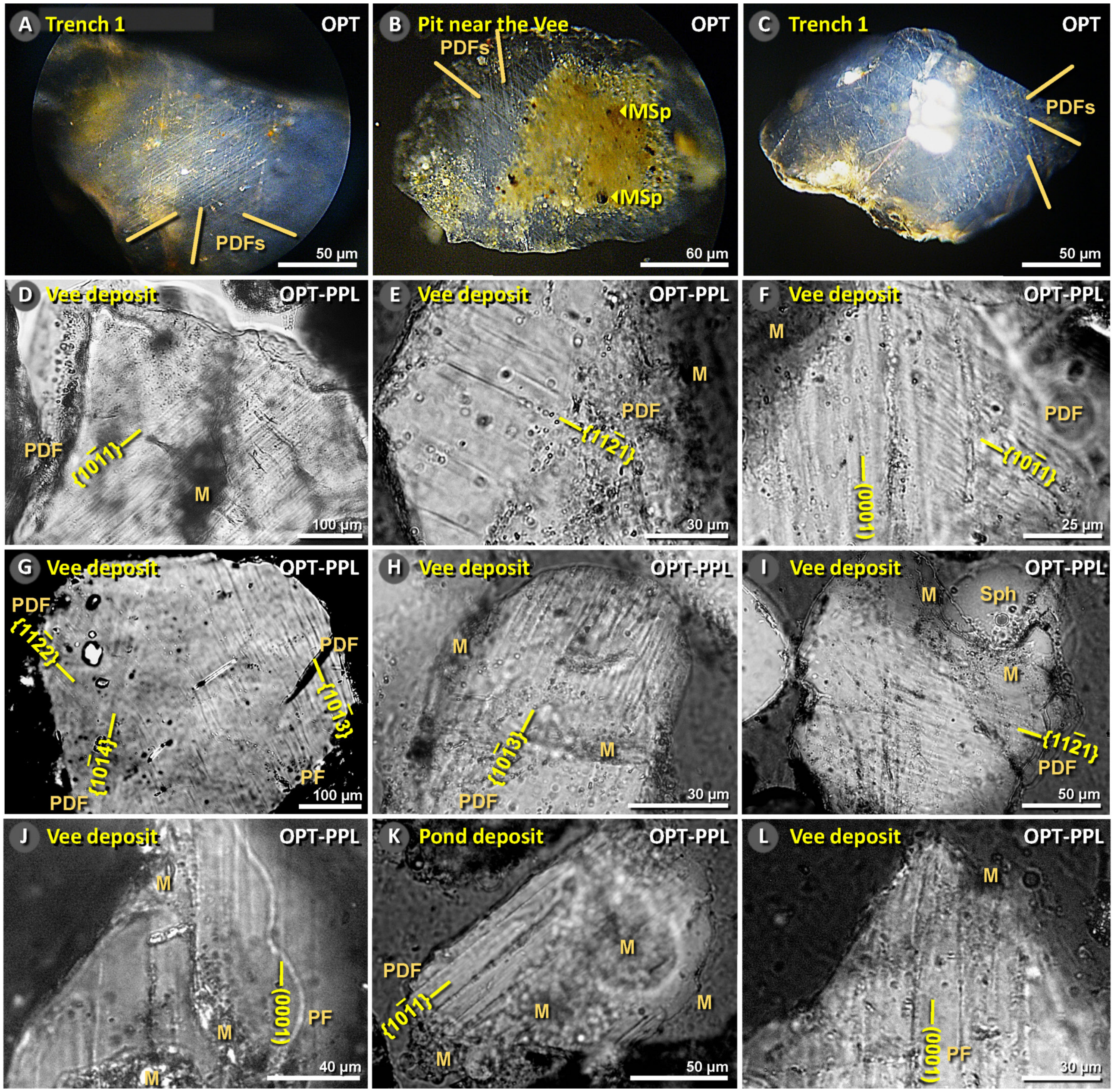

Figure 23: Shocked quartz grains from various locations. Planar deformation features (PDFs) and planar fractures (PFs) are marked. Yellow lines indicate 1-4 sets of lamellae. "M" marks areas of isotropic melted silica, as determined by crossed polars; "MSp" indicates microspherules; "PDF" marks planar deformation features; and "PF" indicates planar fractures. Panels A and C are from Trench #1 on the east side of the lake; panel B is from a well at the south end of the lake; the others are from the Vee deposit, except for panel K from the Pond deposit. **(A-C)** Optical photomicrographs. Notably, shocked quartz grains typically have a bluish hue from light diffracting through the shock lamellae. Panel B shows a shocked quartz grain displaying hundreds of small spherules (MSp) fused to its surface, confirming a close relationship between the shocked quartz and the spherule deposits. Shocked quartz grains were also extracted from fragments of meltglass. The largest spherule is ~6 µm in diameter and, therefore, is difficult to visualize in the image. **(D-L)** Grayscale optical plane-polarized (OPT-PPL) photomicrographs. The Miller-Bravais crystallographic indices shown were measured with a universal stage. Panel I shows a ~90-µm-diameter spherule embedded in the meltglass fragment surrounded by a border of meltglass. The spherule appears to have collided with the meltglass and destroyed the shock lamellae in that part of the grain.

these features were melted silica rather than cryptocrystalline or microcrystalline quartz. As was previously reported for Tunguska, we often measured oxygen/silicon ratios of 53/47 wt% or less in partially melted grains, significantly lower than quartz overgrowth and quartz cement (i.e., hydrated silica at ~66/34 wt%), thus eliminating authigenesis. In addition, no known authigenic process can produce shocked quartz.

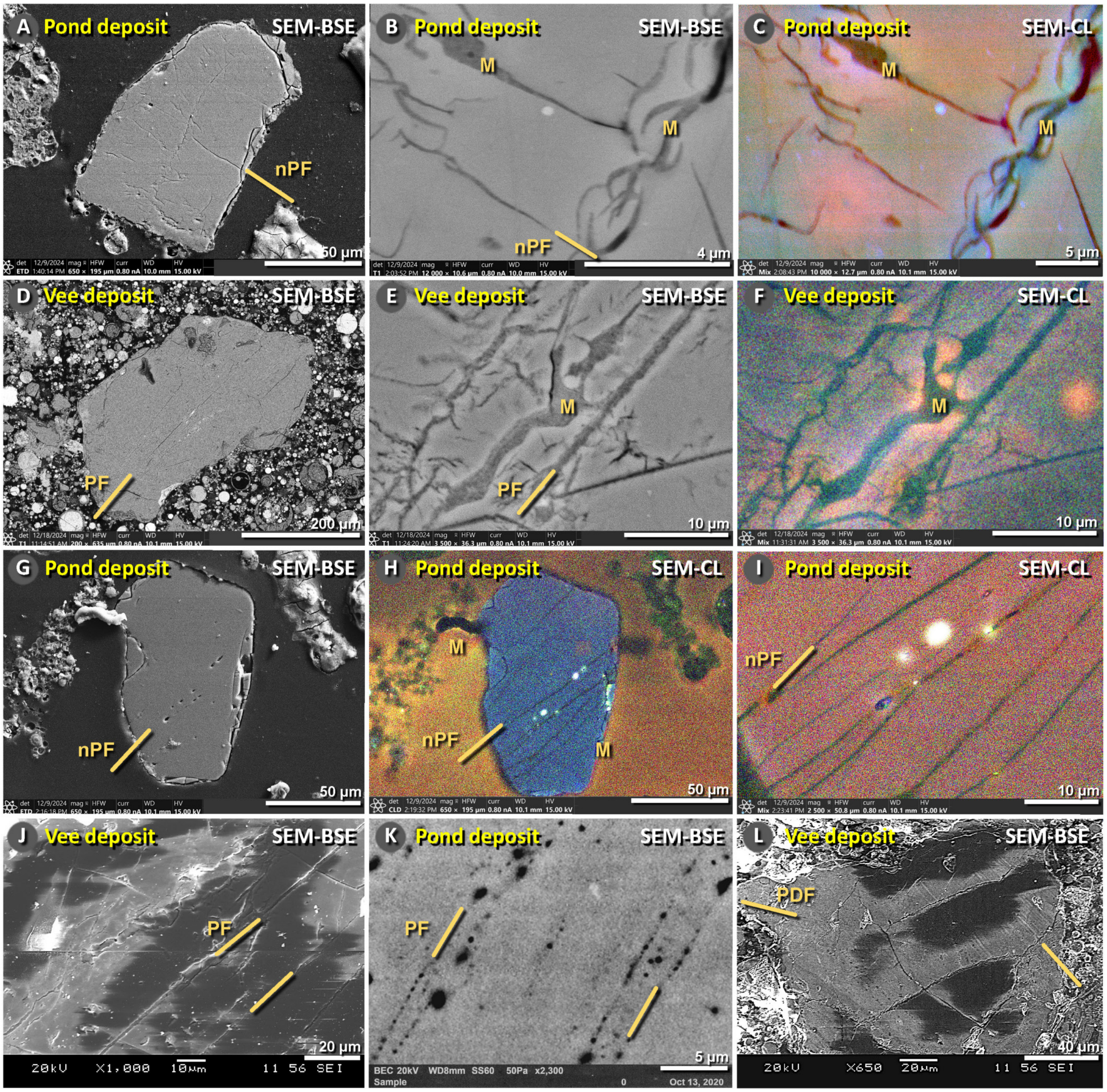

Figure 24: Features of shocked quartz grains from the Vee and Pond deposits. Planar deformation features (PDF) and planar fractures (PF) are marked. Glass-filled non-planar fractures (nPF) are also marked. Yellow lines indicate one and occasionally two sets of lamellae. "M" marks areas of isotropic melted silica, as determined by crossed polars. **(A)** Shocked quartz grain with glass-filled nPFs from the Pond deposit. **(B-C)** SEM-BSE and SEM-CL images of the grain in panel A. The darker areas are filled with melted silica (M). **(D)** Quartz grain with glass-filled PFs from the Vee deposit. **(E-F)** SEM-BSE and SEM-CL images of the same grain as panel D. The darker areas are filled with melted silica (M). **(G)** Shocked quartz grain with glass-filled nPFs from the Vee deposit. **(H-I)** SEM-CL images of the same grain as panel G. The darker areas are filled with melted silica (M). **(J-L)** SEM-BSE images of quartz grains from the Vee and Pond deposits, displaying PFs and PDFs.

11.5 Tectonism

Perkins is in a relatively inactive coastal fault zone, and although fault motion can create breccia, meltglass, deformation lamellae, and macro-scale melting [54, 55], tectonic processes cannot boil quartz and zircon or produce PDFs, glass-coated quartz, or silica-filled fractures in individual quartz grains [35, 56]. Anders et al. [57] noted that deformation lamellae are not fractures but dislocations. Unlike the shock features observed at Perkins, they are never glass-filled and are never shocked.

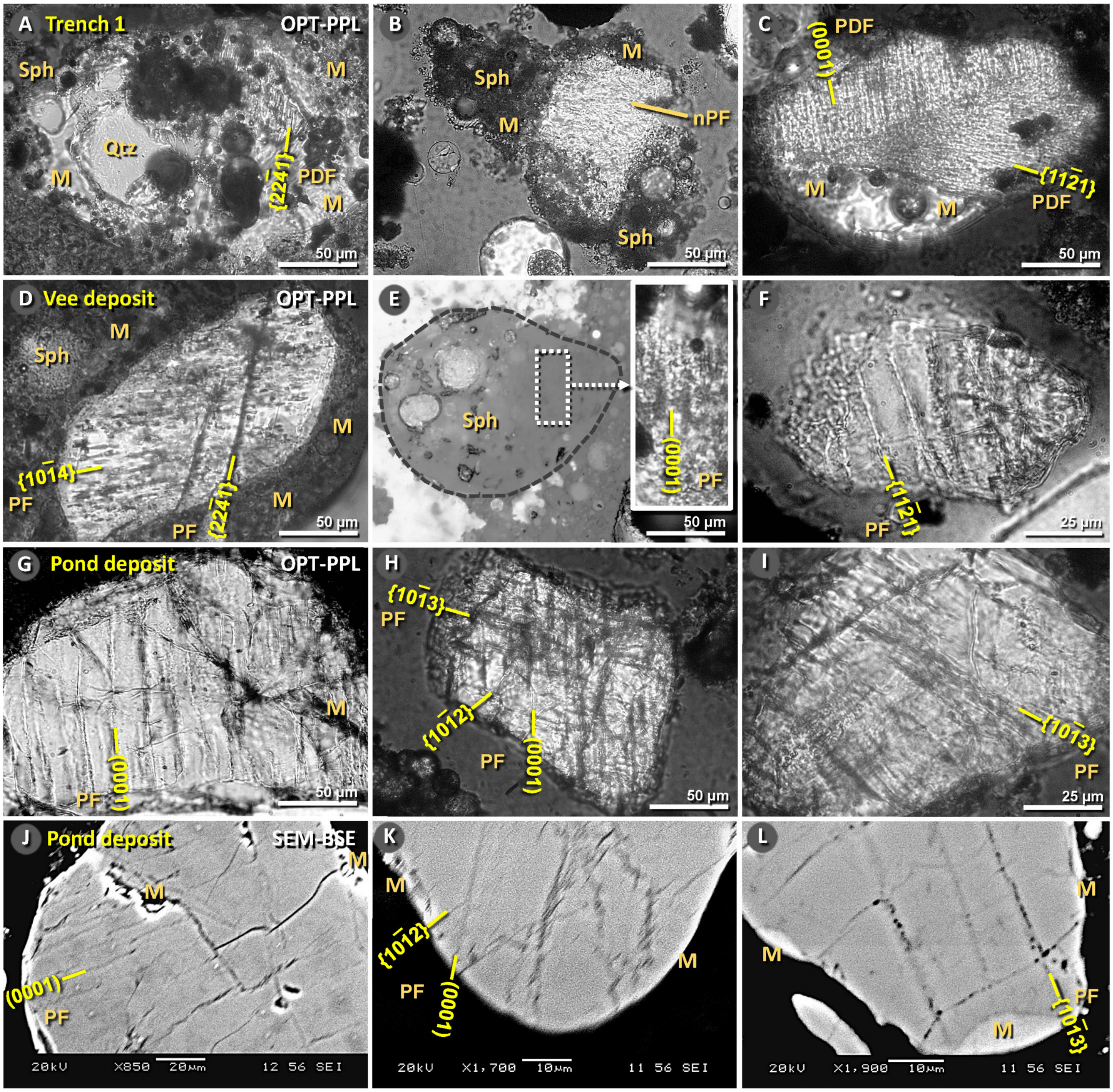

Figure 25: Thermally warped, glass-filled shocked quartz grains from Trench #1, the Vee, and the Pond. Optical plane-polarized photomicrographs (OPT-PPL) and SEM-BSE images of thermally altered shocked quartz grains from the three deposits. Lower shock pressures produce grains with less clearly defined lamellae; all contain melted silica along the fractures. "M" marks areas of isotropic melted silica, as determined by crossed polars; "Qtz" marks areas of crystalline quartz; "Sph" indicates spherules; "PDF" marks planar deformation features; "PF" shows planar fractures, and "nPF" indicates glass-filled non-planar shock fractures. Miller-Bravais crystallographic indices were measured using a universal stage, except for nPFs that could not be indexed because they were too thermally altered. Panels A-C are from Trench #1, D-F are from the Vee deposit, and G-L are from the Pond deposit. **(A)** A fragment of meltglass containing unshocked crystalline quartz (left) and shocked quartz (upper right). **(B)** A shocked quartz grain embedded in a cluster of meltglass and spherules. **(C)** A polycrystalline shocked quartz grain with meltglass fused to the bottom edge. **(D)** A thermally distorted shocked quartz grain surrounded by meltglass containing spherules. **(E)** Oval-shaped glassy spherule embedded with a shocked quartz grain displaying glass-filled planar fractures (inset). **(F-I)** OPT-PPL images of thermally warped shocked quartz grains displaying PDFs and PFs. **(J-L)** SEM-BSE images of corresponding grains in each panel above. All three have lighter-colored Ca-Al-Si meltglass (M) fused to the edges of the grains.

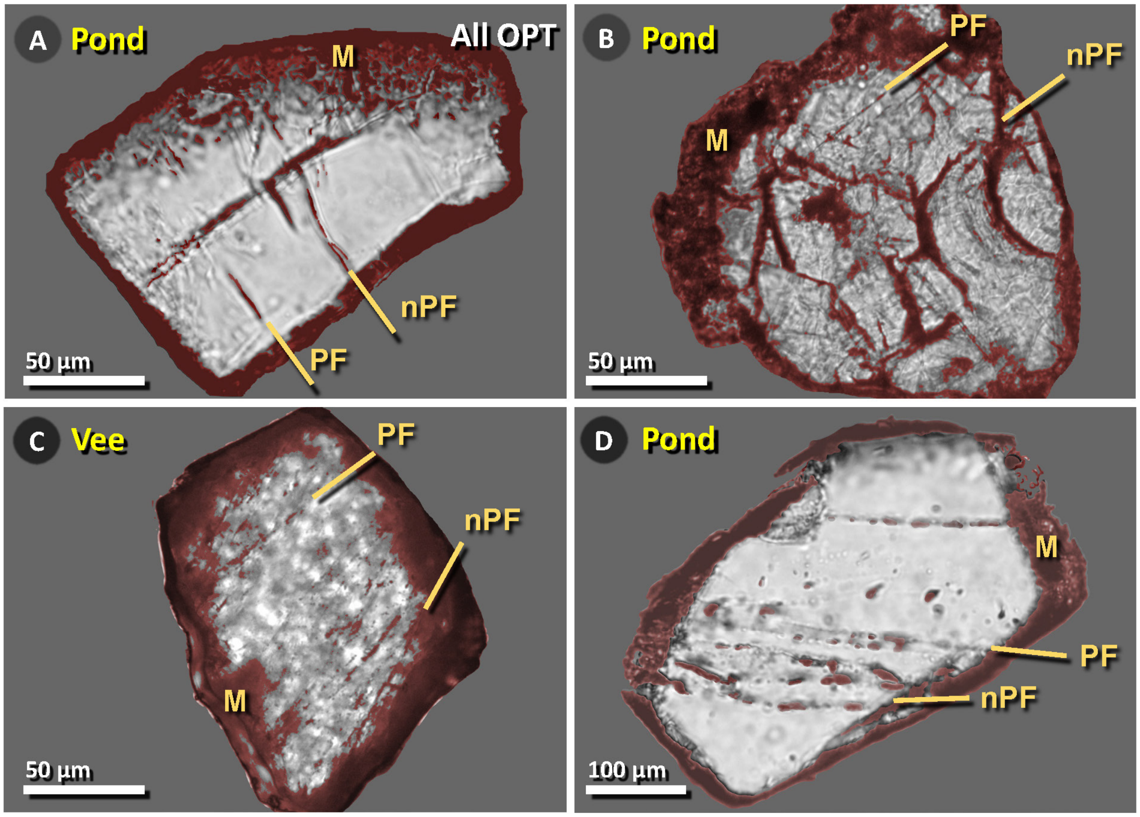

Figure 26: **Optical images of meltglass-coated, glass-filled quartz grains from the Vee and Pond. (A-D)** Portions of quartz grains that are isotropic under crossed polars are marked in false-colored red ("M") and were subsequently identified as melted quartz using CL. Gray areas are crystalline quartz. Glass-filled planar fractures (PF) and non-planar fractures (nPF) are marked. The amorphous areas were false-colored red, and the non-grain backgrounds were false-colored gray to enhance clarity. The original, unmodified figures are in **Supporting Information, Figure S15** [5].

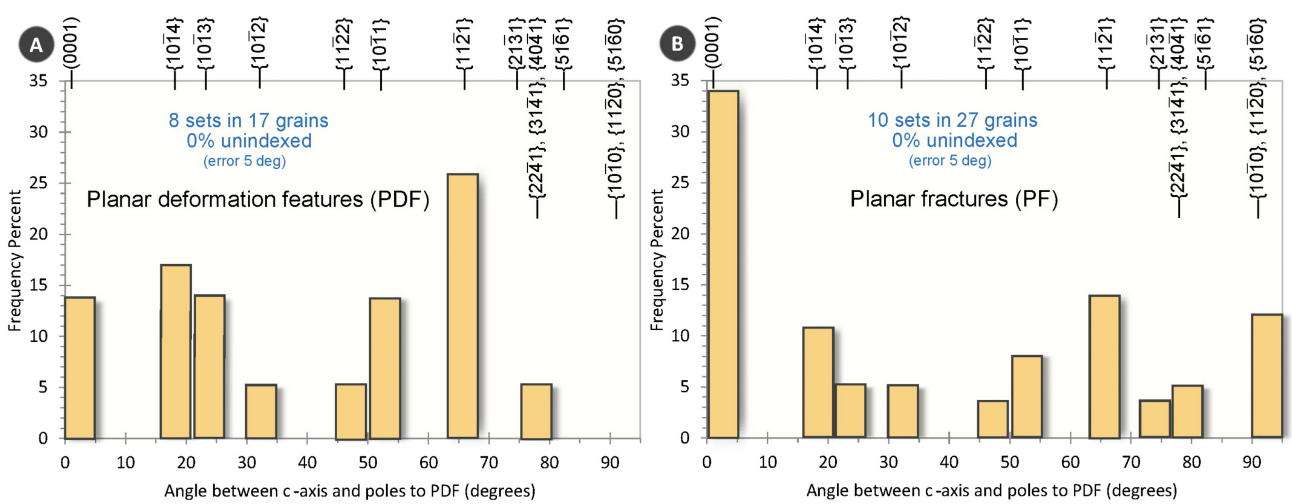

Figure 27: **Miller-Bravais indices.** The percentages of 44 shocked quartz grains for each index, as measured using the universal stage. **(A)** 17 grains displayed eight indexed sets of planar deformation features (PDFs). **(B)** 27 grains displayed 10 indexed sets of planar fractures (PFs). As is typical of PFs at other sites, the (0001) plane, an indicator of low shock conditions, is one of the most common at Perkins [33]. Shocked quartz abundances (44 grains) are high at Perkins, with 1% showing evidence of shock metamorphism (~1 per 100 quartz grains).

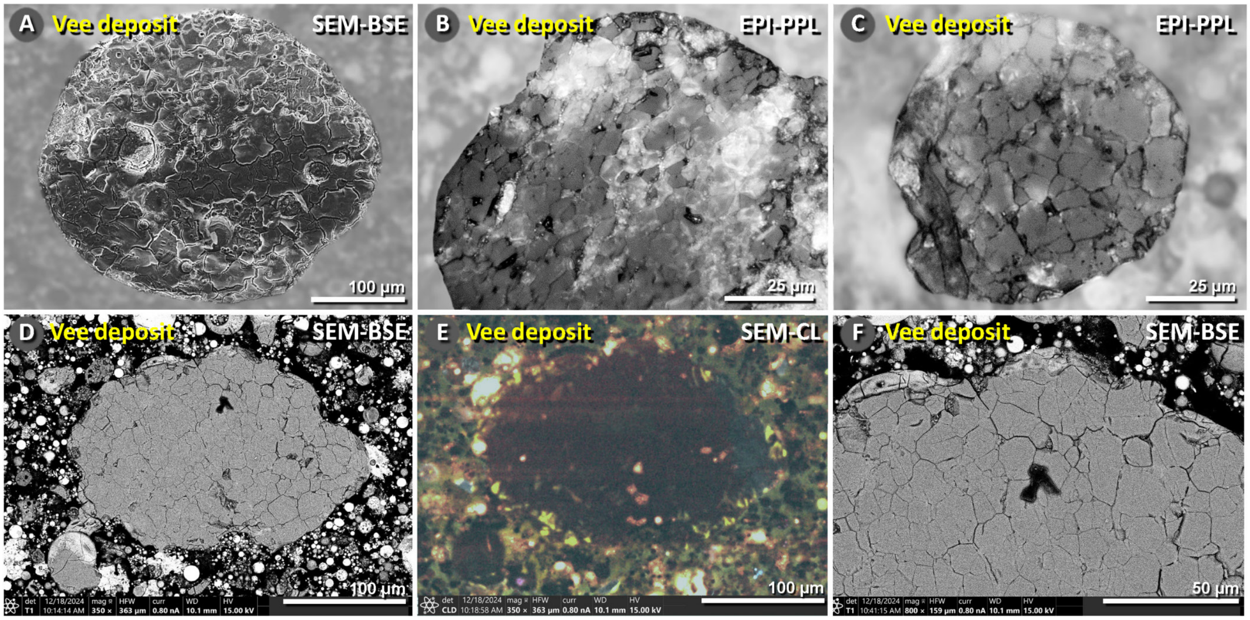

Figure 28: **Microbrecciated quartz grains from the Vee. (A-F)** SEM-BSE, EPI-PPL, and SEM-CL images of incipient microbrecciated grains. Panel E is an SEM-CL image showing that the glass-filled microbrecciated grain in panel D is non-luminescent (black) and, therefore, amorphous. The non-grain backgrounds in panels A-C were blurred and lightened to enhance clarity. The original, unmodified figures are in **Supporting Information, Figure S16** [5].

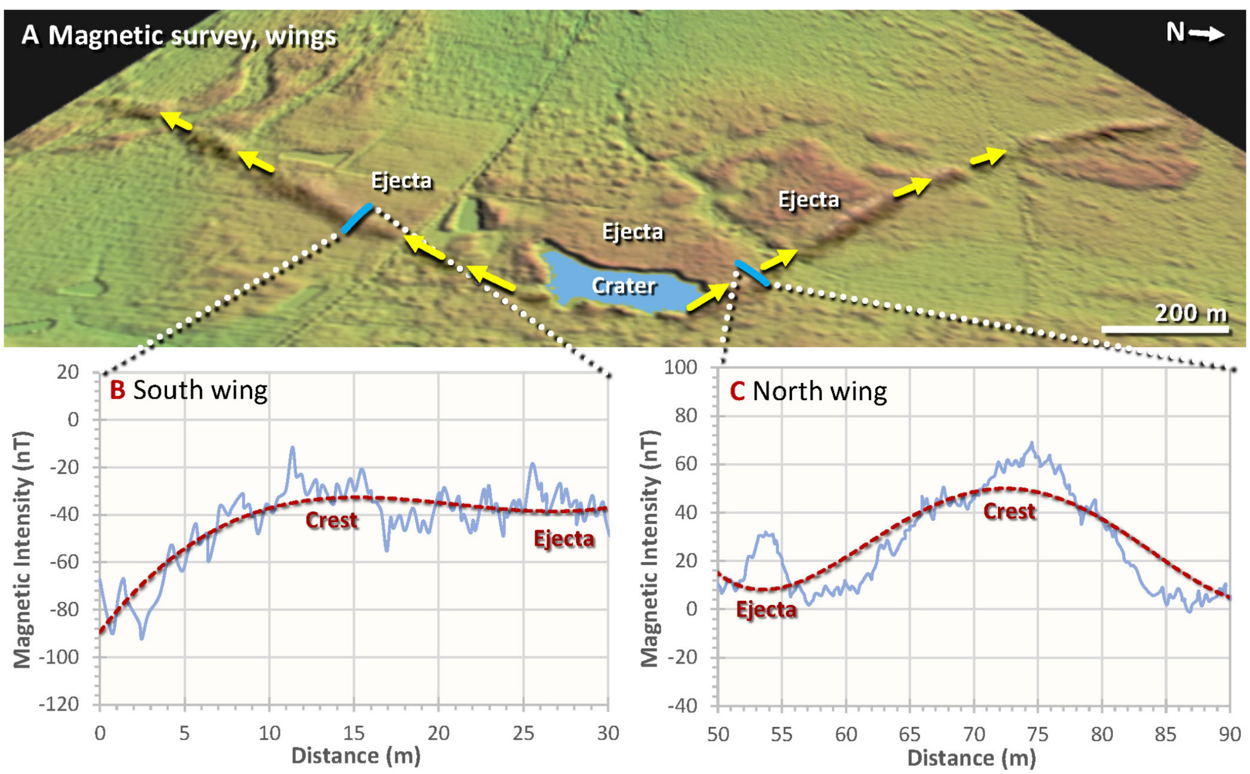

Figure 29: **Magnetic surveys across the lake/depression's wings. (A)** The LiDAR digital elevation model shows two large wing-like features (yellow arrows) extending away from the lake/depression. These Fe-rich raised features may have resulted from impact material being ejected from the airburst/impact, similar to rays of secondary ejecta on the Moon and Mars [51]. **(B-C)** Raw magnetic profiles across the two wings are shown as solid blue lines with smoothed results as red dashed lines. The profiles show peaks in magnetic intensity (nT) that correspond to the physical tops of the wings ("crests"). Other increases correspond to the potential ejected material west of the lake/depression (ejecta). The vertical scale is exaggerated several times, and the wings have been digitally highlighted for clarity. The base figure was created with Global Mapper, v. 8.0.

Table 3: Lists the proxy type, analytical method, and key finding for the above results.

Proxy Type	Analysis Method	Key Finding
Dating	Radiocarbon Dating (OxCal Modeling); Argon-argon dating	Spherule/meltglass layer dated to 12,794 ± 69 cal BP; overlaps Younger Dryas Boundary. Argon-argon dating confirms the age is young and not from a much older impact event.
Spherules, Fe- and Si-rich	Optical Microscopy; SEM; EDS; LA-ICP-MS	>100 tonnes; complex morphologies; Fe-, Si-, Al-, Ca-rich; peak inside lake depression.
Carbon Spherules/ Glasslike Carbon	SEM; EDS; LA-ICP-MS	High carbon content; PGE enrichment (Os, Ir, Pt); indicators of extraterrestrial material.
Meltglass	Optical Microscopy; SEM; EDS; LA-ICP-MS; INAA	>1 tonne; highly vesicular; melt temps ≥1590–4400°C; aluminosilicate glass compositions.
Metallic Flakes (Low-Oxygen)	SEM; EDS	Native Fe, troilite, wüstite flakes; extraterrestrial chemistry; melt textures.
High-Temperature Minerals	SEM; EDS; Optical Microscopy	Quartz, zircon, and kaolinite melted/boiled; temperatures far exceed terrestrial processes.
Shocked Quartz, Glass-filled fractured Quartz	Optical Microscopy; SEM; Cathodoluminescence; Universal Stage	PDFs, PFs, and nPFs observed; ~1% of quartz grains shocked in the deposits, consistent with cosmic impact pressures (approx. >5 GPa).
Microbrecciated Quartz	SEM; Cathodoluminescence	Brecciated quartz grains with amorphous cement; high shock stress indicator.
Magnetic Anomalies	Ground Magnetic Surveys	Positive anomalies match the "wings" of depression and are consistent with ballistic ejecta patterns.

11.6 Volcanism

Spherules, meltglass, and breccia can form from volcanism. However, it is widely accepted that volcanism cannot produce shock metamorphism [35, 56]. Furthermore, the nearest volcanoes are >1000 km away in Central America, which is far too distant to deposit tonnes of material at the Perkins site.

11.7 Lightning

This process typically produces tubular fulgurites confined to small areas up to several meters in diameter [26, 58, 59], much smaller than the 300-m lake. One might reasonably expect lightning strikes to be frequent over time on any given part of the planet, and therefore, fulgurites should be ubiquitous. However, we found only one fulgurite in 32 cores and five trenches, and it was not associated with an abundance peak in spherules and meltglass. Furthermore, meltglass was not ubiquitous outside of the inferred impact layer. Although we searched extensively for meltglass fragments in Trench #1, we observed none in three samples, inconsistent with formation by lightning strikes, which are expected to be ubiquitous.

There is a potential connection between lightning and impacts. Lightning strikes are inferred to be numerous in impact-related dust clouds, based on observing massive increases in lightning in volcanic plumes. For example, after the submarine eruption of Hunga Tonga, the incidence of volcanic lightning was so high that it constituted up to 80% of all global lightning activity at that time [60]. However, lightning generated during an airburst differs significantly from typical thunderstorm or volcanic lightning in several key aspects. In airburst-generated lightning, charge separation primarily occurs through debris particles rather than water droplets or ice crystals in thunderstorms [61]. The dust/debris cloud produced by the airburst would have distinct electrical conductivity properties due to its unique composition, which includes vaporized impactor material and superheated atmospheric gases [62], combined with extreme temperatures exceeding several thousand Kelvin.

While lightning related to an impact event may have contributed to forming some features in our samples, the mechanism would have differed fundamentally from typical terrestrial lightning processes, potentially producing unique signatures in the geological record. Thus, regular lightning as a potential formation mechanism can be excluded.

11.8 Older airburst/impact event

We considered whether the Perkins deposits might be reworked from those older impact events. There are five known impact craters in the southeastern United States within 800 km of Perkins: a ~58-Ma crater 300 km away in Texas, a ~84-Ma crater ~700 km away in Alabama, and three ~100-300-Ma craters >800 km away in Tennessee. In addition, Chicxulub, the 65-Ma K-Pg crater, is >1000 kilometers away in Yucatán, Mexico, and the 35-Ma Chesapeake Bay crater is >1700 km away in Virginia. These craters are too distant to have ejected a 16.33 kg meltglass fragment that landed at the Perkins site. In addition, it is unlikely that spherule deposits hundreds of km away from a crater would have been concentrated at >100 billion spherules/kg at Perkins. Additionally, the $^{40}Ar/^{39}Ar$ data of the spherules constrain the age to <2 Ma, significantly younger than any known major impacts in the region. Thus, the most plausible scenario is that a local impact event deposited the material, most likely within the last 30,000-10,000 years.

EVIDENCE

- **Lake/Depression Morphology**
  - 300-meter-long shallow depression with a raised rim
  - Unusual steep-sided basin geometry
- **Material Findings**
  - 100 tonnes of Fe-, Si-, Ca-rich spherules
  - ~1 tonne of vesicular meltglass
  - Abundant shocked quartz with PDFs, PFs, nPFs
  - Oxygen-depleted metallic flakes (e.g., wüstite, native Fe)
  - Glasslike carbon fragments
- **Geochemical Data**
  - High-temperature minerals (e.g., melted zircon, quartz, magnetite)
  - PGEs (Os, Ir, Pt) enrichment in spherules
- **Radiometric Dating**
  - Radiocarbon dating centers on ~12,794 ± 69 cal BP
  - 40Ar/39Ar dating: Deposits are young (<2 Ma)
- **Hydrocode Modeling**
  - Impact modeling predicts formation of shallow depression via airburst
- **Magnetic Surveys**
  - Positive magnetic anomalies over "wings" adjacent to depression

INTERPRETATIONS

- **Formation Mechanism**
  - Airburst event created meltglass, spherules, shocked quartz
  - High-temperature processes (>1710–4400°C) involved
- **Origin of Materials**
  - Materials unlikely from anthropogenic sources (e.g., fly ash, slag)
  - Not volcanic, tectonic, or lightning-related
- **Depositional Context**
  - Likely from single event at Younger Dryas onset (~12,800 cal BP)
  - Spherule abundance and depth distribution support airburst
- **Crater Origin**
  - Lake/depression potentially first airburst crater in W. Hemisphere
  - Morphology and geophysical signatures consistent w/ known impacts

CONCLUSION

- **New Evidence for Younger Dryas Airburst**
  - Supports hypothesis of multiple cosmic impact events during YDB
- **Potential First Airburst Crater**
  - Perkins site represents a rare, preserved airburst-created feature
- **Scientific Implications**
  - Adds crucial understanding to airburst physics, geological impact signatures
  - Challenges assumptions that small airbursts cannot create craters
- **Future Research**
  - Additional dating, geochemistry, and modeling needed to confirm origin/age

Figure 30: **Visual Flowchart.** To aid in synthesizing this study's complex, multidisciplinary data, we provide a summary flowchart that directly links the key proxies, analytical methods, and findings to their broader interpretations. This schematic representation highlights the logical progression from field observations and laboratory analyses to rejecting conventional hypotheses and accepting a cosmic airburst as the most plausible explanation. By visually organizing the evidence and its implications, this framework underscores the robust, converging lines of support for a high-energy, mid-air cosmic event around 1650 BCE.

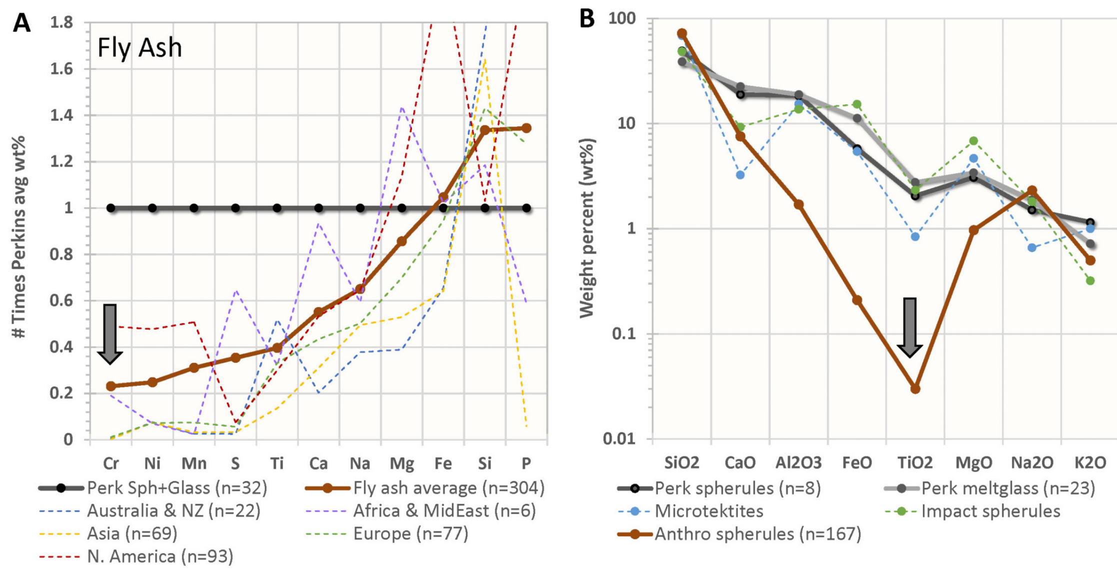

Figure 31: Comparison of Perkins meltglass and spherules to other materials. (A) Fly ash: selected elemental abundances for Perkins spherules and meltglass compared to normalized abundances of fly ash samples (**Supporting Information, Tables S8 and S9** [5]). The solid black line represents the Perkins melted material normalized to 1, where "n = 32" equals the number of samples compiled; the solid red line represents the average fly ash values from five continents (n = 304) normalized to Perkins values; and the dashed lines indicate individual values from five continents. The Perkins spherules are compositionally dissimilar to all fly ash tested on five continents. **(B)** Anthropogenic spherules, microtektites, and impact spherules compared to Perkins spherules and meltglass. The solid black line represents values for Perkins spherules (n = 8); the solid gray line denotes Perkins meltglass (n = 23); the solid red line indicates Si-rich anthropogenic spherules [53]; and the dashed lines represent microtektites and impact spherules [53]. The Perkins spherules are compositionally dissimilar to the anthropogenic spherules. However, they closely match the values for microtektites and impact spherules, consistent with an impact origin.

11.9 Airburst/impact event

A comparison of Perkins melted spherules and meltglass to impact-related microtektites and impact spherules reveals they are compositionally similar (Figure 31B). Thus, the presence of these materials, along with boiled quartz grains, boiled zircon, and shocked quartz, supports a high-temperature, high-pressure cosmic impact event at the Perkins site.

However, although these materials were found *in situ* in Trench #1, that was not the case for the Vee and Pond deposits, so the question remains regarding their original location. Before 1999, one pit was excavated at the Lake deposit site, displaying numerous fragments of meltglass and spherule-rich clusters (site "W" in Figures 7 and 8). We searched but found no other primary deposits away from the lake/depression. Therefore, the most likely source appears to be the Lake deposit site on the NW edge of the lake/depression (Figure 3). The glass-and-spherule deposits' lateral and vertical distribution patterns are consistent with the lake being ground zero for an airburst/impact, but this issue of their origin remains unclear.

To further explore the cosmic impact hypothesis, we performed neutron activation analyses (NAA) on the sediment from Trench #1 in search of elemental abundances indicative of potential extraterrestrial (ET) material. A useful test is to compare the ratios of Ni and Cr to Fe because Ni is typically enriched in ET material ~330 times over crustal abundance [63] and Cr is enriched 38 times [63], whereas Fe is enriched much less at only ~5 times [63]. The results reveal peaks in Ni/Fe and Cr/Fe ratios that are higher than crustal averages but lower than for meteoritic material (Figure 32A), consistent with the dominance of terrestrial material mixed with small amounts of ET material, typically reported at <2 wt% [64–66].

In addition, we calculated the same ratios from SEM-EDS elemental abundances for selected metal-rich areas of Vee meltglass fragments. Ni/Fe ratios in 5 of 10 spherules and 3 of 22 meltglass fragments were higher than the ET average ratios [63], while the others displayed terrestrial ratios [63]. The Cr/Fe ratios for 4 of 10 spherules and 3 of 22 meltglass fragments were higher than the ET average ratios (Figure 31B). Thus, these results suggest that terrestrial melted sediment became mixed with minor amounts of ET material.

We also used laser ablation inductively coupled plasma mass spectrometry (LA-ICP-MS) to measure elemental abundances for 7 Perkins spherules. We then compared these elemental abundances with those of known ET material, which is typically highly enriched compared with

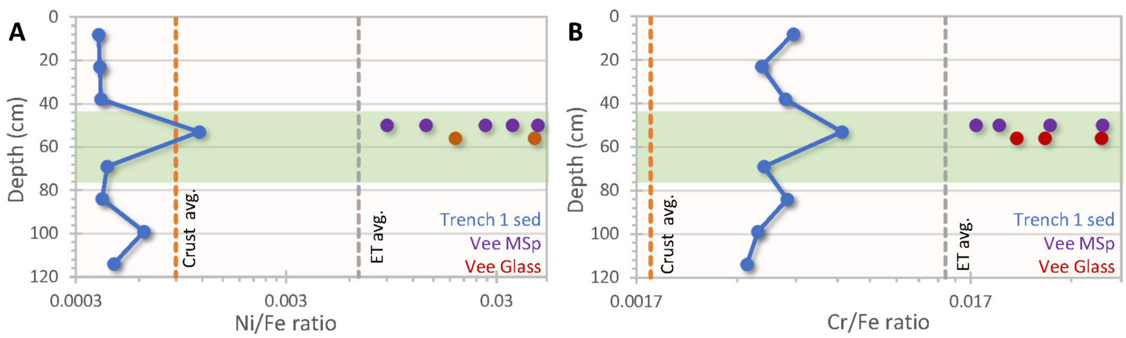

Figure 32: Nickel, chromium, and iron ratios. Trench #1 values are the solid blue lines plotted by depth in cm below the surface. Vee spherules are purple dots, and Vee meltglass values are red dots, plotted at the same depth as the ~12,800-year peak in spherules. **(A)** The Ni/Fe ratios by depth show an abundance peak at ~50 cm, overlapping the two largest peaks in deposits of meltglass and spherules. **(B)** The Cr/Fe ratios by depth also show an abundance peak at ~50 cm. For panels A and B, SEM-EDS measurements on selected examples of Vee spherules and deposit meltglass show enrichments in Ni and Cr that are larger than ET averages but within the range of known ET material.

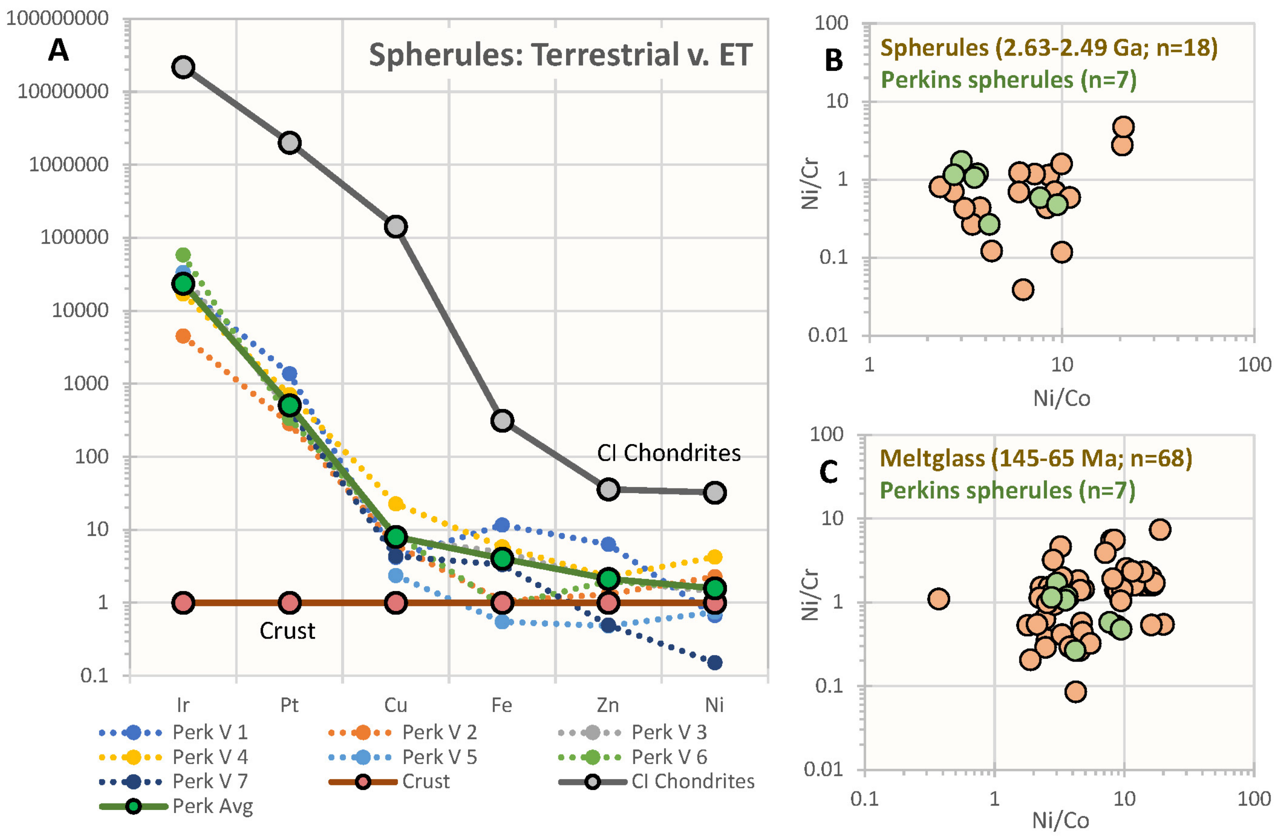

Figure 33: Comparison of ET-enriched elements in spherules. Results from laser ablation-ICP MS. **(A)** Individual wt% (dotted lines) and the average wt% (green line) of 7 Vee spherules reveal that all six elements are enriched over crustal abundance (orange line), although still less than the wt% averages for CI chondrites (gray line). **(B)** Other elements in extraterrestrial material are highly enriched over crustal abundances: Ni = 330×; Co = 34×; Cr = 38×. Comparing Ni/Co to Ni/Cr ratios of the same 7 Vee spherules to 18 impact-related spherules (Archaen spherule layer, n = 18; age: 2.63-2.49 Ga [67]) shows an excellent overlap. **(C)** A similar overlap occurs when comparing Ni/Co to Ni/Cr ratios of the same 7 Vee spherules to impact-related meltglass (Morokweng crater, n = 8; age: 145 Ma [68] and the Chicxulub crater, n = 60; age: 65 Ma [69]).

crustal abundances, e.g., Ir = 24,000×; Pt = 1500×; Cu = 6×; Fe = 5×; Zn = 4×; and Ni = 330×(Figure 33A) [63]. The results reveal that spherules from the Vee deposit likely comprise mostly melted terrestrial sediments incorporated with small percentages of extraterrestrial material, typically <2 wt% [64–66]. For some PGEs in Perkins spherules, the enrichments are very high: the average Ir concentration is ~20,000× higher than the crustal average, and Pt is ~600× higher.

In addition, we compared Ni/Co and Ni/Cr ratios of Perkins spherules and meltglass to material from known impact events, the 145-Ma Morokweng crater and the 65-Ma Chicxulub crater. Ni, Co, and Cr are helpful for comparison because they are typically elevated over crustal abundances in ET material (Ni = 330×; Co = 33×; and Cr = 38×). The Ni/Co and Ni/Cr ratios for Perkins spherules overlap those from an impact spherule layer dating to 2.63-2.49 Ga, and the Perkins meltglass also overlaps the ratios from two known impacts (Figure 33B, 33C).

The Perkins compositions are similar to those found at multiple YDB sites across 5 continents [26, 58, 70–80]. Most importantly, the Perkins glass-and-spherule deposits are morphologically and compositionally similar to 28 spherule layers identified worldwide [81, 82]. Although only seven of those layers have been positively linked to known impact craters, it is widely accepted that those 28 spherule layers represent evidence of cosmic impact events, even in the absence of known craters [81, 82].

Many of the varieties of spherules, meltglass, metallic flakes, and quartz grains observed in this study display evidence of high-temperature melting or boiling. Their equilibrium melting to boiling points range from ~1050 to 4400°C, with flux-mediated, non-equilibrium melting typically occurring several hundred degrees lower (Table 1). The evidence is consistent with an extremely high-energy thermal event.

12. The lake/depression as an impact crater

There is no conclusive evidence that the Perkins lake/depression is a crater, partially because modern excavations have modified parts of the Perkins lake/depression. However, the collective results suggest that this structure is a possible crater because known impact craters typically display raised rims and are associated with large quantities of high-temperature melted spherules, meltglass, and high-pressure shocked quartz grains [38]. Even so, identification of an impact crater is not required for acceptance as an impact event. Twenty-eight known spherule layers of different ages across the planet are widely accepted as representing impact events, though 21 are not associated with any known craters [81, 82]. Two extensive fields of meltglass, the Libyan Desert glass field and the Australasian tektite field, the world's largest, are widely accepted as having been produced by impact events, even though no craters have been identified [3, 4].

Further research would be beneficial for testing the hypothesis that the lake/depression resulted from a cosmic impact. These studies could include deep-coring the lake/depression in search of a buried bed of spherules and meltglass or conducting geophysical surveys (e.g., gravity, seismic, or airborne magnetic). In addition, we propose exploring smaller depressions near the primary lake/depression to determine if they are also of potential impact origin.

Several previous investigations have concluded that during airbursts at all altitudes, the incoming comet or asteroid is vaporized so that no fragments reach Earth's surface [83, 84]. Thus, the question arises whether the airburst proposed here is possible or plausible.

While most incoming bolide material vaporizes during an airburst, it is indisputable that airburst fragments commonly reach Earth's surface. For example, fragments of the Sikhote-Alin iron meteorite struck Siberia in 1947, distributing ~8500 pieces totaling more than 23,000 kg across 1.6 square km. This event produced more than 100 small impact craters ranging from 0.5 to 26 m diameter [85]. Argentina's Campo del Cielo meteorite field contains numerous meteorites that produced >100 shallow craters up to 26.5 m in diameter and 6 m in depth. Shock pressures were sufficiently energetic for the Sikhote-Alin and Campo del Cielo airbursts to produce multiple small, shallow, shock-generated craters in unconsolidated surficial sediments.

Although the airburst over Chelyabinsk, Russia, in 2013 was a much smaller event than the ones discussed above, fragments still reached Earth's surface. Even though the blast occurred at a height of ~29.7 km with an energy of ~500 kt [83, 86–89], the exploding bolide ejected numerous meteorite fragments, two of which weighed 64.7 and 540 kg [90], the largest of which produced a 9-m diameter hole in the frozen surface of a lake.

Across Western Europe (2.2 million km^2), exploding fragments from eight proposed near-surface airbursts [2] produced shallow craters associated with spherules, meltglass, shocked quartz, and microbrecciated quartz. Co-author K. E. and colleagues investigated most of them across three countries: the Czech Republic [91, 92], Germany [93–109], and Finland [110]. They have been dated to within the last ~11,700 years, averaging one touch-down airburst in Western Europe approximately every 1500 years during the Holocene, making them a geologically common phenomenon.

Thus, there is extensive evidence that airburst fragments can strike Earth's surface with significant force, making surface impacts during airbursts the norm, regardless of whether the airbursts occur at high or low altitudes. If the shock front and thermal pulse are sufficiently intense during an airburst, these conditions can create meltglass, spherules, shocked quartz, and all other evidence observed at the Perkins site.

13. Melted and shocked quartz during an airburst

Airbursts are generally considered to be low-shock events, so the question arises as to whether the required conditions could have occurred to produce shocked quartz in a Perkins airburst. In conducting laboratory experiments to investigate shock quartz, Christie et al. [111–113] showed that melted silica could form in fractured quartz cylinders where the confining pressure was 15 kb (1.5 GPa), inferred to result from frictional melting during brittle fracturing. The evidence indicates pressures equal to or greater than this value produced the materials at Perkins. In addition to high pressures, Gratz et al. [114] found that thermally induced shock metamorphism can occur when high temperatures (≥1710°C) create fractures in quartz that are injected with melted silica. Ernstson performed similar laboratory experiments [115, 116] and observed spallation, during which quartz fractures into multiple fragments through interaction with a compression wave.

The results of Christie et al. and Ernstson suggest a plausible formation mechanism for the Perkins shocked quartz and microbrecciated quartz. Relatively low-energy airburst/impact shockwave pulses could have created compression fractures in quartz grains, and spallation created tensile fractures. Lastly, after the grains fractured, they filled with melted silica either from the grain surface or from melted silica and vapor carried by the high-pressure, high-velocity airburst cloud.

Melted silica within breccia is the primary characteristic distinguishing impact breccia from other geologically deformed breccia [117]. The material at Perkins can be identified as non-authigenic melted silica due to several factors. The glass is determined to be amorphous using crossed polars, thus confirming that it is noncrystalline, and this characteristic eliminates authigenic quartz overgrowth and quartz cement, which are crystalline. Next, SEM imagery detected no micro-spheres in the glass, thus eliminating chert, agate, chalcedony, and other microcrystalline

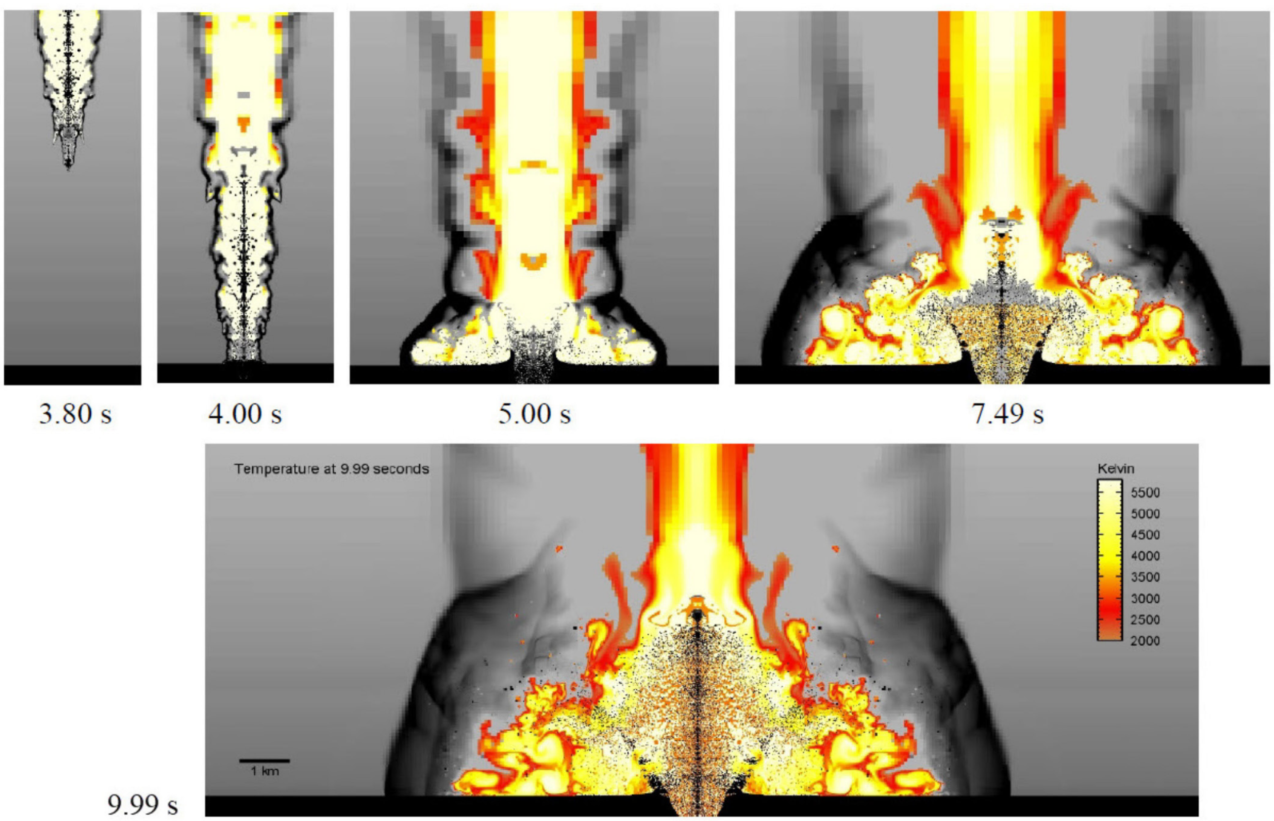

Figure 34: Hydrocode model of asteroid airburst showing crater formation and meltglass production. This model by Boslough and Crawford [3, 4] shows the jet from an asteroid airburst excavating a crater, melting surficial material at >5500 K (yellow on the temperature scale), and ejecting ablated material (small black objects). Melted materials, such as those produced under these conditions, have been observed at Perkins. Figure adapted from Boslough and Crawford [3, 4].

or cryptocrystalline varieties of quartz. Lastly, SEM-EDS indicates that the oxygen/silicon ratio of the glass is ≤53/47 wt%, the stoichiometric ratio of quartz, thus indicating that the glass is not hydrated silica (hyalite at ~66/34 wt% ratio). Therefore, high-temperature melted silica is the only remaining possibility for the Perkins glass.

The shocked quartz and vesicular microbrecciated quartz were observed at all three Perkins locations, often fused to spherules and meltglass, suggesting that they formed simultaneously. As discussed above under potential origins, the most parsimonious explanation is that it resulted from a cosmic impact event.

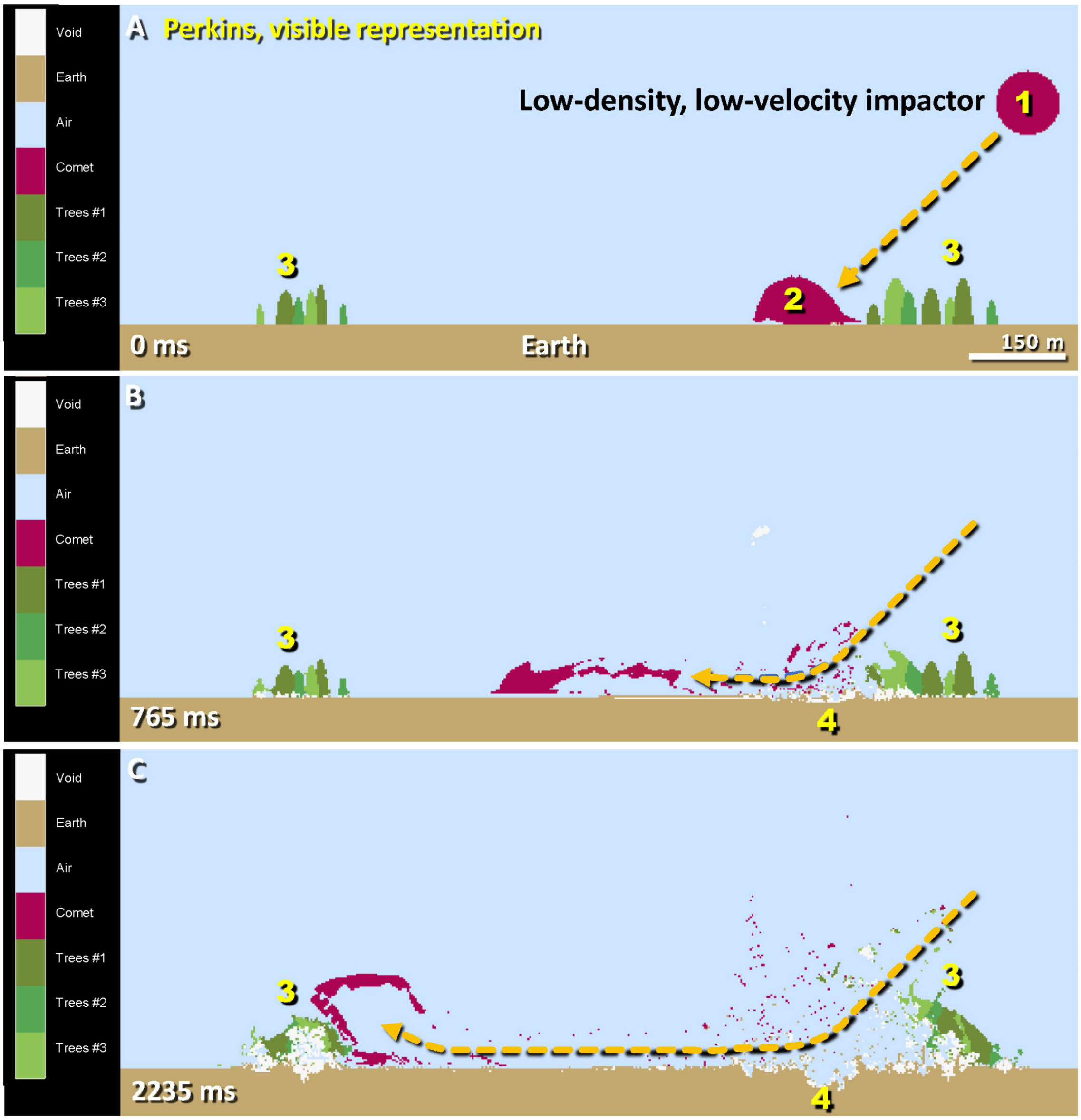

Figure 35: Visible representation, hydrocode model of possible low-density, low-velocity impactor. The legend shows various materials. **(A)** After a 350-m comet broke up in an airburst 108 km high, one 100-m-wide ultra-low-density fragment (red; #1 and #2) struck the Earth, traveling at 0.975 km/s at an angle of 45° (yellow dashed line). Earth's surface was relatively flat with vegetation and trees (#3; not to scale). **(B)** At ~765 ms, the impacting airburst fragment created a shallow crater ~25 m deep (#4). Because the airburst fragment was much less dense than the Earth, it broke into a laterally moving cloud of small particles (red). The impact created pockets of near-vacuum conditions (white) and began to vaporize vegetation (#3). **(C)** After 2235 ms, the crater deepened, and the denser vegetation deflected the low-density impactor cloud. Image created with Autodyn-2D, versions 2023 R1 and 2023 R1 Student (Ansys, Inc.).

14. Hydrocode model of a touch-down airburst

Here, we explore the possibility that the evidence at Perkins resulted from a touch-down airburst, in which the near-surface detonation of an asteroid or comet produced high-velocity fragments that struck the ground with sufficient velocity to create a shallow crater. In addition, the event generated the high-temperature, high-pressure conditions necessary to produce spherules, meltglass, shocked quartz, and the other observed materials.

Multiple studies [2, 12, 118, 119] have produced hydrocode models or reported evidence that airbursts/impacts can produce high-velocity fragments that strike the ground with sufficient velocity to produce glass-filled shocked quartz. In addition, a hydrocode model produced by Boslough and Crawford [62, 120, 121] of a 108-Mt airburst demonstrated that such events can excavate unconsolidated sediment,

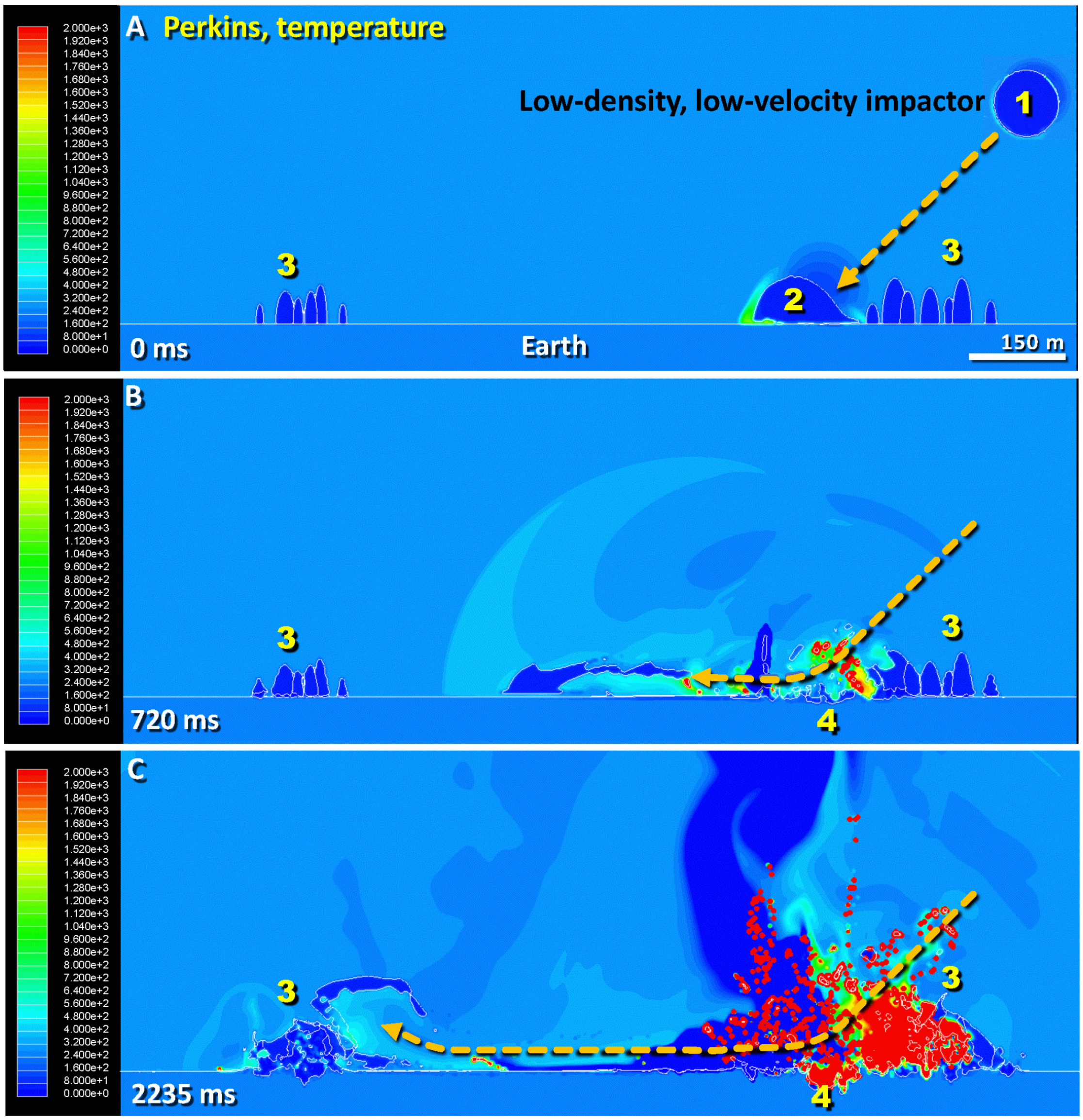

Figure 36: Temperature representation, hydrocode model of possible low-density, low-velocity impactor. (A) A 100-m-wide ultra-low-density fragment (#1 and #2) of a 350-m comet struck the Earth (yellow dashed line) as described in the figure above. **(B)** After 720 ms, the impacting fragment created a shallow crater ~25 m deep (#4). Temperatures rose to >2000°C (red), the boiling point of quartz. At 720 ms, the comet fragment broke into a laterally moving cloud of small particles. The high temperatures began to vaporize vegetation (#3). **(C)** After 2235 ms, the crater deepened, and the >2000°C temperatures continued to melt surficial sediments and vaporize vegetation. Image created with Autodyn-2D, versions 2023 R1 and 2025 R1 Student (Ansys, Inc.).

melt surficial sediments at ~5800 K, and create a crater (Figure 34). Boslough and Crawford [62, 121] describe the theoretical process by which airbursts can produce meltglass. This process is essential, so we quote their conclusion in its entirety. For some airbursts, "the hot jet of vaporized projectile (the descending 'fireball') makes contact with the Earth's surface, where it expands radially. During the time of radial expansion, the fireball can maintain temperatures well above the melting temperature of silicate minerals, and its radial velocity can exceed the sound speed in air. We suggest that the surface materials can ablate by radiative/convective melting under these conditions, and then quench rapidly to form glass after the fireball cools and recedes."

For this study, we also performed computer modeling to investigate whether a cosmic airburst/impact could produce spherules, meltglass, and shocked quartz. Initial conditions were first modeled using the online Earth Impact Effects Program (**Supporting Information, Tables S10 and S11** [5]) [122, 123] as follows: a 350-m-wide comet with a density of 250 kg/m^3 (equivalent to the density of Shoemaker-Levy 9 [124, 125]) entered Earth's atmosphere at 45°, traveling at 30 km/s. The impactor initially broke up into multiple fragments as an airburst at an altitude of 108 km, and these fragments struck Earth's surface as a low-density cloud traveling at 0.975 km/s with an impact energy of 0.64 Mt (Figures 35 and 36). The largest cloud of impactor fragments was modeled as ~100 m in diameter, although it should be noted that this was not a solid object but rather a high-velocity dispersed cloud of debris. This cloud produced a modeled elliptical crater 363 m long and 77 m wide, corresponding well with the 300-m span of the seasonal lake/depression at Perkins. The floor of the modeled crater was underlain by a lens of meltglass tens of meters below the surface, too deep for us to detect with our 6-m test wells.

This hydrocode model confirms that near-surface contact airbursts can produce fragments that strike the Earth with sufficient velocity to produce meltglass, spherules, and shocked quartz. The Earth Impact Effects Program predicts that events similar to the proposed Perkins airburst recur every 19,000 years. The parameters used for modeling with Autodyn are shown in **Supporting Information, Tables S10 and S11** [5]. This model is non-unique; we created dozens of models with varying parameters under which low-density, dispersed comet fragments can produce shallow craters similar to the one modeled here. The numerous variations indicate that these events

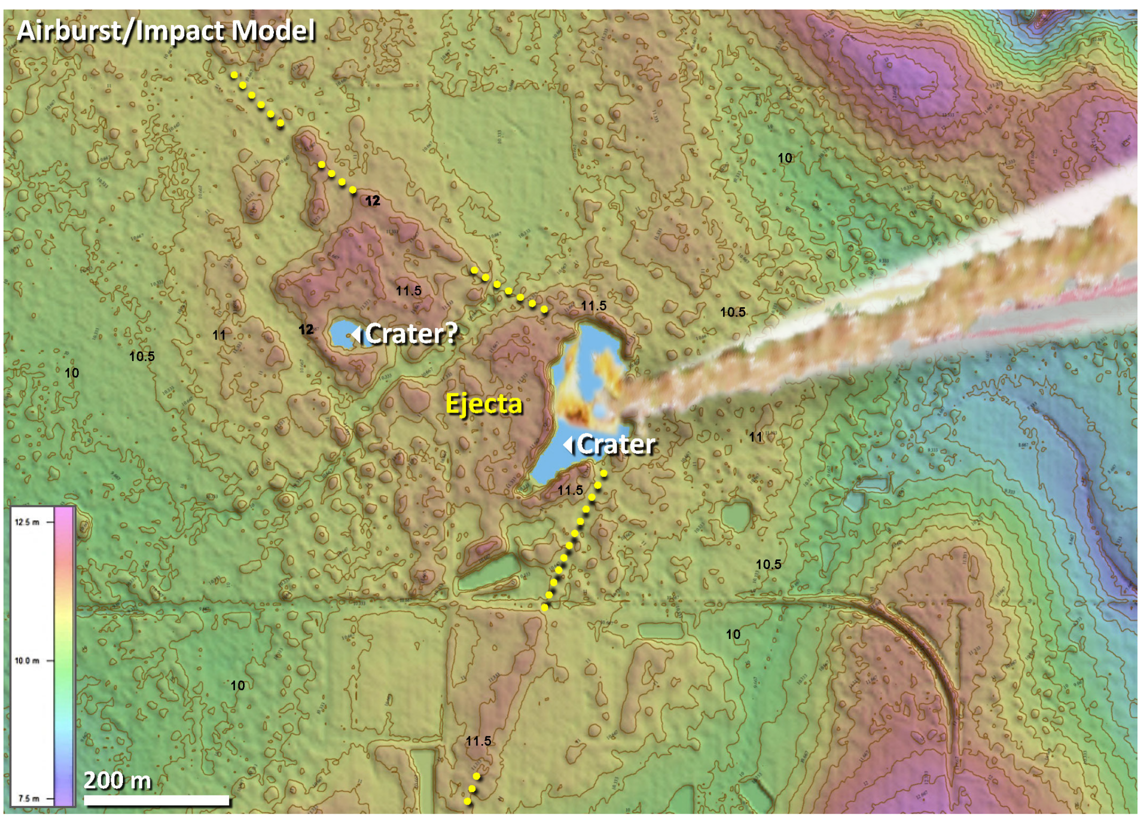

Figure 37: Interpretation of one possible impactor scenario. Based on the hydrocode model, we used a LiDAR-derived digital elevation model to show a potential crater with an ejecta apron to the west, with two possible "wings" of debris extending away from the crater lake. An additional potential crater is shown in blue, which warrants investigation. Elevation in black; the vertical scale is meters above sea level and is exaggerated several times for better visibility. The base figure was created with Global Mapper, v. 8.0.

are common, far more so than typical crater-forming impact events, and the modeled cratering shows that they can potentially cause considerable surface damage [2, 10].

We suggest the following potential airburst/impact scenario for the Perkins site. A large low-density comet entered the atmosphere at a low angle and initially broke up catastrophically at a high altitude. Multiple fragments descended until one or more impacted into or exploded just above the Earth's surface as a "touch-down" or "type-2 contact airburst" [126, 127]. The impact or airburst had sufficient energy to create a shallow-rimmed crater or multiple smaller craters that overlapped to become the modern lake/depression (Figure 37). Smaller fragments struck the ground in a shotgun-like blast, forming multiple ephemeral craters across the site. The airburst/impact ejected surficial sediments that formed a raised rim around the crater, an ejecta blanket to the west, and 'wings' of impact-related debris.

15. Comparison of the Perkins site to other YDB sites and the K-Pg

Several tables below compare the Perkins site to other YDB sites (Table 4) and compare YDB sites to the KPg impact event (Table 5).

Conclusions

Comprehensive analyses of deposits at the Perkins site reveal abundant impact proxies, including Fe- and Si-rich spherules, vesicular meltglass, partially melted quartz grains,

Table 4: Compares multiple proxies at the Perkins site to 25 other YDB sites on four continents.

YDB SITES (26)	Country	Modeled ages	Uncertainty (68%)	Shocked quartz	Aciniform C: Soot	Charcoal; ash	Carbon spherules	Glass-like carbon	Dark layer (black mat)	Microspherules	High-temp meltglass	Nanodiamonds	Pt, Ir, Os, Ni,Co,Cr	Extinct megafauna	Human pop decline
Perkins	LA, US	12794	69	•		•	•	•		•	•		•		
Abu Hureyra	Syria	12825	55	•		•		•	•	•	•	•	•		•
Arlington Cyn	CA, US	12805	55	•	•	•	•		•	•		•	•	•	•
Blackville	SC, US	12820	1080	•	•		•	•		•	•	•	•		
Blackwater Draw	NM, US	12775	365	•		•		•	•	•			•	•	•
Bowser Road	NY, US	12868	--	•					•	•	•	•	•	•	•
Bull Creek	OK, US	12840	75		•							•	•		
Daisy Cave	CA, US	12730	320			•		•	•	•					•
Guil-Mt.Viso	Fr/Ital	12787	34	•			•	•		•			•		
Halls Cave	TX, US	12873	55	•	•				•			•	•	•	
Indian Creek	WY, US	12750	425				•		•			•			•
Lake Cuitzeo	MEX	12850	570			•	•		•	•		•	•	•	•
Lake Hind	Canada	12745	180			•	•	•	•			•	•		
Lindenmeier	CO, US	12775	180			•			•			•		•	
Lingen	GERM	12735	85	•		•	•	•	•	•		•			
Lommel	BELG	12735	790			•	•	•	•	•		•	•		
Melrose	PA, US	12255	2405		•	•	•	•	•	•	•	•	•		
Mucunuque	Venez	12787	34	•			•		•	•	•		•		
Murray Spgs	AZ, US	12750	235	•	•	•	•	•	•	•	•	•	•	•	•
Ommen	Neth	12750	560			•	•	•	•	•		•			
Pilauco	Chile	12770	160	•		•			•	•			•	•	
Sheriden Cave	OH, US	12840	120			•	•		•	•		•	•	•	•
Stara Jimka site	Czech	12805	70			•				•					
Topper	SC, US	12785	185			•	•	•		•		•	•		•
UP-Newtonville	NJ, US	12783	29	•			•	•	•	•	•	•	•		
White Pond	SC, US	12785	58		•				•				•	•	

Table 5: Comparison of evidence for the K-Pg impact with the Younger Dryas Impact Hypothesis.

Evidence Type	K-Pg Boundary (66 Ma)	Younger Dryas Boundary (~12.8 ka)
Shocked quartz	Globally in boundary clay layer; classic shock metamorphism diagnostic of impact	At multiple YDB sites on five continents; morphology and pressure features consistent with hypervelocity shock
Platinum-group elements (Pt, Ir)	Iridium and other PGE anomalies globally distributed; consistent with chondritic impactor	Elevated Pt and Ir reported at many YDB sites, including in Greenland ice cores and terrestrial sections
Spherules and melt-glass	Glassy spherules with aerodynamic shapes; high-temperature condensation and impact ejecta	Magnetic spherules, melt-glass, and lechatelierite found; thermally consistent with temperatures >2200°C
Nanodiamonds	Present but less emphasized in K-Pg debates	Widespread at YDB sites; interpreted as shock products from high-energy atmospheric or surface explosions
High-temperature minerals	Minerals with high melting/boiling points (e.g., chromite) found in ejecta	Refractory minerals (e.g., corundum, spinel, etc.) reported; requires extreme temperature regimes
Native elements	Native iron rarely preserved due to oxidation; found in meteorites, not generally in ejecta	Native iron and other unoxidized metallic phases reported at YDB sites; not explainable by known terrestrial processes
Global wildfire indicators	Charcoal and soot layer globally distributed; modeled as radiation from re-entering ejecta	Charcoal, carbon spherules, and combustion products found widely; interpreted as biomass burning triggered by impact
Crater identification	Chicxulub crater confirmed and precisely dated to K-Pg; fits in size, structure, and age	No confirmed crater; crater not required for multiple airbursts
Multiple spherule layers (global)	Several global spherule layers documented, but K-Pg most precisely matched to crater	>50 sites with impact spherules reported globally
Extinction evidence	Mass extinction at all ecological levels, especially of non-avian dinosaurs	Abrupt megafaunal extinction in North America; timing coincides with YDB; debated association
Black mat / boundary layer	Thin clay layer with global distribution; marks sharp paleo-ecological break	“Black mat” layer found at dozens of sites; rich in carbon and proxies, though stratigraphic correlation debated
Alternative explanations	Competing volcanic hypothesis (Deccan Traps) no longer primary; impact theory dominant	Meltwater pulse hypothesis remains dominant alternative; lacks direct evidence of global effects
Not anthropogenic	Clearly non-anthropogenic; precedes humans	Clear evidence of natural origin; no plausible anthropogenic mechanism for observed markers or extinction patterns
Scientific consensus	Overwhelming support across disciplines for impact hypothesis	Hypothesis remains controversial; strongly supported by some, rejected by others

glass-filled microbrecciated quartz, and shocked quartz grains with glass-filled planar fractures. Radiocarbon dating suggests an age close to the onset of the Younger Dryas (~12,800 cal BP). Geochemical comparisons and thermal estimations indicate that formation temperatures ≥2000°C exceeded those achievable through anthropogenic, volcanic, or tectonic processes.

Hydrocode modeling supports the hypothesis that a low-altitude airburst/impact could have generated the observed depression and associated deposits. While alternative explanations for this material, including natural fluvial or anthropogenic processes, were considered, they fail to account for the full suite of geological and geochemical evidence.

We propose that the Perkins lake/depression represents an airburst/impact crater associated with the Younger Dryas onset and, as such, contributes to the broader understanding of the frequency and effects of cosmic impact events on Earth’s surface environments.

Recent extensive research and observations at this site and elsewhere imply that airbursts have been more common than currently accepted and that numerous easily overlooked such airburst/impact events may have occurred in the past.

Acknowledgments

We gratefully acknowledge the cooperation of Fitzenreiter family members: Walter Leo Fitzenreiter Jr. (deceased), Sarah Fitzenreiter, Walter and Tanya Eubanks, Garren Fitzenreiter, and Seth Dinger. We also thank James Powell and Ken Tankersley for their thoughtful suggestions for improving the manuscript. We are also grateful for the assistance of Eugene Jhong and Brian Muraresku through the Athanatos Foundation, who helped make this research possible. The authors used OpenAI’s ChatGPT (GPT-4, 2025 version) to improve the manuscript’s clarity and structure. The authors critically reviewed and edited all content to ensure accuracy and adherence to scientific standards, following journal ethical guidelines.

Author contributions

R.F., M.A.L., K.E., C.R.M., M.T., G.K., and A.W. conceived and directed aspects of the project. All co-authors contributed data and/or technical analysis for the paper and wrote, edited, reviewed, and/or approved the manuscript.

Funding

The study was funded by the Comet Research Group (CRG) and with the generous support of Eugene Jhong and Brian Muraresku through the Athanatos Foundation, who provided substantial research gifts to the University of California, Santa Barbara (J.P.K) and the University of South Carolina through the South Carolina Institute for Archaeology and Anthropology (C.R.M.). G.K. and MT were funded by the Czech Science Foundation (Grant 23-06075S).

Data availability

Data are provided within the manuscript or supplementary information files.

Sample availability

Key YDB samples for this study are mostly depleted and no longer available.

Potential conflicts of interest

J.P.K., M.A.L., C.R.M., and A.W. volunteer their time as co-founders and directors of CRG. No co-author receives a salary, compensation, stock, or any other financial benefit from CRG, except for tax deductions for CRG donations by co-authors A.W., M.A.L., and T.W. All co-authors may receive reimbursements from their respective organizations for attending symposia on the research presented in this paper. A.W. is a co-author of a book about the Younger Dryas Impact Hypothesis; he donates all proceeds to the non-profit Comet Research Group. The authors declare no other competing interests. M.A.L., C.R.M., and A.W. are editors of this journal but recused themselves and played no role in the review or acceptance of this manuscript.

References

[1] Kletetschka, G.; Takac, M.; Smrcinova, L.; Kavkova, R.; Abbott, D.; LeCompte, M.A.; Moore, C.R.; Kennett, J.P.; Adedeji, V.; Witwer, T.; et al. New Evidence of High-Temperature, High-Pressure Processes at the Site of the 1908 Tunguska Event: Implications for Impact and Airburst Phenomena. *Airburs. Crater. Imp.* **2025**, *3*, 20250001,

[2] West, A.; Young, M.D.; Costa, L.; Kennett, J.P.; Moore, C.R.; LeCompte, M.A.; Kletetschka, G.; Hermes, R.E. Modeling Airbursts by Comets, Asteroids, and Nuclear Detonations: Shock Metamorphism, Meltglass, and Microspherules. *Airburs. Crater. Imp.* **2024**, *2*, 1–30,

[3] Boslough, M.; Crawford, D.A. Low-altitude Airbursts and the Impact Threat. *Int. J. Impact. Eng.* **2008**, *35*, 1441–1448.

[4] Boslough, M.B.; Crawford, D.A. *Low-Altitude Airbursts and the Impact Threat-Final LDRD Report*. Sandia National Lab. (SNL-NM): Albuquerque, NM, USA, 2007, doi: 10.2172/1139983.

[5] Fitzenreiter, R.; et al. SUPPORTING INFORMATION: Evidence of a 12,800-year-old Shallow Airburst Depression in Louisiana with Large Deposits of Shocked Quartz and Melted Materials in *Zenodo.org* 2025.

[6] Hamers, M.F.; Drury, M.R. Scanning Electron Microscope-Cathodoluminescence (SEM-CL) Imaging of Planar Deformation Features and Tectonic Deformation Lamellae in Quartz. *Meteorit. Planet. Sci.* **2011**, *46*, 1814–1831, doi: 10.1111/j.1945.5100.2011.01295.x.

[7] Hamers, M.F.; Pennock, G.M.; Drury, M.R. Scanning Electron Microscope Cathodoluminescence Imaging of Subgrain Boundaries, Twins and Planar Deformation Features in Quartz. *Phys. Chem. Minerals* **2017**, *44*, 263–275, doi: 10.1007/s00269.016.0858.x.

[8] Hamers, M.F.; Pennock, G.M.; Herwegh, M.; Drury, M.R. Distinction Between Amorphous and Healed Planar Deformation Features in Shocked Quartz Using Composite Color Scanning Electron Microscope Cathodoluminescence (SEM-CL) Imaging. *Meteorit. Planet. Sci.* **2016**, *51*, 1914–1931, doi: 10.1111/maps.12711.

[9] French, B.M. *Traces of Catastrophe: A Handbook of Shock-Metamorphic Effects in Terrestrial Meteorite Impact Structures*, Lunar and Planetary Institute, 1998; p. 120.

[10] Silvia, P.J.; Collins, S.; LeCompte, M.A.; Costa, L.; Howard, G.A.; Kennett, J.P.; Moore, C.R.; Kletetschka, G.; Victor Adedeji, A.; Hermes, R.E.; et al. Modeling How a Powerful Airburst Destroyed Tall el-Hammam, a Middle Bronze Age City Near the Dead Sea. *Airburs. Crater. Imp.* **2024**, *2*, 1–52, doi: 10.14293/ACI.2024.0005.

[11] Bunch, T.E.; LeCompte, M.A.; Victor Adedeji, A.; Wittke, J.H.; David Burleigh, T.; Hermes, R.E.; Mooney, C.; Batchelor, D.; Wolbach, W.S.; Kathan, J.; et al. A Tunguska Sized Airburst Destroyed Tall el-Hammam a Middle Bronze Age City in the Jordan Valley Near the Dead Sea. *Sci. Rep.* **2021**, *11*, 18632, doi: 10.1038/s41598.021.97778.3.

[12] Moore, C.R.; LeCompte, M.A.; Kennett, J.P.; Brooks, M.J.; Firestone, R.B.; Ivester, A.H.; Ferguson, T.A.; Lane, C.S.; Duernberger, K.A.; Feathers, J.K.; et al. Platinum, Shock-Fractured Quartz, Microspherules, and Meltglass Widely Distributed in Eastern USA at the Younger Dryas Onset (12.8 ka). *Airburs. Crater. Imp.* **2024**, *2*, 1–31.

[13] Fenneman, N.M. *Oil Fields of the Texas-Louisiana Gulf Coastal Plain*, US Government Printing Office, 1906. p. 146.

[14] OxCal 4.4.4. University of Cambridge, 2021. Available online: http://c14.arch.ox.ac.uk/oxcal.

[15] Kennett, J.P.; Kennett, D.J.; Culleton, B.J.; Aura Tortosa, J.E.; Bischoff, J.L.; Bunch, T.E.; Daniel, I.R.; Erlandson, J.M.; Ferraro, D.; Firestone, R.B.; et al. Bayesian Chronological Analyses Consistent with Synchronous Age of 12,835-12,735 Cal B.P. for Younger Dryas Boundary on Four Continents. *Proc. Natl. Acad. Sci. U. S. A.* **2015**, *112*, E4344–4353, doi: 10.1073/pnas.1507146112.

[16] Perttula, T.K. Paleoindian to middle archaic projectile points from east texas. In *Index of Texas Archaeology: Open Access Gray Literature from the Lone Star State*, 2013; Volume 2013, pp. 27, doi: 10.21112/.ita.2013.1.27.

[17] White, A.A. Functional and Stylistic Variability in Paleoindian and Early Archaic Projectile Points from Midcontinental North America. *N. Am. Archaeol.* **2013**, *34*, 71–108, doi: 10.2190/NA.34.1.c.

[18] Yakubik, J.-K.; Wilkie, L.A.; Weinstein, R.; Schilling, T.; Saunders, J. *Archaeology of Louisiana*. Louisiana State University Press, 2010.

[19] Bronk Ramsey, C. Bayesian Analysis of Radiocarbon Dates. *Radiocarbon* **2009**, *51*, 337–360.

[20] Reimer, P.J.; Austin, W.E.N.; Bard, E.; Bayliss, A.; Blackwell, P.G.; Ramsey, C.B.; Butzin, M.; Cheng, H.; Edwards, R.L.; Friedrich, M.; et al. The IntCal20 Northern Hemisphere Radiocarbon Age Calibration Curve (0–55 cal kBP). *Radiocarbon* **2020**, *62*, 725–757, doi: 10.1017/rdc.2020.41.

[21] Sweatman, M.; Powell, J.; West, A.; Young, M. Rebuttal of Holliday et al.'s Comprehensive Gish Gallop of the Younger Dryas Impact Hypothesis. *Airburs. Crater. Imp.* **2024**, *2*, doi: 10.14293/ACI.2024.0007.

[22] Sweatman, M.B. The Younger Dryas Impact Hypothesis: Review of the Impact Evidence. *Earth Sci. Revi.* **2021**, *218*, 103677.

[23] Kennett, D.J.; West, J.P.; Erlandson, G.J.; Johnson, J.M.; Hendy, J.R.; West, I.L.; Culleton, A.; Jones, B.J.; Stafford, T.L.; Thomas W. Wildfire and Abrupt Ecosystem Disruption on California's Northern Channel Islands at the Ållerød-Younger Dryas Boundary (13.0-12.9 ka). *Quat. Sci. Rev.* **2008**, *27*, 2530–2545.

[24] Lowe, D.R.; Byerly, G.R. The Terrestrial Record of Late Heavy Bombardment. *New Astron. Rev.* **2018**, *81*, 39–61.

[25] Chadwick, B.; Claeys, P.; Simonson, B. New Evidence for a Large Palaeoproterozoic Impact: Spherules in a Dolomite Layer in the Ketilidian Orogen, South Greenland. *J. Geol. Soc.* **2001**, *158*, 331–340.

[26] Moore, A.M.T.; Kennett, J.P.; Napier, W.M.; Bunch, T.E.; Weaver, J.C.; LeCompte, M.; Victor Adedeji, A.; Hackley, P.; Kletetschka, G.; Hermes, R.E.; et al. Evidence of Cosmic Impact at Abu Hureyra, Syria at the Younger Dryas Onset (~12.8 ka): High-temperature Melting at >2200°C. *Sci. Rep.* **2020**, *10*, 4185, doi: 10.1038/s41598.020.60867.w.

[27] Tselmovich, V.; Kurazhkovskii, A.Yu.; Kazansky, A.Yu.; Shchetnikov, A.A.; Blyakharchuk, T.A. Catastrophic events in the holocene and their registration in peat deposits. In *Proceedings of the 11th Intl School and Conference "Problems of Geocosmos", 3–7 October 2016, St. Petersburg, Russia*, 2016; pp. 91–98.

[28] Tselmovich, V.A.; Kurazhkovskii, A.Y.; Kazansky, A.Y.; Shchetnikov, A.A.; Blyakharchuk, T.A.; Philippov, D.A. Studying the Dynamics of Cosmic Dust Flux on the Earth's Surface from Peat Deposits. *Izvestiya, Physics of the Solid Earth* **2019**, *55*, 517–527, doi: 10.1134/S1069351319030108.

[29] Tselmovich, V.A. Composition and microscopic features of background cosmic dust from peat. In *Minerals: Structure, Properties, Methods of Investigation: 9th Geoscience Conference for Young Scientists, Ekaterinburg, Russia, February 5–8*, 2020, 2018; pp. 253–259.

[30] Sungatullin, R.H.; Bahtin A.I.; Vorobev V.V.; Osin J.N.; Guzel S.; Vladimir A.T. Composition and Morphology of Metal Microparticles in Paleozoic Sediments of Caspian Depression. *Int. J. Appl. Eng. Res.* **2015**, *10*, 45372–45382.

[31] Sungatullin, R.K.; Sungatullina, G.M.; Zakirov, M.I.; Tsel'movich, V.A.; Glukhov, M.S.; Bakhtin, A.I.; Osin, Y.N.; Vorob'ev, V.V. Cosmic Microspheres in the Carboniferous Deposits of the Usolka Section (*Urals foredeep*). *Russ. Geol. Geophys.* **2017**, *58*, 59–69, doi: 10.1016/j.rgg.2016.12.003.

[32] Pechersky, D.; Markov, G.; Tsel'movich, V. Pure Iron and Other Magnetic Minerals in Meteorites. *Solar Syst. Res.* **2015**, *49*, 61–71, doi: 10.1134/S0038094614060070.

[33] Poelchau, M.H.; Kenkmann, T. Feather Features: A Low-shock-pressure Indicator in Quartz. *J. Geophys. Res. Solid Earth* **2011**, *116*, doi: 10.1029/2010JB007803.

[34] Gratz, A. Deformation in Laboratory-shocked Quartz. *J. Non-Cryst. Solids* **1984**, *67*, 543–558, doi: 10.1016/0022.3093(84)90175.3.

[35] Bohor, B.F. Shocked Quartz and More; Impact Signatures in Cretaceous/Tertiary Boundary Clays In *Global Catastrophes in Earth History; An Interdisciplinary Conference on Impacts, Volcanism, and Mass Mortality;* Sharpton, V.L., Ward, P.D., Eds.; Geological Society of America, 1990.

[36] Goltrant, O.; Cordier, P.; Doukhan, J.-C. Planar Deformation Features in Shocked Quartz; a Transmission Electron Microscopy Investigation. *Earth Planet. Sci. Lett.* **1991**, *106*, 103–115, doi: 10.1016/0012.821X(91)90066.Q.

[37] Gratz, A.J.; Fisler, D.K.; Bohor, B.F. Distinguishing Shocked from Tectonically Deformed Quartz by the use of the SEM and Chemical Etching. *Earth Planet. Sci. Lett.* **1996**, *142*, 513–521, doi: 10.1016/0012.821X(96)00099.4.

[38] French, B.M.; Koeberl, C. The Convincing Identification of Terrestrial Meteorite Impact Structures: What Works, what Doesn't, and why. *Earth Sci. Rev.* **2010**, *98*, 123–170, doi: 10.1016/j.earscirev.2009.10.009.

[39] Bunch, T.; Cohen, A.J. Shock Deformation of Quartz from Two Meteorite Craters. *Geol. Soc. Am. Bull.* **1964**, *75*, 1263–1266.

[40] Bunch, T.E. *A Study of Shock-Induced Microstructures And Solid State Transformations of Several Minerals from Explosion Craters*, Ph.D thesis, University of Pittsburgh, 1966.

[41] Voorn, M. *A New Way to Confirm Meteorite Impact Produced Planar Features in Quartz: Combining Universal Stage and Electron Backscatter Diffraction Techniques*, 2010.

[42] Huber, M.S.; FerriÈRe, L.; Losiak, A.; Koeberl, C. ANIE: A Mathematical Algorithm for Automated Indexing of Planar Deformation Features in Quartz Grains. *Meteorit. Planet. Sci.* **2011**, *46*, 1418–1424, doi: 10.1111/j.1945.5100.2011.01234.x.

[43] Losiak, A.; Belcher, C.M.; Plado, J.; Jõeleht, A.; Herd, C.D.K.; Kofman, R.S.; Szokaluk, M.; Szczuciński, W.; Muszyński, A.; Wild, E.M.; et al. Small Impact Cratering Processes Produce Distinctive Charcoal Assemblages. *Geology* **2022**, *50*, 1276–1280, doi: 10.1130/g50056.1.

[44] Losiak, A. *Geochemical, Isotopic, and Petrographic Investigations of Rocks from the Bosumtwi Impact*, 2013.

[45] Bischoff, A.; Stöffler, D. Chemical and Structural Changes Induced by Thermal Annealing of Shocked Feldspar Inclusions in Impact Melt Rocks from Lappajärvi Crater, Finland. *J. Geophys. Res. Solid Earth* **1984**, *89*, B645–B656, doi: 10.1029/JB089iS02p0B645.

[46] Kaliwoda, M.; et al. Quartz and cristobalite ballen aggregates formed by dehydration of shock-generated amorphous phases in impact melt rocks from the ries imapct structure (Germany). In *52nd Lunar and Planetary Science Conference*, 2021; pp. 2445.

[47] Koeberl, C.; Ferrière, L. Libyan Desert Glass area in Western Egypt: Shocked Quartz in Bedrock Points to a Possible Deeply Eroded Impact Structure in the Region. *Meteorit. Planet. Sci.* **2019**, *54*, 2398–2408, doi: 10.1111/maps.13250.

[48] Longo, G.; Di Martino, M. Remote sensing investigation of the tunguska explosion area. In *Remote Sensing for Agriculture, Ecosystems, and Hydrology IV*, 2003; Volume 4879, pp. 326–333.

[49] Longo, G.; Di Martino, M.; Anfinogenov, J.; Budaeva, L.; Kovrigin, E.; Andreev, G.; A New Unified Catalogue and a New Map of the 1908 Tree Fall in the Site of the Tunguska Cosmic Body Explosion. *Asteroid-Comet Hazard* **2005**, *2005*, 222–225.

[50] Ernstson, K.; Müller, W.; Gawlik-Wagner, A.; West, A. The new world of impact cratering: The high-resolution digital terrain model and hydrocode modeling – The Saarland (Germany) low altitude touchdown airburst impact event. In *Lunar and Planetary Science Conference*, 2025.

[51] Shuvalov, V. A Mechanism for the Production of Crater Rays. *Meteorit. Planet. Sci.* **2012**, *47*, 262–267, doi: 10.1111/j.1945.5100.2011.01324.x.

[52] Pilkington, M.; Grieve, R.A.F. The Geophysical Signature of Terrestrial Impact Craters. *Rev. Geophys.* **1992**, *30*, 161–181, doi: 10.1029/92RG00192.

[53] Niyogi, A.; Pati, J.K.; Patel, S.C.; Panda, D.; Patil, S.K. Anthropogenic and Impact Spherules: Morphological Similarity and Chemical Distinction–A Case Study from India and its Implications. *J. Earth Syst. Sci.* **2011**, *120*, 1043–1054.

[54] Houser, L.M.; Ault, A.K.; Newell, D.L.; Evans, J.P.; Shen, F.-A.; Van Devener, B.R. Nanoscale Textural and Chemical Evolution of Silica Fault Mirrors in the Wasatch Fault Damage Zone, Utah, USA. *Geochem. Geophys. Geosyst.* **2021**, *22*, e2020GC009368, doi: 10.1029/2020GC009368.

[55] Janssen, C.; Wirth, R.; Rybacki, E.; Naumann, R.; Kemnitz, H.; Wenk, H.-R.; Dresen, G. Amorphous Material in SAFOD Core Samples (San Andreas Fault): Evidence for Crush-origin Pseudotachylytes? *Geophys. Res. Lett.* **2010**, *37*, doi: 10.1029/2009GL040993.

[56] Bohor, B.; Fisler, D.; Gratz, A.J. Distinguishing between shock and tectonic lamellae with the SEM. In *Lunar and Planetary Science Conference*, 1995; Volume 26, pp. 145.

[57] Anders, M.H.; Laubach, S.E.; Scholz, C.H. Microfractures: A Review. *J. Struct. Geol.* **2014**, *69*, 377–394.

[58] Bunch, T.E.; Hermes, R.E.; Moore, A.M.; Kennett, D.J.; Weaver, J.C.; Wittke, J.H.; DeCarli, P.S.; Bischoff, J.L.; Hillman, G.C.; Howard, G.A.; et al. Very High-Temperature Impact Melt Products as Evidence for Cosmic Airbursts and Impacts 12,900 Years Ago. *Proc. Natl. Acad. Sci. U. S. A.* **2012**, *109*, E1903–E1912, doi: 10.1073/pnas.1204453109.

[59] Moore, A.M.T.; Kennett, J.P.; Napier, W.M.; Bunch, T.E.; Weaver, J.C.; LeCompte, M.A.; Victor Adedeji, A.; Kletetschka, G.; Hermes, R.E.; Wittke, J.H.; et al. Abu Hureyra, Syria, Part 2: Additional Evidence Supporting the Catastrophic Destruction of this Prehistoric Village by a Cosmic Airburst ~12,800 Years Ago. *Airburs. Crater. Imp*. **2023**, *1*, doi: 10.14293/ACI.2023.0002.

[60] Yuen, D.A.; Scruggs, M.A.; Spera, F.J.; Zheng, Y.; Hu, H.; McNutt, S.R.; Thompson, G.; Mandli, K.; Keller, B.R.; Wei, S.S.; et al. Under the Surface: Pressure-Induced Planetary-Scale Waves, Volcanic Lightning, and Gaseous Clouds Caused by the Submarine Eruption of Hunga Tonga-Hunga Ha'apai Volcano. *Earthq. Res. Adv.* **2022**, *2*, 100134, doi: 10.1016/j.eqrea.2022.100134.

[61] Rakov, V.A.; Uman, M.A. *Lightning: Physics and Effects.* Wiley Online Library, 2004.

[62] Boslough, M. Airburst modeling. In *Handbook of Cosmic Hazards and Planetary Defense*, 2021; pp. 1–24, doi: 10.1007/978.3.319.02847.7_56.1.

[63] Rudnick, R.L.; Gao, S. Composition of the continental crust. In *Treatise on Geochemistry* Rudnick, R.L., Ed.; Elsevier, 2003; Volume 3, pp. 1–64.

[64] Koeberl, C. The Geochemistry and Cosmochemistry of Impacts. *Treatise Geochem.* **2003**, *1*, 739–791, doi: 10.1016/B978.008043751.4/00228.5.

[65] Huber, M.S.; Köberl, C. Distribution of Meteoritic Material in Sudbury Ejecta. *Meteorit. Planet. Sci.* **2012**, *47*, A200.

[66] Wakita, S.; Johnson, B.C.; Denton, C.A.; Davison, T.M. Jetting During Oblique Impacts of Spherical Impactors. *Icarus* **2021**, *360*, 114365.

[67] Simonson, B.M.; McDonald, I.; Shukolyukov, A.; Koeberl, C.; Reimold, W.U.; Lugmair, G.W. Geochemistry of 2.63–2.49 Ga Impact Spherule Layers and Implications for Stratigraphic Correlations and Impact Processes. *Precambrian Res.* **2009**, *175*, 51–76, doi: 10.1016/j.precamres.2009.08.004.

[68] Koeberl, C. Geochemistry and Petrography of Impact Breccias and Target Rocks from the 145 Ma Morokweng Impact Structure, South Africa. *Geoch. Cosm. Acta* **2003**, *67*, 1837–1862, doi: 10.1016/S0016.7037(02)00994.8.

[69] Goderis, S.; Tagle, R.; Belza, J.; Smit, J.; Montanari, A.; Vanhaecke, F.; Erzinger, J. Claeys, P. Reevaluation of Siderophile Element Abundances and Ratios Across the Cretaceous–Paleogene (K–Pg) Boundary: Implications for the Nature of the Projectile. *Geochim. Cosm. Acta* **2013**, *120*, 417–446, doi: 10.1016/j.gca.2013.06.010.

[70] Firestone, R.B.; West, A.; Kennett, J.P.; Becker, L.; Bunch, T.E.; Revay, Z.S.; Schultz, P.H.; Belgya, T.; Kennett, D.J.; Erlandson, J.M.; et al. Evidence for an Extraterrestrial Impact 12,900 Years Ago that Contributed to the Megafaunal Extinctions and the Younger Dryas Cooling. *Proc. Natl. Acad. Sci. U. S. A.* **2007**, *104*, 16016–16021, doi: 10.1073/pnas.0706977104.

[71] Firestone, R.B.; West, A.; Revay, Z.; Hagstrum, J.T.; Belgya, T.; Hee, S.S.Q.; Smith, A.R. Analysis of the Younger Dryas Impact Layer. *J. Sib. Fed. Univ.* **2010**, *1*, 30–62.

[72] Hagstrum, J.T.; Firestone, R.B.; West, A.; Weaver, J.C.; Bunch, T.E. Impact-related Microspherules in Late Pleistocene Alaskan and Yukon "muck" Deposits Signify Recurrent Episodes of Catastrophic Emplacement. *Sci. Rep.* **2017**, *7*, 16620, doi: 10.1038/s41598.017.16958.2.

[73] Israde-Alcantara, I.; Bischoff, J.L.; Domínguez-Vázquez, G.; Li, H.-C.; DeCarli, P.S.; Bunch, T.E.; Wittke, J.H.; Weaver, J.C.; Firestone, R.B.; West, A.; et al. Evidence from Central Mexico Supporting the Younger Dryas Extraterrestrial Impact Hypothesis. *Proc. Natl. Acad. Sci. U. S. A.* **2012**, *109*, E738–E747, doi: 10.1073/pnas.1110614109.

[74] LeCompte, M.A.; Goodyear, A.C.; Demitroff, M.N.; Batchelor, D.; Vogel, E.K; Mooney, C.; Rock, B.N.; Seidel, A.W. Independent Evaluation of Conflicting Microspherule Results from Different Investigations of the Younger Dryas Impact Hypothesis. *Proc. Natl. Acad. Sci. U. S. A.* **2012**, *109*, E2960–2969, doi: 10.1073/pnas.1208603109.

[75] LeCompte, M.A.; West, A.; Adededji, A.; Demitroff, M.; Witwer, T.; Langenburg, R.A. The Bowser Road Mastodon and the Younger Dryas Impact Hypothesis, Appendix 3. In *The Archaeological Recovery of the Bowser Road Mastodon, Orange County, NY*; Gramly, R.M., Ed.; Persimmon Press, 2017.

[76] Pino, M.; Abarzúa, A.M.; Astorga, G.; Martel-Cea, A.; Cossio-Montecinos, N.; Navarro, R.X.; Lira, M.P.; Labarca, R.; LeCompte, M.A.; Adedeji, V.; et al. Sedimentary Record from Patagonia, Southern Chile Supports Cosmic-Impact Triggering of Biomass Burning, Climate Change, and Megafaunal Extinctions at 12.8 ka. *Sci. Rep.* **2019**, *9*, 4413, doi: 10.1038/s41598.018.38089.y.

[77] Teller, J.; Boyd, M.; LeCompte, M.; Kennett, J.; West, A.; Telka, A.; Diaz, A.; Adedeji, V.; Batchelor, D.; Mooney, C.; et al. A Multi-proxy Study of Changing Environmental Conditions in a Younger Dryas Sequence in Southwestern Manitoba, Canada, and Evidence for an Extraterrestrial Event. *Quat. Res.* **2019**, *93*, 60–87, doi: 10.1017/qua.2019.46.

[78] Wu, Y.; Sharma, M.; LeCompte, M.A.; Demitroff, M.N.; Landis, J.D. Origin and Provenance of Spherules and Magnetic Grains at the Younger Dryas Boundary. *Proc. Natl. Acad. Sci. U. S. A.* **2013**, *110*, E3557–E3566, doi: 10.1073/pnas.1304059110.

[79] Wittke, J.H.; Weaver, J.C.; Bunch, T.E.; Kennett, J.P.; Kennett, D.J.; Moore, A.M.T.; Hillman, G.C.; Tankersley, K.B.; Goodyear, A.C.; Moore, C.R.; et al. Evidence for Deposition of 10 Million Tonnes of Impact Spherules Across Four Continents 12,800 y Ago. *Proc. Natl. Acad. Sci. U. S. A.* **2013**, *110*, E2088–E2097, doi: 10.1073/pnas.1301760110.

[80] Golyeva, A.; Druzhinina, O. Microbiomorphous Analysis in the Study of Late-Glacial Environment: Preliminary Results of the Study of the Kulikovo Section (Sambian Peninsula, Kaliningrad Region). *Izvestia Ras. Geographical Series* **2024**, *88*, 77–89.

[81] Glass, B.P.; Simonson, B.M. Mesozoic spherule/impact ejecta layers. In *Distal Impact Ejecta Layers*. Berlin, Heidelberg: Springer, 2013; pp. 245–320, doi: 10.1007/978.3.540.88262.6_5.

[82] Glass, B.P.; Simonson, B.M. Distal Impact Ejecta Layers: Spherules and More. *Elements* **2012**, *8*, 43–48, doi: 10.2113/gselements.8.1.43.

[83] Artemieva, N.; Shuvalov, V. Atmospheric Shock Waves After Impacts of Cosmic Bodies Up to 1000 m in Diameter. *Meteorit. Planet Sci.* **2019**, *54*, 592–608, doi: 10.1111/maps.13229.

[84] Van Ginneken, M.; Goderis, S.; Artemieva, N.; Debaille, V.; Decrée, S.; Harvey, R.P.; Huwig, K.A.; Hecht, L.; Yang, S.; Kaufmann, F.E.D.; et al. A Large Meteoritic Event Over Antarctica ca. 430 ka Ago Inferred from Chondritic Spherules from the Sor Rondane Mountains. *Sci. Adv.* **2021**, *7*, eabc1008, doi: 10.1126/sciadv.abc1008.

[85] Martel, L.M. Better Know A Meteorite Collection: Natural History Museum in London, United Kingdom. *Planet. Sci. Res. Discov. Rep*. **2009**, *136*, 1–10.

[86] Artemieva, N.A.; Shuvalov, V.V. From Tunguska to Chelyabinsk Via Jupiter. *Annu. Rev. Earth Planet. Sci.* **2016**, *44*, 37–56, doi: 10.1146/annurev.earth.060115.012218.

[87] Kletetschka, G.; Vyhnanek, J.; Kawasumiova, D.; Nabelek, L.; Petrucha, V. Localization of the Chelyabinsk Meteorite from Magnetic Field Survey and GPS Data. *IEEE Sens. J.* 2015, *15*, 4875–4881, doi: 10.1109/JSEN.2015.2435252.

[88] Brown, P.G.; Assink, J.D.; Astiz, L.; Blaauw, R.; Boslough, M.B.; Borovička, J.; Brachet, N.; Brown, D.; Campbell-Brown, M.; Ceranna, L.; et al. A 500-Kiloton Airburst Over Chelyabinsk and an Enhanced Hazard from Small Impactors. *Nature* **2013**, *503*, 238–241, doi: 10.1038/nature12741.

[89] Popova, O.P.; Jenniskens, P.; Emel'yanenko, V.; Kartashova, A.; Biryukov, E.; Khaibrakhmanov, S.; Shuvalov, V.; Rybnov, Y.; Dudorov, A.; Grokhovsky, VI.; et al. Chelyabinsk Airburst, Damage Assessment, Meteorite Recovery, and Characterization. *Science* **2013**, *342*, 1069–1073, doi: 10.1126/science.1242642.

[90] Kocherov, A.; Korochantsev, A.; Lorenz, C.; Ivanova, M.; Grokhovsky, V. Recovery, laboratory preparation and current state of the main mass of the Chelyabinsk meteorite. In *45th Annual Lunar and Planetary Science Conference*, 2014; p. 2227.

[91] Molnár, M.; Ventura, K.; Švanda, P.; Štaffen, Z.; Rappenglück, M.A.; Ernstson, K. Chrudim-Pardubice: Evidence for a young meteorite impact strewn field in the Czech Republic. In *48th Annual Lunar and Planetary Science Conference*, 2017; p. 1920.

[92] Poßekel, J.; Molnár, M.; Ernstson, K. The proposed meteorite impact event in the Czech Republic: Evidence strengthened by investigations with the digital terrain model. In *53rd Lunar and Planetary Science Conference* 2678, 2022; p. 1558.

[93] Ernstson, K.; Müller, W.; Gawlik-Wagner, A. The Saarlouis semi crater structure: Notable insight into the Saarland (Germany) meteorite impact event achieved. In *49th Lunar and Planetary Science Conference*, 2018; Abstract #1876.

[94] Ernstson, K.; Portz, D.; Müller, W. Zhamanshinite-like black-glass melt rocks from the Saarland (Germany) meteorite impact site. In *52nd Lunar and Planetary Science Conference*, 2021; p. 1350.

[95] Siegel, U.; Rommelfangen, J.; Müller, W.; Michelbacher, S.; Ernstson, K. Shatter cones in Litermont Quartzites: Saarlouis/Nalbach (Saarland, Germany) meteorite impact event strengthened. In *Lunar and Planetary Science Conference*, 2022; Abstract #1842.

[96] Ernstson, K.; Bauer, F.; Hiltl, M. A Prominent Iron Silicides Strewn Field and Its Relation to the Bronze Age/Iron Age Chiemgau Meteorite Impact Event (Germany). *Earth Sci.* **2023**, *12*, 26–40, doi: 10.11648/j.earth.20231201.14.

[97] Ernstson, K.; Mayer, W.; Neumair, A.; Rappenglück, B.; Sudhaus, D. The Chiemgau crater strewn field: Evidence of a Holocene large impact event in Southeast Bavaria, Germany. *J. Sib. Fed.* **2010**, *3*, 72–103.

[98] Ernstson, K.; Poßekel, J.; Rappenglück, M.A. Near-ground airburst cratering: Petrographic and ground penetrating radar (GPR) evidence for a possibly enlarged Chiemgau impact event (Bavaria, SE-Germany). In *Lunar and Planetary Science Conference*, 2020; p. 1231.

[99] Ernstson, K.; Sideris, C.; Liritzis, I.; Neumair, A. The Chiemgau Meteorite Impact Signature of the Stöttham Archaeological Site (Southeast Germany). *Mediterr. Archaeol. Archaeom.* **2012**, *12*, 249–259.

[100] Rappenglück, B.; Hiltl, M.; Ernstson, K. Artifact-in-impactite: A new kind of impact rock. Evidence from the Chiemgau meteorite impact in southeast Germany. In *Proceedings of the Modern Problems of Theoretical, Experimental, and Applied Mineralogy, Yushkin Readings, Syktyvkar, Russia, 7–10 December 2020*, 2020; pp. 365–367.

[101] Rappenglück, B.; Hiltl, M.; Ernstson, K. Metallic artifact remnants in a shock-metamorphosed impact breccia: An extended view of the archeological excavation at Stöttham (Chiemgau, SE-Germany). In *50th Annual Lunar and Planetary Science Conference*, 2019; p. 1334.

[102] Rappenglück, M.A.; Ernstson, K.; Mayer, W.; Beer, R.; Benske, G.; Siegl, C.; Sporn, R.; Bliemetsrieder, T.; Schüssler, U. *The Chiemgau Impact Event in the Celtic Period: Evidence of a Crater Strewnfield and a Cometary Impactor Containing Presolar Matter*; Impakt c/o Kord Ernstson: Chiemgau, 2004.

[103] Rappenglück, B.; Hiltl, M.; Poßekel, J.; Rappenglück, M.A.; Ernstson, K. People Experienced the Prehistoric Chiemgau Meteorite Impact – Geoarchaeological Evidence from Southeastern Germany: A Review. *Mediterr. Archaeol. Archaeom.* **2023**, *23*, 1–29, doi: 10.5281/zenodo.7775799.

[104] Rappenglück, B.; Hiltl, M.; Ernstson, K. Exceptional evidence of a prehistoric meteorite impact at the archaeological site of Stöttham (Chiemgau, SE-Germany). In *Harmony and Symmetry: Celestial Regularities Shaping Human Culture. Proceedings of the SEAC 2018 Conference*; Draxler, S., Lippitsch, M.E., Wolfschmidt, G., Eds., Hamburg, 2020; 116–125.

[105] Rappenglück, B.; Hiltl, M.; Ernstson, K. The Chiemgau impact: Evidence of a latest bronze age/early iron age meteorite impact in the archaeological record, and resulting critical considerations of catastrophism. In *Beyond Paradigms in Cultural Astronomy*; González-García, C., Frank, R.M., Sims, L.D., Rappenglück, M.A., Zotti, G., Belmonte, J.A., Šprajc, I., Eds.; BAR Publishing, 2021; pp. 57–64.

[106] Shumilova, T.G.; Isaenko, S.I.; Ulyashev, V.V.; Makeev, B.A.; Rappenglück, M.A.; Veligzhanin, A.A.; Ernstson, K. Enigmatic Glass-Like Carbon from the Alpine Foreland, Southeast Germany: A Natural Carbonization Process. *Acta Geol. Sin.-Engl. Ed.* **2018**, *92*, 2179–2200.

[107] Waldmann, G.; Herten, F.; Hiltl, M.; Ernstson, K. The enigmatic Niederrhein (Germany) deposit: Evidence of a middle-pleistocene meteorite impact strewn field. In *49th Annual Lunar and Planetary Science Conference*, 2018; p. 1610.

[108] Ernstson, K.; Schulz-Hertlein, G.; Ernstson, T.; Poßekel, J. A probable holocene meteorite impact crater strewn field in Lower Franconia (Germany): Evidence from digital terrain models and geophysical surveys (GPR, electrical imaging, geomagnetics). In *Poster, Proceedings of the AGU Fall Meeting*, 2022.

[109] Ernstson, K.; Poßekel, J.; Kurtz, J. The enigmatic sachsendorf bay structure (Oderbruch, Northeast Germany): Evidence of a pleistocene/holocene meteorite impact event. In *12th Planetary Crater Consortium Meeting* 12, 2022, 2021.

[110] Ahokas, H. *Thirty-three Previously Unknown Meteoritic Craters of Diameter From 5 to 100 m in Western Kouvola, Finland From a Swarm of Impactors in the Holocene*, Kave, 2023.

[111] Christie, J.; Ardell, A. Substructures of Deformation Lamellae in Quartz. *Geology* **1974**, *2*, 405–408, doi: 10.1130/0091-7613(1974)2<405:SODLIQ>2.0.CO;2.

[112] Christie, J.; Griggs, D.; Carter, N. Experimental Evidence of Basal Slip in Quartz. *J. Geol.* **1964**, *72*, 734–756, doi: 10.1086/627030.

[113] Christie, J.M.; Raleigh, C.B. The Origin of Deformation Lamellae in Quartz. *Am. J. Sci.* **1959**, *257*, 385–407, doi: 10.2475/ajs.257.6.385.

[114] Gratz, A.; Nellis, W.J.; Christie, J.M.; Brocious, W.; Swegle, J.; Cordier, P. Shock Metamorphism of Quartz with Initial Temperatures −170 to + 1000° C. *Phys. Chem. Minerals* **1992**, *19*, 267–288, doi: 10.1007/BF00204005.

[115] Ernstson, K. Meteorite impact spallation: From mega- to micro-scale. Available online: http://www.impact-structures.com/impact-educational/meteorite-impact-spallation-from-mega-to-micro-scale/ (2014).

[116] Ernstson, K.; Poßekel, J. Enigmatic meteorite impact signature: Field evidence and ground penetrating radar (GPR) measurements suggest megascopic impact spallation features. In *AGU Fall Meeting Abstracts* 2019, 2019; EP53F–2239.

[117] Dressler, B.; Reimold, W. Terrestrial Impact Melt Rocks and Glasses. *Earth Sci. Rev*. **2001**, *56*, 205–284, doi: 10.1016/S0012.8252(01)00064.2.

[118] Hermes, R.E.; Wenk, H.-R.; Kennett, J.P.; Bunch, T.E.; Moore, C.R.; LeCompte, M.A.; Kletetschka, G.; Adedeji, A.V.; Langworthy, K.; Razink, J.J.; et al. Microstructures in Shocked Quartz: Linking Nuclear Airbursts and Meteorite Impacts. *Airbursts and Cratering Impacts* **2023**, *1*, 1–40, doi: 10.14293/ACI.2023.0001.

[119] Moore, A.M.T.; Kennett, J.P.; LeCompte, M.A.; Moore, C.R.; Li, Y.-Q.; Kletetschka, G.; Langworthy, K.; Razink, J.J.; Brogden, V.;

van Devener, B.; et al. Abu Hureyra, Syria, Part 1: Shock-fractured quartz grains support 12,800-year-old Cosmic Airburst at the Younger Dryas Onset. *Airbursts Cratering Impacts* **2023**, *1*, 1–28, doi: 10.14293/ACI.2023.0003.

[120] Boslough, M. Computational modeling of low-altitude airbursts. In *AGU Fall Meeting*, 2007; Abstracts, #U21E-03.

[121] Boslough, M. Airburst modeling. In *First International Workshop on Potentially Hazardous Asteroids Characterization, Atmospheric Entry and Risk Assessment, 7–9 July, 2015*. NASA Ames Research Center, 2015.

[122] Collins, G.S.; Lynch, E.; McAdam, R.; Davison, T.M. A Numerical Assessment of Simple Airblast Models of Impact Airbursts. *Meteorit. Planet. Sci.* **2017**, *52*, 1542–1560, doi: 10.1111/maps.12873.

[123] Collins, G.S.; Melosh, H.J.; Marcus, R. Earth Impact Effects Program: A Web-based Computer Program for Calculating the Regional Environmental Consequences of a Meteoroid Impact on Earth. *Meteorit. Planet. Sci.* **2005**, *40*, 817–840, doi: 10.1111/j.1945.5100.2005.tb00157.x.

[124] Sekanina, Z.; Chodas, P.W.; Yeomans, D.K. Tidal Disruption and the Appearance of Periodic Comet Shoemaker-Levy 9. *Astron. Astrophys.* **1994**, *289*, 607–636.

[125] Crawford, D.A. Comet Shoemaker-Levy 9 Fragment Size Estimates: How Big Was the Parent Body? *Ann. N. Y. Acad. Sci.* **1997**, *822*, 155–173, doi: 10.1111/j.1749.6632.1997.tb48340.x.

[126] Boslough, M.; Schultz, P.; Harris, R. Hypervelocity airburst shower formation of the Pica Glass. In *13th Planetary Crater Consortium Meeting* 13, 2022; p. 2021.

[127] Van Ginneken, M.; Harvey, R.P.; Goderis, S.; Artemieva, N.; Boslough, M.; Maeda, R.; Gattacceca, J.; Folco, L.; Yamaguchi, A.; Sonzogni, C.; et al. The Identification of Airbursts in the Past: Insights from the BIT-58 Layer. *Earth Planet. Sci. Lett.* **2024**, *627*, 118562, 10.1016/j.epsl.2023.118562.